Study of cosmic rays by Auger and LHAASO : R&D and Data Analysis of AugerPrime and simulations for LHAASO

Zizhao Zong

université PARIS-SACLAY

UNIVERSITÉ PARIS SUD
Comprendre le monde, construire l'avenir

NNT : 2017SACLS366

THÈSE DE DOCTORAT
DE L'UNIVERSITÉ PARIS-SACLAY
PRÉPARÉE À L'UNIVERSITÉ PARIS-SUD

ÉCOLE DOCTORALE N°576
Particules, Hadrons, Énergie, Noyau, Instrumentation, Imagerie, Cosmos et Simulation (PHENIICS)
Spécialité de doctorat : Astroparticules et cosmologie

Par
M. Zizhao Zong

Study of cosmic rays by Auger and LHAASO: R&D and Data Analysis of AugerPrime and simulations for LHAASO

Thèse présentée et soutenue à Orsay , le 20/10/2017

Composition du Jury :

M. Reza Ansari	Professeur, LAL	Président du jury
M. François Montanet	Professeur, LPSC	Rapporteur
M. Zhen Cao	Professeur, IHEP, China	Rapporteur (absent)
M. Olivier Martineau-Huynh	Maître de conférences, LPNHE	Examinateur
Mme Giulia Hull	Ingénieur de recherche, IPNO	Examinatrice
Mme Tiina Suomijärvi	Professeur, IPNO	Directrice de thèse

Abstract

Cosmic rays are charged particles, as well as coproducts like photons and neutrinos, originated in cosmic-ray sources inside or outside the Galaxy. They arrive at the top of the Earth's atmosphere with primary energies of up to a few 10 EeV. When the cosmic rays enter the atmosphere, they interact with the molecules in the air and produce a large number of secondary particles, creating an extensive air shower (EAS). The ground-based observation of the EAS can be used to deduce the energy, the arrival direction, and the mass composition of cosmic rays.

The Pierre Auger Observatory and the Large High Altitude Air Shower Observatory (LHAASO) are both EAS observatories aiming at solving open questions of cosmic-ray studies but focusing on different energy ranges, the highest-energy and the so-called knee (around few PeV) regions. Based on the experience gained during the operation of the Pierre Auger Observatory for more than 10 years, the Auger collaboration has proposed an upgrade project, called "AugerPrime", with the aim of increasing the sensitivity of the surface detector array to the primary mass of cosmic rays.

Both observatories employ the so-called "hybrid detector arrays" composed of optical telescopes overlooking the longitudinal development and ground detector arrays sampling the signal densities in the lateral direction of the EAS. The ground detector arrays of both observatories are being constructed or upgraded to have various types of particle detectors (scintillator and water-Cherenkov detectors), which allow us to decompose the electromagnetic and muonic components of the EAS.

In this thesis, a series of studies contributing to the AugerPrime and LHAASO projects are presented. Concerning the AugerPrime project, the present study includes R&D work of the scintillator detector and data analysis of the engineering array. For the LHAASO project, simulations of the wide field of view Cherenkov telescope array and a multivariate analysis of LHAASO-hybrid observations for the primary mass identification are presented.

Résumé

Les rayons cosmiques sont des particules chargées, ainsi que des coproduits comme les photons et les neutrinos, issus de sources de rayons cosmiques galactiques ou extragalactiques. Ils arrivent au sommet de l'atmosphère terrestre avec des énergies primaires allant jusqu'à quelques 10 EeV. Lorsque les rayons cosmiques entrent dans l'atmosphère, ils interagissent avec les molécules de l'air et produisent un grand nombre de particules secondaires, créant une gerbe atmosphérique (extensive air shower, EAS). Accompagné des particules secondaires, une émission de la lumière Cherenkov et de la lumière fluorescence est induite par le passage des particules dans l'atmosphère.

L'Observatoire Pierre Auger et Large High Altitude Air Shower Observatory (LHAASO) sont des observatoires dédiés à la détection des gerbes atmosphériques dans le but de répondre aux questions ouvertes concernant les rayons cosmiques, mais se concentrant sur différentes gammes d'énergie, les plus hautes énergies et les énergies autour de quelques PeV. Après plus de 10 ans d'exploitation de l'Observatoire Pierre Auger, la collaboration Auger a proposé une amélioration des détecteurs de son réseau de surface, appelée «AugerPrime». Le but est d'augmenter la sensibilité à la masse des particules primaires en ajoutant un détecteur scintillateur sur le détecteur Cherenkov à eau. Les deux observatoires sont dits «hybrides» car composés de télescopes optiques observant le développement longitudinal des gerbes et des réseaux de détecteurs de surface échantillonnant leurs profils latéreaux.

Dans cette thèse, une série d'études contribuant aux projets AugerPrime et LHAASO sont présentées. En ce qui concerne le projet AugerPrime, la présente étude comprend le travail de recherche & dévelopment des scintillateurs et l'analyse de données du réseau de tester. Pour le projet LHAASO, des simulations de télescopes Cherenkov et une analyse multivariée des observations hybrides pour l'identification des masses primaires sont présentées.

Acknowlegement

First and foremost, I would like to express my sincere gratitude to my supervisor, Prof. Tiina Suomijärvi. I'm grateful for her supervision of the thesis work, her patience, her encouragement, her help in daily life, and her advice for my future plan. All these will be a valuable wealth for my whole life.

Then I would like to thank the other jury members, Mr Ansari, Mr Montanet, Mr Martineau-Huynh, Ms Hull, and Mr Cao for their insightful questions, comments, and corrections on the thesis.

I also would like to express my gratitude to Ms Giulia Hull and our colleagues in the RDD group of IPN for their supervision and collaboration on the SSD R&D work. Many thanks go to the colleagues in the astro-particle group of IPN for their advice and help on thesis work.

I'm grateful to my institute, Institut de Physique Nucléaire d'Orsay (IPNO) where I have spent three years and have learned a lot of knowledge related to my thesis subject. Many thanks go to all the colleagues in IPNO for their help in both work and daily life.

Many thanks go to the Auger and LHAASO collaborators for the illuminating discussions and the effective teamwork.

As a Ph.D. student in the CSC-UPSud program (No.201406170006), I'm grateful to my funding association: China scholarship council and Université Paris-Sud.

Many thanks go to my beloved family for their support and encouragement. Finally, Many thanks go to my friends in Orsay area for their concerns and help during the last three years.

Contents

1

Introduction

After the cosmic rays were discovered in 1912, a great number of studies have been performed to understand their nature and origin. For experimental studies, balloons, satellites and ground detectors have been used. The observed cosmic-ray spectrum extends from few GeV up to $\sim 10^{20}$eV. The chemical composition of the cosmic rays is mostly light elements (proton and Helium). By accurately measuring the mass composition, the energy spectrum, and the arrival direction of high-energy cosmic rays, including charged particles, gamma rays and neutrinos, we expect to have a better understanding of their origin.

The Pierre Auger observatory (Malargüe, Argentina), aiming to probe the origin of cosmic rays with the highest energies (>10^{18}eV), has steadily taken data since 2004 and yielded important results. In particular, a flux suppression is clearly observed at $\mathrm{E} > 4 \times 10^{19} eV$, and the cosmic-ray composition tends to be heavier at the highest energies. The Auger collaboration has proposed an upgrade project for the Observatory, named "AugerPrime", in order to precisely determine the mass composition of the ultra-high-energy cosmic rays (UHECR) based on shower-by-shower measurements. The engineering array (EA) of 12 upgraded detector stations has been deployed in October 2016 and is since then continuously taking data.

The large high altitude air shower observatory (LHAASO), which is now under construction at 4400 m a.s.l. in Daocheng, China, is a multipurpose astro-particle experiment. One of the

scientific goals of LHAASO is to measure the cosmic-ray spectrum around the "knee" region from 30 TeV to 100 PeV. LHAASO proposes to detect the extensive air showers induced by different primary particles with a hybrid technique by combining three detector arrays, wide field of view Cherenkov telescope array (WFCTA), water Cherenkov detector array (WCDA), and 1 km^2 array. This hybrid observation is expected to have good performance for identifying the primary mass.

Auger and LHAASO both aim at contributing to solve the open questions of cosmic rays focusing on different energy regions of the cosmic-ray spectrum. The motivation of this thesis work is to contribute to the research and development of the AugerPrime and LHAASO cosmic-ray experiments. This thesis work was conducted under the framework of these two experiments and mainly focuses on the R&D work for the AugerPrime scintillator detectors, on the analysis of the first data from AugerPrime EA, on the simulation of WFCTA and on the analysis of LHAASO-hybrid simulation data by using the multivariate analysis (MVA) method.

The thesis work is not only achieved by the author alone, but is a result of collaboration between IPN-Orsay and the collaborators from Auger and LHAASO. In order to objectively define the author's part in the presented work, the author's own contribution is indicated in the Chapters 4, 5, and 7. The manuscript of this thesis is organized as follows:

- In Chapter 2, the cosmic-ray studies are briefly introduced including the history of cosmic-ray studies, the physics principles of the cosmic rays, the extensive air showers (EAS), and the ground-based cosmic-ray experiments.

- In Chapter 3, the history and the status of the Pierre Auger observatory are introduced. The physics motivation and the technical implementations of the AugerPrime upgrade project are also presented.

- In Chapter 4, the R&D work for the AugerPrime scintillator surface detectors (SSD) is presented including the tests of the SSD configurations and the fabrication of the fiber/PMT optical coupling module. This R&D work was supervised by the colleagues of the IPN-RDD (R&D Détecteurs) group. The optical coupling module was fabricated with the machine tool by the staff of the IPN workshop. The author performed all the tests of SSD components (scintillator, fiber, and optical method), made the LCE (light-collection efficiency) estimate for different scintillator/fiber configurations, participated in the design and the assembly of the polished optical coupling module of SSD, and wrote the technical reports and publications.

- In Chapter 5, the analysis of the first data from the AugerPrime engineering array

consisting of 12 upgraded detector stations is presented. In particular, the detector calibration and the long-term performance of the EA stations are presented. Furthermore, the shower signals measured by both the water-Cherenkov detectors (WCD) and the scintillator surface detectors and the preliminary results of the signal accuracy are discussed. This work was done in collaboration with the AugerPrime team. The author developed the routine to read the first data of the AugerPrime engineering array, evaluated the performance of the EA stations, and studied the shower signals of these upgraded detectors. He also wrote the technical reports and publications.

- In Chapter 6, the scientific goals of LHAASO and the design of the WCDA, KM2A, and WFCTA detector arrays are introduced.

- In Chapter 7, the simulation of the LHAASO-WFCTA is first presented. The primary energy reconstruction of the EAS based on the WFCTA simulation is then introduced. In the last sections of this chapter, the results obtained on the primary particle identification with the LHAASO hybrid detector, which consists of WCDA, KM2A, and WFCTA by using the multivariate method, are presented. The characteristics of various MVA algorithms and the comparison of their performances when they are used for the primary mass identification are discussed. In this work, the WFCTA simulation code was developed by the LHAASO-WFCTA team. As a member of this team, the author optimized the I/O module and the structure of the code, developed the camera simulation module, and participated in the debugging of the code. Concerning the particle identification with the MVA methods, the simulation of air showers and LHAASO detectors was implemented by the collaborators in IHEP. The author did the preparation (fitting and tuning) of simulation data, developed the MVA scripts for the primary mass classification and analyzed the results from the MVA classifiers.

- In Chapter 8, all the results of this thesis are summarized and the prospects for further work are discussed.

Currently, the AugerPrime and LHAASO projects are both under construction. The studies presented in this thesis have been presented and discussed in the collaboration meetings and conferences and have contributed to both projects.

2

Cosmic-ray studies

2.1 A brief history of cosmic-ray studies

Cosmic rays are high-energy radiations and originating particles from the outer space. They have been accelerated and traveling for hundreds of millions of years in the universe since the whole cosmos came into being. Cosmic rays carry information about the origin and acceleration, propagation and interaction with astrophysical environments. Therefore, they are important messengers for astrophysics, cosmology and particle physics. The study of cosmic-ray related physics has played an important role in humans' exploration of the nature since scientists started to understand cosmic rays about a hundred years ago.

The initial discovery of cosmic rays was led by the study of gas conductivity in 1900 [1–3]. In the experiments, the gas was observed to have some residual conductivity after the removal of all radioactive sources, and therefore can not be understood as the effect of natural radioactive isotopes in the earth's crust. In 1912, with a hot air balloon risen to ~5300 meters a.s.l., V. F. Hess found that the ionization rate of the air at high altitude was several times of that at the ground level [4]. From 1913 to 1914, W. Kolhörster repeated Hess' experiment and reached the altitude of ~9300 m [5, 6]. These results indicated that the ionization was induced by the "radiation" from the outer space.

In 1926, R. A. Millikan first introduced the term "cosmic rays", which is generally used today [7]. In 1928, J. Clay et al. found that the ionization rate increased with the latitude, which indicates that the ionization source was charged particles and deflected by the geomagnetic field. In 1929, by using a cloud chamber, D. V. Skobelzyn first observed the trajectory of cosmic- ray particles. In 1932, with the cloud-chamber method, C. C. Anderson found the existence of the Positron [8], which was predicted in Dirac's theory of relativistic quantum mechanics. In 1937, Anderson and S. Neddermeyer discovered the Muon (μ), which doesn't undergo the strong interaction [9]. In 1946, Rochester and Butler found the V-shape tracks in the cloud chamber, which was interpreted as the K meson (Kaon) [10]. This was the first strange particle discovered. In 1947, with nuclear emulsion exposed at a high altitude, Lattes Occhialini and Powell found the π meson [11] that was predicted by H. Yukawa in 1935 [12–14]. In 1951, the first strange baryon (Λ) was discovered in cosmic ray experiments by Armenteros' group [15, 16]. Before the advent of particle accelerators in the 1950s, cosmic-ray experiments were the most general ways to study particle physics for scientists at that time.

The famous "Geiger–Müller counter" was invented in 1928 [17] and improved by W. Bothe in 1929 [18]. This device allowed scientists to perform a precise-time measurement

of the radiation. The coincident measurement could separate cosmic-ray events from the radioactive background. This technique is now generally used for nuclear and particle physics.

In 1938, P. Auger and his colleagues discovered the "extensive air shower" (EAS) induced by cosmic rays by using the coincidence between multiple groups of Geiger-Müller counting tubes deployed in the Alps [19]. In their experiment, they measured the relationship between the coincident counting rate of the tubes and the distance between them, and found that, contrary to their expectations, the coincident counting rate dropped rapidly with the increase of the distance, and then basically remained unchanged to the distance of ~300 m. Their experiments were regarded as a milestone for the study of EAS and initiated the study of high-energy cosmic rays with ground detector arrays. In 1963, J. Linsley et al. observed the first highly energy cosmic-ray event of $\sim 10^{20}$ eV with a ground detector array [20]. In 1966, the cosmic microwave background (CMB) was discovered [21]. Greisen [22], Zatsepin and Kuzmin [23] noted that high-energy cosmic rays would lose energy when interacting with cosmic background photons, which results to the so-called Greisen-Zatsepin-Kuzmin (GZK) cutoff ($\sim 5\times 10^{19}$ eV) in the cosmic-ray energy spectrum. In 1991 and 1994, the Fly's-eye experiment [24] and the AGASA experiment [25, 26] measured the highest energy cosmic-ray events at 10^{20} eV. Several experiments were proposed to solve the issue between experimental results and the theoretical prediction and answer the open questions of cosmic-ray studies. The results of the HiRes experiment, which was developed based on the Fly-eye experiment, appeared to be in agreement with the prediction of GZK cutoff [27]. The recent results from the Pierre Auger observatory [28, 29] also show a flux suppression above 4×10^{19} eV [30]. However, the origin of the suppression still remains unknown.

The history of cosmic-ray studies was fruitful in the last one hundred years. However, some open questions remain for further studies, such as the origin of cosmic rays and the mechanism of cosmic-ray acceleration and propagation. Along with the development of technology, a number of advanced scientific projects have been proposed all around the world. One can expect important results in this field.

2.2 Characteristics of cosmic rays

2.2.1 The spectrum of cosmic rays

The energy spectrum is an important aspect of cosmic-ray studies, which intuitively reflects the relationship between the flux and the energy of cosmic rays. Cosmic-ray acceleration and propagation leave their imprint in the cosmic-ray spectrum making it one of the most important observable. The energies of cosmic rays arriving at the top of the atmosphere are

distributed in a large range of 11 orders from 10^9 to 10^{20} eV (see in Figure 2.1).

For cosmic rays with energies of 10^9 to 10^{20} eV, the energy spectrum can be expressed roughly in the power-law form:

$$\frac{dN}{dE} \propto E^{-\gamma} \tag{2.1}$$

where dN/dE is the differential flux, E is energy, $-\gamma$ is the index of the energy spectrum. With the improved accuracy of cosmic-ray measurements, it is found that the cosmic-ray spectrum is not a simple power-law spectrum. At the energy of $\sim 3.2 \times 10^{15}$ eV, the index of the spectrum changes from -2.7 to -3.1, this structure is called the "knee" region. At the energy of $\sim 4.0 \times 10^{17}$ eV, the index changes again from -3.1 to -3.3, this region is named as the "second knee". At the energy of $\sim 4.0 \times 10^{18}$ eV, the index changes back from -3.3 to -2.7, this region is called the "ankle". The flux suppression can be clearly seen at the energy of $\sim 4\times 10^{19}$ eV in the spectrum.

For the knee in the spectrum, there are some potential origins but no conclusive explanation at present. It may be attributed to the energy limits of the cosmic-ray acceleration in the Galaxy. The second knee may be caused by the escape of heavy particles. As for the ankle region, it is believed to be induced by the superposition of Galactic and extra-galactic cosmic rays. The GZK cutoff, as mentioned in the previous section, is due to the interaction between the cosmic rays and the CMB, which is the heat radiation of 3 K left in the Big Bang period.

2.2.2 The origin of cosmic rays

The exact origin of cosmic rays is still inconclusive for now, although there are some reasonable explanations such as the intense activities of the stellar surfaces, supernova explosions, pulsars, active galaxies and etc..

According to the different origins, cosmic rays can be divided into solar, galactic and extra-galactic cosmic rays. It is observed that, during solar flares, the shock generated by the solar wind can accelerate the particles in the interplanetary space to energies of keV to MeV level. Compared to galactic and extra-galactic cosmic rays, the energies of solar cosmic rays are rather low and the flux of them is synchronized with the activities of the sun. Galactic cosmic rays with energies of up to 10^{15} eV are considered to be originated from the supernova explosions and other phenomena that are the most intense high-energy physics processes in the Galaxy.

The origin of cosmic rays with energies larger than 10^{15} eV is considered to be in the extra-galactic space. Possible candidates can be radio galaxies, burst galaxies, and quasars. As for cosmic rays with energies larger than 10^{18} eV, there is no clear explanation for their origins at present.

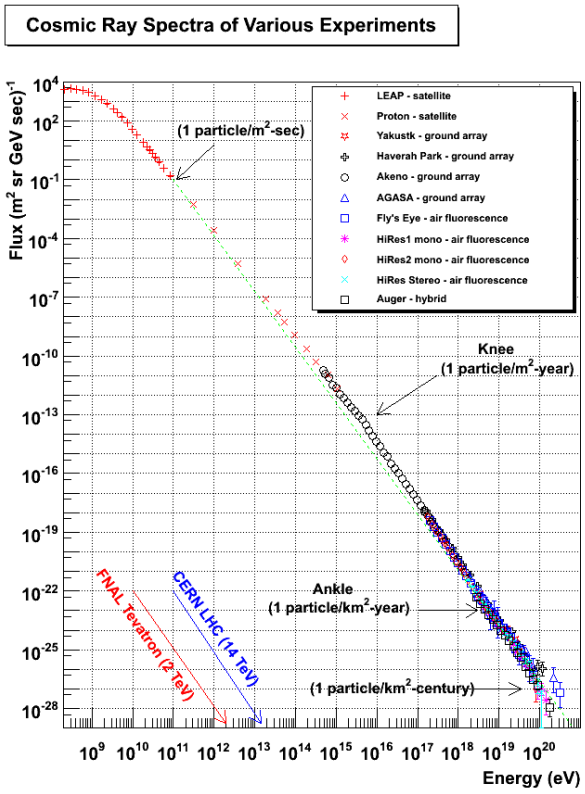

(a)

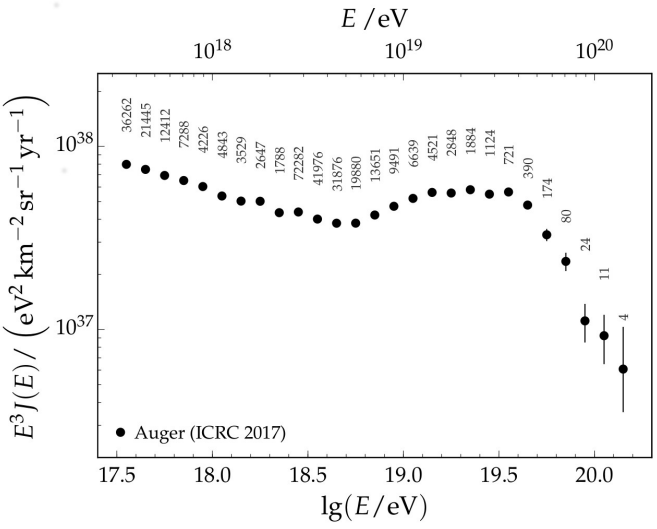

(b)

Figure 2.1 – 2.1(a) shows the cosmic-ray spectrum measured by various experiments. This figure is taken from ref.[31]. 2.1(b) shows the cosmic-ray spectrum in the energy range of E>10^{17} eV measured by the Pierre Auger observatory. This figure is taken from ref.[32].

2.2.3 The mass composition of cosmic rays

Cosmic rays can be classified as primary or secondary cosmic rays. Primary cosmic rays are generally the particles created by external sources which are generally outside of the solar system. These primary cosmic rays interact with the matter in the interstellar medium during its propagation and produce secondary particles, which are so-called secondary cosmic rays. It is estimated that about 98% of the cosmic rays at the top of the atmosphere are nuclei and 2% are electrons. For the nuclei part, it is composed of about 87% protons, 12% heliums, and 1% for heavier nuclei. These heavier nuclei can be divided into the following groups according to their Z values: light nuclei ($3 < Z < 5$), medium nuclei ($6 < Z < 9$), heavy nuclei ($10 < Z < 19$) very heavy nuclei ($20 < Z < 30$), ultra heavy nuclei ($Z > 30$).

The relative proportion of each element in the universe is called the cosmic element abundance, which is the basis for studying the origin of elements and explaining the evolution of various astronomical objects. The element abundance in many astronomical objects is supposed to be similar to that in the solar system. Therefore, the element abundance in the solar system is generally used as the cosmic element abundance. Figure 2.2 shows the element abundance of cosmic rays and of the universe, respectively.

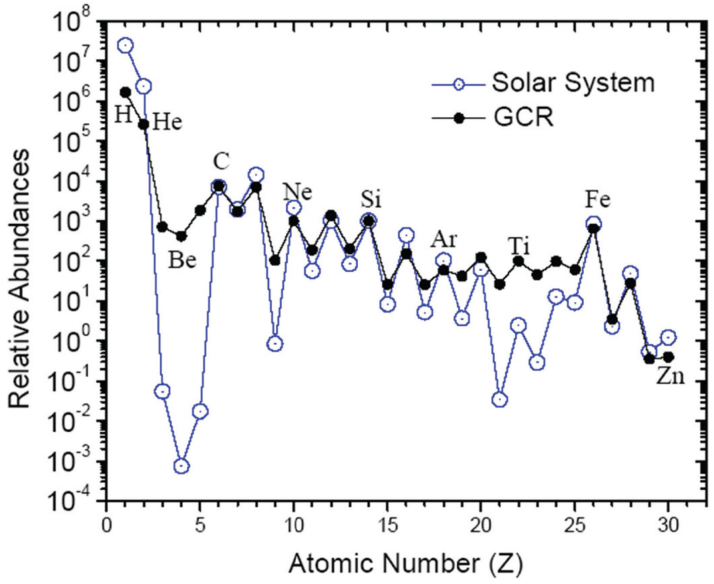

Figure 2.2 – Comparison of relative abundances between Galactic (closed dots) and Solar System (open dots) cosmic rays, which is taken from [31]

It can be seen from the graph that the relative element abundances of Solar System and Galactic cosmic rays have similar distributions. In case of nuclei with $Z \geq 6$, the abundance of even nuclei is always about one order higher than the abundance of odd nuclei. The abundance of H and He in cosmic rays is lower than their abundance of the universe, since their Larmor

radii are larger than the heavy nuclei thus they escape the Galaxy easier. Li, Be, and B are considered to be generated by the collisions between C, N, O and the interstellar medium. Sc, Ti, V, Cr, Mn are considered to be secondary products of Fe. The analysis of cosmic-ray mass composition can contribute to the study of the origin and propagation of cosmic rays.

2.3 Extensive air showers

The extensive air shower (EAS) is a cascade of ionized particles and electromagnetic radiation produced in the atmosphere when a primary cosmic ray enters the atmosphere. All high-energy cosmic rays from outer space will inevitably collide with the various nuclei in the air, then undergo a series of interactions such as nuclear cascade, electromagnetic cascade, and weak interaction, and produce secondary particles. When the energies of the secondary particles are high enough, they will continue to collide with the substance in the air and generate new secondary particles. Therefore, many generations of secondary particles are produced in this process and these particles will travel down towards the ground at a speed close to the light speed. These particles will be traveling in a quasi-conical surface and spread in the area of several square kilometers.

2.3.1 Development of the EAS

Secondary particles, according to the composition, can be divided into three categories: hadron components, electromagnetic components, and μ components. Figure 2.3 shows the development of an air shower. The depth of the first interaction between each cosmic-ray particle and the atmosphere, X_0, depends on the nature and the primary energy of this particle. The X_0 is generally around 40 g/cm^2 corresponding to an altitude of from 15,000 to 35,000 m. The first batch of secondary particles are usually nuclei, π mesons and K mesons.

The secondary nuclei continue to interact with the atmospheric molecules and lose about half of their energy each time in the reaction. Baryons, π mesons and K mesons with long lifetime form the core of the hadron shower. The hadron shower can produce μ components and electromagnetic components. The generated π^0 in the showers will decay into a pair of γ photons, and these γ photons will produce further electromagnetic cascades. Electromagnetic showers also produce a small part of the hadron component and μ components. 90% of μ components are generated by the decay of π mesons, and K mesons, and only about 10% are produced in the electromagnetic composition [34]. As muons are only affected by the ionization when propagating in the atmosphere, they basically arrive at the ground with a very low degradation of energy. Due to the decay of π mesons and muons, a neutrino component

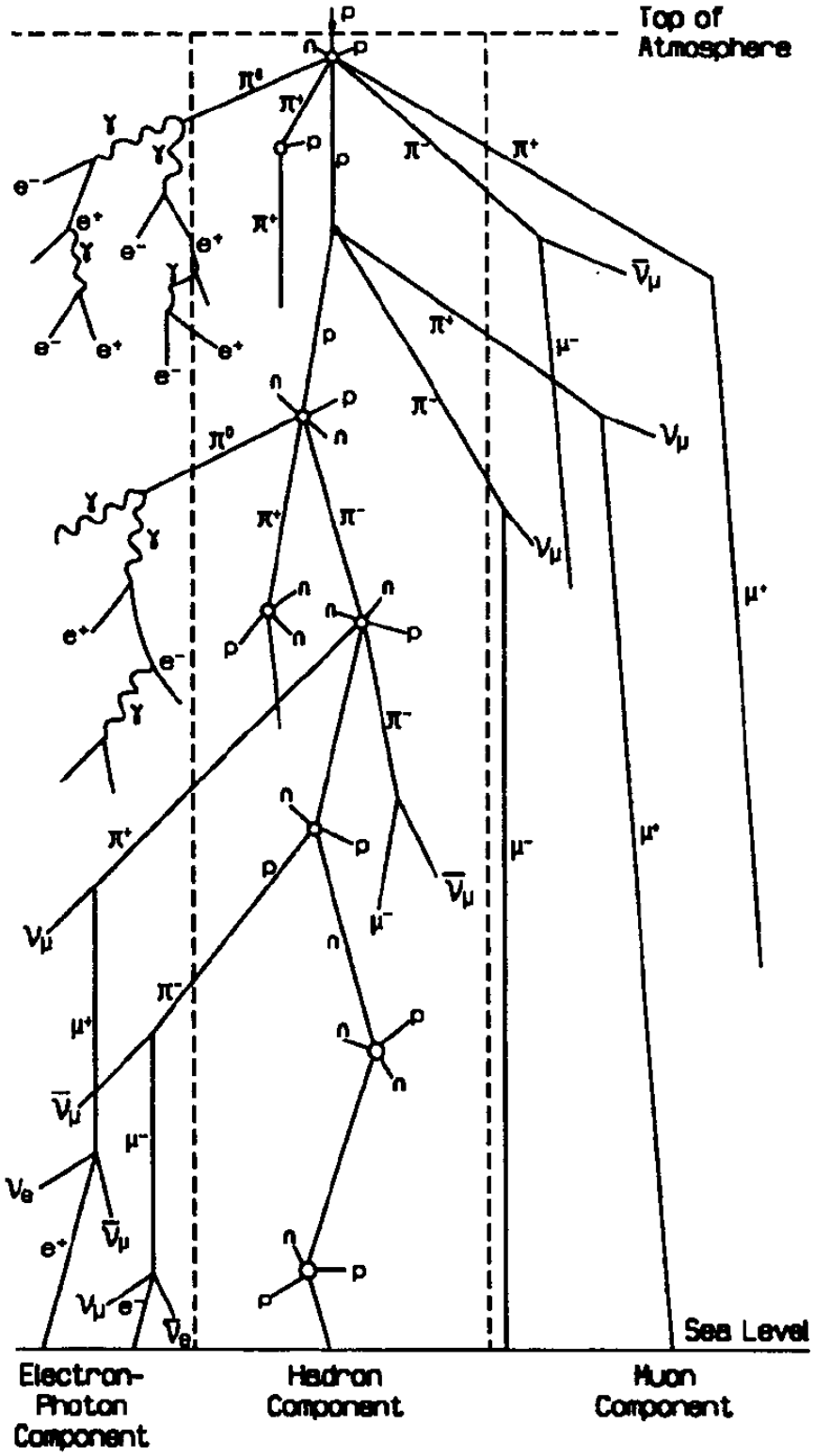

Figure 2.3 – The development of an air shower induced by a high-energy proton. It is composed of hadronic, electromagnetic and muon cascades. This figure is taken from [33].

is also generated in the air shower. The secondary particles usually travel downwards with a certain angle in air showers. These secondary particles will produce many generations of secondary particles. The lateral expansion and the density of the particles get larger with the increase of the atmospheric depth in the shower development. The number of secondary particles will reach the maximum value at the atmospheric depth of X_{max} when the average energy of these particles equals a critical value. This is a result of the competition between different physics processes. For the hadronic showers, the interaction length will compete with the decay length. For the electromagnetic showers, the radiation processes including bremsstrahlung and pair production will compete with the processes of ionization losses, the photoelectric effect, and the Compton scattering. After reaching the X_{max}, the secondary particles gradually decay or are absorbed by the atmosphere, the number of secondary particles get decreased along with the shower development.

2.3.2 Electromagnetic cascade

In the air shower development, high energy γ photons (above a few MeV, below which the photoelectric effect and the Compton scattering are dominant) can interact with matter in the air primarily via pair production to produce positrons, and electrons. These electrons will then produce γ photons via bremsstrahlung. The secondary photons, positrons and electrons continue to repeat this process, thereby resulting in an electromagnetic (EM) shower.

The EM shower will get laterally spread in the atmosphere mainly due to the multiple Coulomb and Compton scatterings. Pair production, bremsstrahlung, excitation, and ionization also cause the additional scattering and energy loss. The electromagnetic cascade can be described with the Heitler model [35]. When a particle with an initial energy of E_0 has moved for a certain depth of atmosphere λ_{em}, two secondary particles with the same energy are generated and the secondary particles continue to repeat the process. In this process, the difference of interaction cross-section with respect to the energy is ignored. The number of particles N increases with the atmospheric depth X. After the n collisions, the number of particles at the depth of $X = n \cdot \lambda_{em}$ and the energy of each particle can be expressed as:

$$N = 2^n = 2^{\frac{X}{\lambda_{em}}}\ ,\ E = \frac{E_0}{2^{X/\lambda_{em}}} \tag{2.2}$$

At the shower maximum, the number of particles N_{max} and the depth X_{max} can be described as:

$$N_{max} = \frac{E_0}{E_c}\ ,\ X_{max} = \lambda_{em} \cdot log_2\left(\frac{E_0}{E_c}\right) \tag{2.3}$$

where the E_c is the critical value of the particle energy [35]. E_c can be understood as the average energy where the collisional losses begin to exceed the radiative losses in the shower

development [36]. The Nishimura-Kamata-Greisen (NKG) equation [37, 38] was proposed to precisely describe the lateral distribution of the electromagnetic cascade:

$$\rho(r,N) = \frac{N}{r_M^2}\frac{\Gamma(4.5-s)}{2\pi\Gamma(s)\Gamma(4.5-2s)}\left(\frac{r}{r_M}\right)^{s-2}\left(1+\frac{r}{r_M}\right)^{s-4.5} \tag{2.4}$$

where $\rho\ (r,N)$ is the particle density at the distance r from the shower axis, N is the total number of the shower secondaries, and r_M is the Molière radius (~80m at sea level) [39, 40]. s is the shower age [41, 42], which can be expressed as:

$$s = \frac{3X/X_0}{X/X_0 + 2X_{max}/X_0} \tag{2.5}$$

where X_{max} is the atmospheric depth of the shower maximum, X_0 is the depth of the first interaction.

2.3.3 Hadronic cascade

The hadronic cascade is produced by the interaction between high-energy hadrons (e.g. protons) in the shower and molecules in the atmosphere via the strong interaction. In this process, a large number of π mesons are produced together with some α and very few heavy nuclei. The longitudinal development of hadronic showers can be described with the Gaisser-Hillas function [43]:

$$N(X) = N_{max}\left(\frac{X-X_0}{X_{max}-X_0}\right)^{\frac{X_{max}-X_0}{\lambda}} exp\left(\frac{X_{max}-X}{\lambda}\right) \tag{2.6}$$

where N(X) is the number of the particles at the depth of X, N_{max} is the total number of particles at the shower maximum, and λ is about 70 g/cm^{-2}.

The relationship of the X_{max} values of showers with a certain energy and initiated by different primary particles can be described as [44–46]:

$$X_{max}^A = X_{max}^P - X_0 \cdot lnA \tag{2.7}$$

where X_{max}^P is the maximum of the proton-induced shower. For the hadronic showers with a fixed primary energy, heavy nuclei can produce more muons than light nuclei. The relationship between the muon numbers produced by a nucleus N_μ^A and by a proton N_μ^p can be described as [36]:

$$N_\mu^A = N_\mu^P A^{1-\beta} \tag{2.8}$$

X_{max} and N_μ are usually two keys to identify the primary particle of air showers.

In the air showers, besides the components mentioned above, there are also radio waves, Cherenkov radiation, fluorescence light, etc. emitted with the shower development.

2.3.4 Cherenkov radiation

According to the special theory of relativity, the velocity of a object with static mass can not exceed the speed of light in the vacuum c. The refractivity of a certain medium n is larger than that of vacuum $n_{vacuum} = 1$, and the velocity of light in this medium v can be expressed as $v = \frac{c}{n}$. Therefore, when the light propagates in a medium like water or air, v is less than c. When a charged particle is accelerated to be faster than v in a transparent medium, the Cherenkov radiation is emitted.

The primary particle of an air shower from the outer space can produce many secondary particles when it enters the atmosphere. During the shower development, the so-called "atmospheric Cherenkov light" of all those secondary particles faster than the local speed of light in the air is emitted. The opening angle θ of the Cherenkov radiation can be described as:

$$cos\theta = \frac{1}{n\beta} \tag{2.9}$$

where β is the ratio of $\frac{v}{c}$. θ depends on the kinetic energy of the charged particle and the refractivity of the medium (see Figure 2.4). Since θ angle is rather small and usually less than 1.4°, the wavefront of atmospheric Cherenkov light propagates only inside a narrow cone around the direction of the incident particle [47].

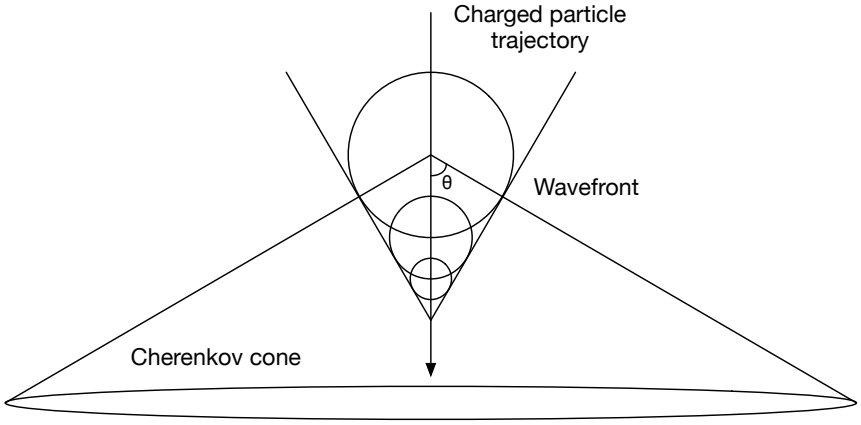

Figure 2.4 – The emission of the atmospheric Cherenkov light [48].

The propagation of Cherenkov light produced in the shower development has a good directivity due to the small opening angle. Benefiting from this advantage, the detection of Cherenkov component turns to be important for the reconstruction of the shower event. The imaging or non-imaging Cherenkov detector arrays are widely used in modern cosmic-ray or gamma-astronomy experiments (see chapter 7).

2.3.5 Fluorescence light

The fluorescence light was first discovered in 1939 and then this related technique was applied in the production of fluorescent lamps [49]. During the development of an air shower, the molecules in the air, mostly nitrogens, can be ionized and excited by secondary particles. These molecules then emit visible or UV (ultraviolet) light during the process of their de-excitation.

In the astro-particle experiments, air fluorescence telescopes are generally deployed at a distance of several km away aside the ground array observing the fluorescence light emitted symmetrically and isotropically in the air [50].

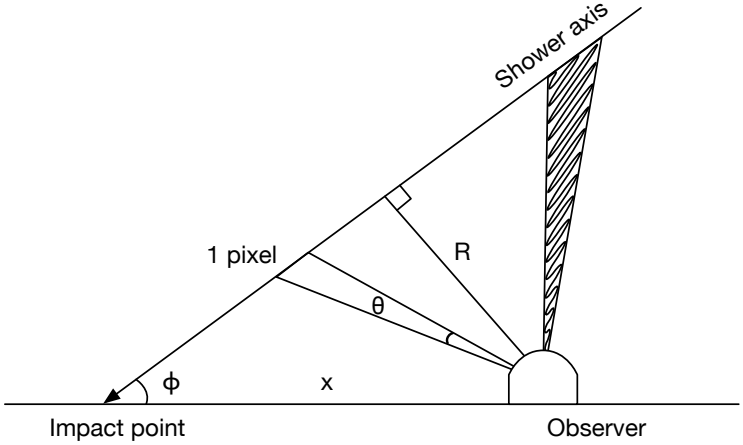

Figure 2.5 – The detection of air fluorescence light [48].

Figure 2.5 shows the detection of air fluorescence light in the shower observation. The duration of signals induced by fluorescence light can be expressed as:

$$\Delta t_{PMT} = \frac{2R}{c \cdot cot(\theta/2)}, \; R = x \cdot sin\phi \tag{2.10}$$

where θ is the FoV of the detector unit, R is the distance from the detector to the shower axis, x is the core distance on the ground, and ϕ is the angle between the shower axis and the horizontal axis.

By combining several cameras equipped with PMT arrays, the fluorescence detectors allow reconstructing the longitudinal development in the atmosphere of the shower event occurring tens of kilometers away [51]. The Pierre Auger observatory (see in chapter 3) and the Telescope Array are two main experiments employing fluorescence detectors working with ground arrays for the air shower measurements.

2.3.6 Radio emission

When the secondary charged particles, mostly for electrons and positrons, produced in the shower development moving in the air, the radio signal is emitted mainly due to the geomagnetic and Askaryan effects [52].

- The geomagnetic effect is the most important mechanism of radio emission during the shower development. Electrons and positrons produced in the shower can be deflected in opposite directions by the Lorentz force of the geomagnetic field (see Figure 2.6-left). Then the radio signal is emitted linearly polarized orthogonally to the direction of the geomagnetic field. The amplitude of radio emission due to this effect is correlated to the strength of the geomagnetic field and the angle between the geomagnetic field and the shower axis.

- The Askaryan effect is induced by a time-variation of the net charge-excess at the shower front. During the shower development, a net charge excess can be formed at the shower front and the charge is conserved due to a positively charged plasma created behind the shower front and along the shower axis (see Figure 2.6-right). A shower can be regarded as a point charge moving in the air. The Askaryan effect makes its charge change during the shower development, thus the radio signal is emitted. The Askaryan radio emission is radially polarized.

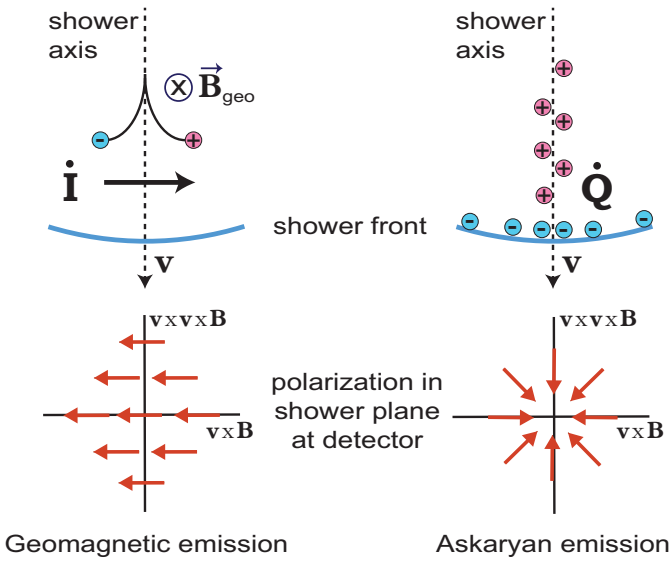

Figure 2.6 – Main mechanisms of radio emission in the shower development [52].

The emitted radio waves at wavelengths of a few meters are generated instantaneously with a high intensity due to the coherence and the superposition [53]. The attenuation of these

radio waves in the atmosphere before reaching the ground level is negligible and therefore the radio signal can be used to reconstruct the EM components of the shower. The power of radio signal pulses from the EAS is mainly distributed in the frequency range of 1 to 200 MHz. The typical radio signals have a duration of few 10 ns. This EAS observation technique has been successfully tested in the Auger Engineering Radio Area (AERA) [54].

2.4 Ground-based cosmic-ray experiments

2.4.1 Overview of ground-based EAS detection

In a broad sense of the word, cosmic-ray experiments refer to the all the scientific installation built to detect high-energy particles coming from the outer space. These experiments can be categorized as direct or indirect detection experiments.

The direct detection of cosmic rays is generally implemented by mounting the detectors onto a satellite or a balloon, which can operate in the Earth's orbit or at the top of the atmosphere. Good results of the cosmic-ray spectra up to few TeV have been produced from the satellite experiments such as Fermi-LAT [55], PAMELA [56] and AMS-02 [57]. The new generation satellite detectors (NUCLEON [58], CALET [59], DAMPE [60] and etc.) are designed to extend the energy range of this measurement up to ~1 PeV. For the measurement of higher energy range, the direct detection is limited by the load of satellites or balloons and can not be easily implemented with current technology.

Compared with the direct detection of the cosmic rays, the ground-based detectors have several advantages: large effective area, wide field of view, long duty cycle and easy maintenance. These features allow the ground-based detectors to measure cosmic rays with primary energies larger than 1 PeV.

Most of the ground-based cosmic-ray experiments are equipped with one or more detector arrays. One detector array is generally composed of one single type detector. In order to collect the most complete information of an air shower event, some experiments tend to employ a hybrid detection of air showers with a mixture of particle/optical detector arrays. The particle detectors have special sensitivities to the hadronic or electromagnetic components of the EAS. The optical detectors are in the form of telescopes or PMT arrays and can catch the Cherenkov or fluorescence light emitted in the shower development. The shower event then can be reconstructed by combining the parameters measured from various detector arrays.

The uncertainty of results measured by ground-based detectors is mainly due to three factors:

- **Atmosphere condition:** The atmospheric environment is complex and changing all

the time. This leads to additional fluctuations for the showers initiated by the primary particles with the same physics and geometry parameters.

- **Strong interaction models:** A large number of momentum transfer processes exist in the interaction between high-energy cosmic rays and atmospheric nuclei. Currently, these processes can not be calculated by the QCD (quantum chromodynamics) theory. The highest energy of a particle accelerated by the man-made accelerator is around a few TeV, which is much lower than the concerned energy range of cosmic rays. Simply extending the theoretical model to higher energy range leads to a series of problems. Although there are many sophisticated models [61–63] available for high-energy strong interactions, they are not completely consistent with the experimental results [64]. The reconstruction of physical parameters of the primary particles highly depends on the Monte Carlo simulation. For the same shower reconstructed with different strong interaction models, there is a slight difference between the results, which also leads to the additional uncertainty.

- **Energy calibration:** Different from the detectors used in satellite or balloon experiments, which can be calibrated with accelerators, ground-based detector arrays are difficult to be directly calibrated. This leads to the slight disagreement between the results from various experiments.

2.4.2 Detectors used in ground-based EAS experiments

In the last several decades, a series of ground-based EAS experiments have been built all over the world. The results from these experiments led to great progresses of the cosmic-ray studies. At the same time, the detection technique applied in these experiments also provide a valuable reference for the future cosmic-ray detectors. Figure 2.7 shows various detectors employed in ground-based cosmic-ray experiments. From the technical point of view, these detectors can be classified as particle detectors, optical detectors, or radio detectors.

Particle detectors

The particle detectors are deployed on the ground or underground. The detectors are located in a regular shape with a fixed spacing between each other in a large area. Then, the density of electrons, positrons, and muons of the shower front can be sampled at the location of each detector. These detectors are made of scintillator or water as the working material. The particles passing through the detector will interact with and deposit part or all of their energies in the working material of the detector. During this process, the visible light will be emitted.

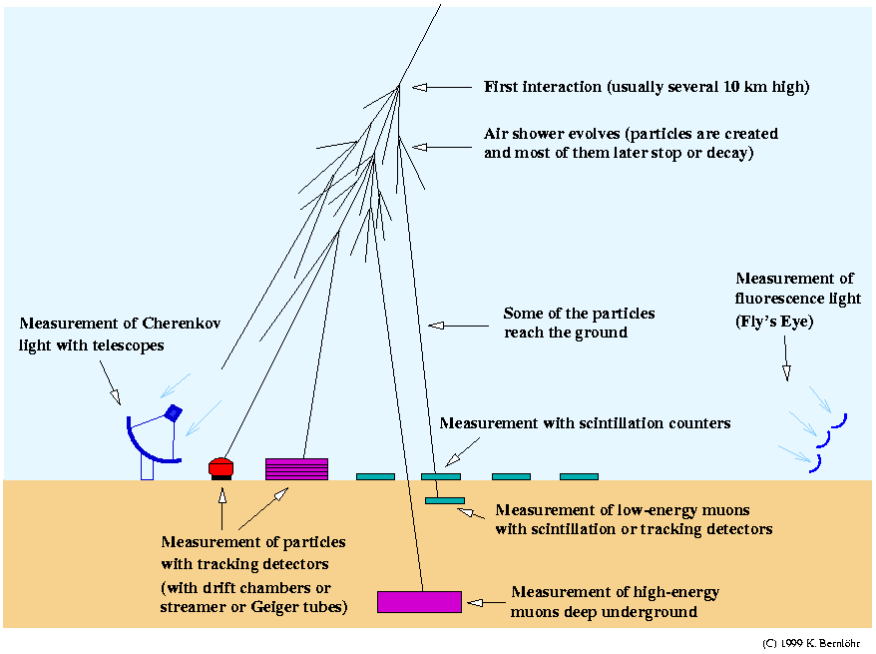

Figure 2.7 – Detectors used in EAS experiments [65].

The photodetectors equipped in the detector are used to collect these optical signals. The signal of a single detector can be triggered with a low-energy threshold and a fast response. The trigger of a shower event can be implemented by the coincidence of multiple detectors in the ground array. The arrival direction can be reconstructed by using the time information recorded by the detector. The energy of the primary particle is related to the total number of secondary particles measured by the whole array.

This kind of detector array is relatively simple to be built in a large scale. These detector arrays can measure the lateral profile of the shower. They also have a high precision for the reconstruction of shower geometry. For the energy reconstruction or particle identification, these detectors are usually working together with other detector arrays or specially designed to be sensitive to the muon components of the showers. The experiments using particle detector arrays include EAS-TOP [66], KASCADE[67] (upgraded as KASCADE-Grande [68]), the surface detector of the Pierre Auger observatory [69] and etc.

Optical detectors

As introduced in subsection 2.3.5 and subsection 2.3.4, fluorescence and Cherenkov light in visible and UV band is emitted during the development of the shower in the atmosphere. The optical detectors, mainly include fluorescence telescopes, atmospheric Cherenkov telescopes, and ground Cherenkov detectors, are used in EAS experiments to measure these light signals.

The first experiment using fluorescence observations was the Fly's Eye experiment [70]

(and the subsequent HiRes experiment [27]). This technique is also used in the Pierre Auger observatory [71] and the Telescope Array experiment [72].

Imaging atmospheric Cherenkov telescopes (IACT) with reflective mirrors of large area and cameras composed of photomultipliers was first used in the Whipple observatory in 1989. After that, scientists started to observe astronomical sources like the Crab Nebula with IACTs, opening a new era for ground-based gamma astronomy. Since then, the technique of IACTs has been widely used in many experiments, such as HESS, MAGIC and the future CTA (see in chapter 7).

The ground Cherenkov detectors are composed of a large-size photomultiplier tube (PMT) with a Winston-cone light collector installed on its entrance window. In the experiments of TUNKA-133 [73] and CASA-BLANCA [74], this type of detectors are deployed in an array with spacing of ~100 m to measure the lateral distribution of the Cherenkov light generated in the air shower.

Optical detectors have many advantages in the EAS detection, but they are limited by the environment of background light and the transparency of the atmosphere. Therefore, they can only operate in dark nights without clouds and moonlight. The average duty cycle of optical detectors is around 12%.

Radio detector

The radio detector used in the cosmic-ray experiments, such as AERA and Tunka-Rex (Tunka Radio Extension) [54], is mostly an array of antennas working together with other ground arrays. Radio antennas have the advantage of low cost, which is conducive to the construction of large area detector arrays. Furthermore, the antennas have stable performance and a full duty cycle.

3

Pierre Auger Observatory & AugerPrime

3.1 The Pierre Auger Observatory

3.1.1 Introduction to the Observatory

The Pierre Auger Observatory is a cosmic-ray observatory, aiming to probe the origin and characteristics of the cosmic rays with a primary energy above 10^{18} eV [69]. The Observatory is located in western Argentina, near the city of Malagüe, Province of Mendoza, at an altitude of 1400 m a.s.l.[75] (see in Figure 3.1). The observatory was officially completed in 2008, and it has been taking good-quality data since 2005. The Pierre Auger Collaboration consists of more than 500 physicists from nearly 100 institutions. A series of significant results have been reported by the collaboration concerning the flux and the mass composition of the ultra-high-energy (UHE) cosmic rays [76–81]. As the observatory provides a good performance in the angular reconstruction [82], it has also yielded a series of remarkable results on the arrival direction of cosmic rays. Some level of correlation has been observed between the highest energy cosmic rays and a catalogue of nearby sources [83, 84]. Furthermore, at large angular scales, evidence for dipole asymmetry in the arrival direction has been observed at energies above 8×10^{18}eV [85]. Based on the data collected by the observatory, related studies of UHE photons [86–89], UHE neutrinos [90–92], UHE neutrons [93, 94] and proton-air/proton-proton cross-section [95, 96] have been published in the last few years.

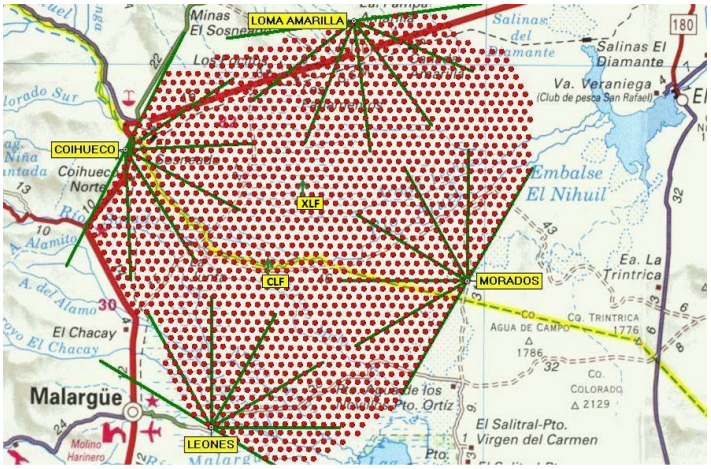

Figure 3.1 – The layout of the Pierre Auger Observatory. This figure is taken from ref.[69]

The Pierre Auger Observatory consists of 1660 water-Cherenkov detector (WCD) stations, generally known as Surface Detector (SD) array, spread over an area of $\sim$ 3000 km^2 in the Pampas. The SD array is overlooked by the fluorescence detector (FD) consisting of 27

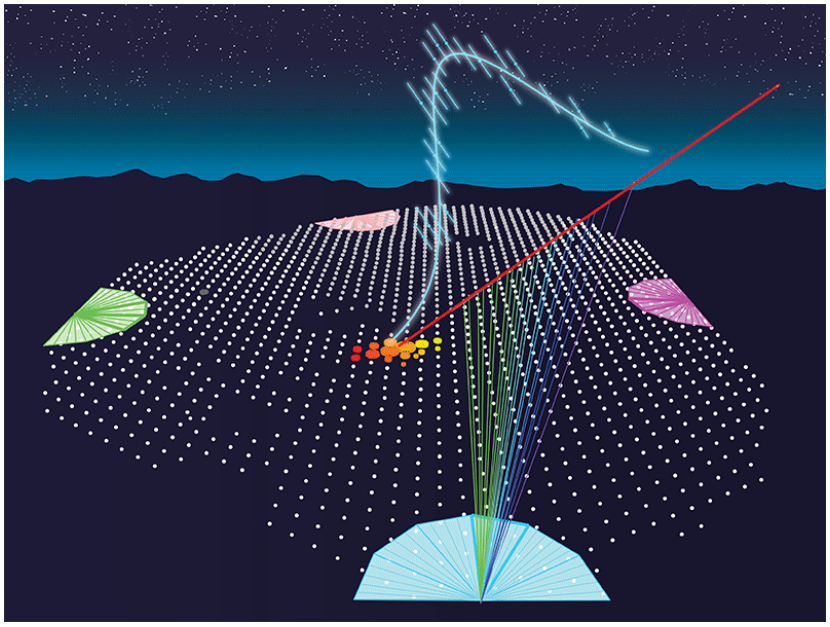

Figure 3.2 – The detection of a hybrid event from a cosmic-ray shower in the Pierre Auger Observatory. The SD array on the ground (white dots) and four FD sites detect the EAS in lateral and longitudinal direction, respectively. The red line shows the shower axis. This figure is taken from ref.[97]

fluorescence telescopes, installed in four FD sites: Los Leones, Los Morados, Loma Amarilla, and Coihueco (see in Figure 3.2). When a shower is generated in the atmosphere above the observatory, the SD array can view a slice of the EAS in the lateral direction by detecting muonic and electromagnetic components of the shower at the ground level, and the FD can provide the shower development in the longitudinal direction by observing the fluorescence light produced by the shower in the atmosphere. The design of this hybrid observation aims at measuring primary cosmic rays with two independent measurements, which can be complementary to each other. The SD array has good performance for determining the arrival directions and for estimating primary energies of the cosmic rays. The primary energy is inferred from the signal density measured by the SD array with the help of the FD calibration. The accurate primary energy can be determined with the FD since the fluorescence light production is proportional to the deposited energy of the EAS in the atmosphere. Beside the cross-check of primary energy with the SD array, the FD has another significant specialty. It is capable to observe the depth of the shower maximum size, X_{max}, which is crucial for the identification of primary mass composition. With this hybrid detector system, different components of the shower can be measured simultaneously. A comprehensive reconstruction can be established by combining the data measured by SD and FD. Stereo observations are even possible for a shower detected by multiple FD sites. It should also be noted that the FD

has its disadvantage in the duty cycle. The FD operation is limited to dark nights of good weather. Its duty cycle is ~ 15% for recent years, while the SD array operates 24 hours per day.

3.1.2 Water-Cherenkov Detector

Considering the UHE cosmic rays, a large detection area is required for data accumulation in an acceptable period. The surface detector array that covers 3000 km^2, offers a large aperture of 7350 $km^2 \cdot sr$ for zenith angles less than 60°. The aperture can be increased by ~30% when events with zenith angles up to 80° are included [98] . The water-Cherenkov detectors (WCD) are cylinder shaped water tanks with a sealed liner and filled with 12 tons ultra-pure water, as shown in Figure 3.3. The inner surface of the liner is composed of several layers of reflective materials. The outer layer of the liner is produced with low-density polyethylene (LDPE) films, and it is co-extruded in a sandwich structure consisting of a clear LDPE layer, a carbon-black LDPE layer, and another clear LDPE layer. Inside the outer liner, two layers of TiO_2 LDPE and DuPont TM Tyvek®1025-BL [99] are attached. This structure can both shield the external light at the outer surface and offer a good diffuse reflectivity at the inner surface. The diameter and the height of the tanks are 3.6 m and 1.2 m, respectively. Three Photonis XP1805 photomultiplier tubes (PMTs), 9 inches in diameter, are installed symmetrically on the surface of the liner and look downward into the water through clear polyethylene windows. The distance between each PMT and the center axis is 1.2 m. Such a detector system can provide a light-tight environment and diffusively reflect the Cherenkov light inside the water volume. Each WCD is self-contained and powered by a solar power supply system providing an average of 10 W for the PMTs and the electronics package.

In the operation of WCDs, the measured signals in each station are calibrated with the signal produced by the Vertical Equivalent Muon (VEM), which means the muon traversing the water tank with a vertical trajectory. During the reconstruction of the shower energy and the arrival direction, WCD signals in units of VEMs will be used to fit the lateral distribution functions.

The SD array has a multiple-level trigger system consisting of the local trigger in each detector and the shower trigger in CDAS (Central Data Acquisition System). Each single station has two levels of the local trigger, which are called T1 and T2. In the T1 level, two modes are implemented in the DAQ (Data acquisition system) system of each detector. In the first mode, a simple threshold trigger (TH-T1) is used to reduce the trigger rate (from ~3 kHz to ~100 Hz) and to select large signals. In the second mode, the “Time-over-Threshold” (ToT) trigger is employed to select small signals spread in time. The ToT rate is less than 2 Hz in each detector. In the T2 level, the global trigger rate is decreased down to ~23 Hz. ToT-T2

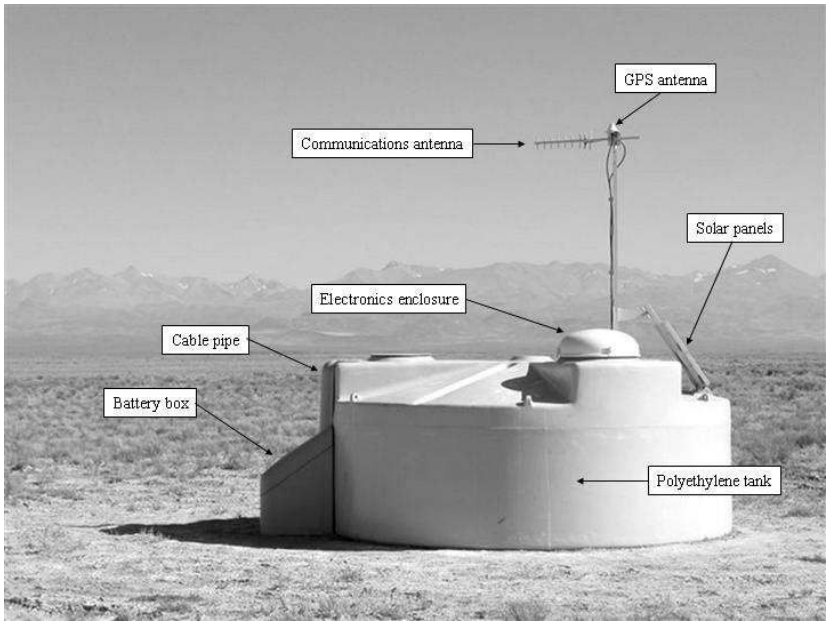

Figure 3.3 – A water-Cherenkov detector in the field, the main components are shown. This figure is taken from ref.[100]

triggers are promoted directly from ToT-T1, while TH-T2 triggers come from the TH-T1 triggers passing a higher threshold. The timestamps of T2 triggers are sent to CDAS for a further determination of the shower trigger (T3). In the T3 level, the spatial and temporal combination of T2 triggers is taken into account. Once the T3 trigger is formed at CDAS, it initiates the data acquisition and storage, thus, the FADC (Flash Analog to Digital Converters) traces from the related detectors are recorded [101].

3.1.3 Fluorescence Detector

As already mentioned, in the Observatory, there are four FD sites consisting of 27 telescopes in total. The four sites are Los Leones, Los Morados, Loma Amarilla and Coihueco. Each of the FD sites is equipped with six independent Auger FD telescopes observing the air showers with a primary energy of 10^{18} eV and above [71]. At Coihueco, besides the six Auger FD telescopes, three HEAT (High Elevation Auger Telescopes) fluorescence telescopes were installed in 2009 to the FD system for the observation of the air showers at lower energies down to 10^{17} eV [102].

The 24 Auger fluorescence telescopes, each of which has a field of view (FoV) of $30° \times 30°$. In elevation direction, the telescopes are set with a minimum of $1.5°$ above the horizon. The total FoV of one FD site is $180°$ in azimuth, as a combination of the six telescopes. As shown in Figure 3.4, the main components of the telescope are the aperture system, the UV

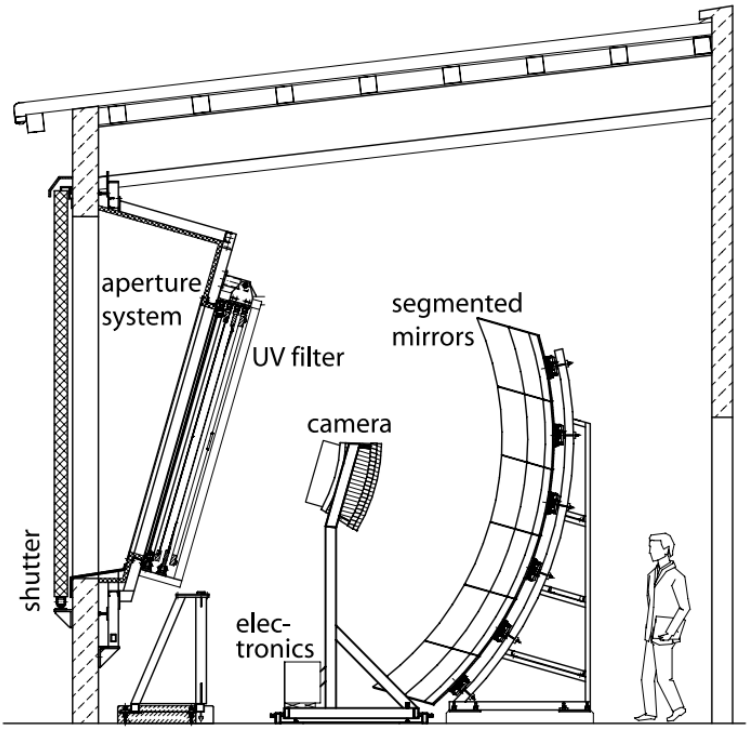

Figure 3.4 – Schematic view of a fluorescence telescope. This figure is taken from ref.[71]

filter, the segmented mirrors, the camera, and the electronics. The Nitrogen fluorescence light induced by an air shower in the atmosphere will pass the UV filter and a Schmidt optics corrector ring and then will be focused by the mirror onto the camera. The air shower will finally be imaged as a trace-like pattern on the camera with a clear time sequence. The UV filter has a transmittance of above 50% for UV light with a wavelength between 310 and 390 nm, and above 80% for 330 to 380 nm. The filter also reduces the background as its transmittance is up to 410 nm thus improving the signal-to-noise ratio of the shower events. The segmented mirrors have a total area of $\sim$10 m^2. They are installed with a spherical inner radius of 3400 mm (possible deviation up to 3420 mm). The camera consists of 440 pixels (22×22) located on the focal surface of the telescope. Each pixel corresponds to a Photonis XP3062 hexagonal photomultiplier [103] with a light collector.

3.1.4 Data acquisition

In the Observatory, a WLAN serviced by a high capacity microwave backbone network is employed to get each individual SD station connected into the communication system. The four FD sites are also connected by the backbone network to the data acquisition and control center. The data flow from the SD array will be delivered to the Central Data Acquisition System (CDAS), which is designed to combine local trigger information from the SD stations

for identifying potential shower events. The FD data are recorded in each FD station and delivered daily to the computer center in Malargüe. During the daytime, FD and SD data are merged for the hybrid coincidences. The newly acquired data are synchronized on the central storage hardware after each night and mirrored to the IN2P3 Computer Center in Lyon, France.

3.1.5 Event reconstruction

In the FD reconstruction, the longitudinal development of the shower is estimated with the Gaisser-Hillas (G-H) function [43].

$$f_{GH}(X) = \left(\frac{dE}{dX}\right)_{X=X_{max}} \left(\frac{X - X_0}{X_{max} - X_0}\right)^{\frac{X_{max}-X_0}{\lambda}} e^{\frac{X_{max}-X}{\lambda}} \tag{3.1}$$

where X_{max} is the depth of the shower maximum size. X_0 and λ are shape parameters. The number of photoelectrons detected by the FD camera will be compared to the expectation of the G-H function with a log-likelihood fit. In this fit, the effects of the light yield, atmospheric transmission, lateral distribution and detector response are taken into account. The reconstructed energy, E_{FD}, of the shower can be obtained as an integral of the G-H equation. A correction is finally added to the E_{FD} for the energy carried by the "invisible" components like high-energy muons and neutrinos in the shower development [104].

The events triggered by the SD array need at first to pass the physics level trigger (T4). T4 trigger selects the real showers from T3 events, which includes background signals from low energy air showers. An additional trigger (6T5), which ensures that the highest signal is surrounded by 6 operating neighbors, can be used to guarantee a well-contained event for an accurate reconstruction.

After the event selection, the arrival direction will be obtained by fitting the start time of each SD signal to a plane front. The shower core on the ground can be obtained from the fits of the SD signals. The lateral distribution function (LDF) of a certain air shower can be described as a modified NKG function [37, 38]:

$$S(r) = S(r_{opt}) \left(\frac{r}{r_{opt}}\right)^{\beta} \left(\frac{r + r_1}{r_{opt}}\right)^{\beta+\gamma} \tag{3.2}$$

where r_{opt} is the reference distance, $r_1 = 700$ m and the $S(r_{opt})$ is an estimation of the shower size. The spacing of stations is 1500 m for the regular SD array. The r_{opt} is chosen to be 1000 m where the shower fluctuation is estimated to be minimum [105]. The parameters β and γ are related to the zenith angle and the shower size.

The measured $S(1000)$ mainly depends on the shower energy, the attenuation of shower particles and the geometrical effects. For a given energy, $S(1000)$ relatively decreases when

the zenith angle (θ) of the shower increases. Thus, the $S(1000)$ can be converted to a reference term, S_{38}, for energy reconstruction.

$$S_{38} = \frac{S(1000)}{f_{CIC}(\theta)}$$

S_{38} can be understood as the signal produced by the particular shower with the size of S(1000) and arriving at $\theta = 38°$. The $f_{CIC}(\theta)$ describes the attenuation curve with the Constant Intensity Cut (CIC) method [106] and fitted with a third-degree polynomial. S_{38} is an estimator of the shower energy obtained independently with the SD array. Combining together the primary energy, E_{FD}, reconstructed by the FD and S_{38}, a power-law relationship can be described as:

$$E_{FD} = A \left(\frac{S_{38}}{VEM} \right)^B$$

where the parameters A and B are fitted on the data and are found to be $A = (1.90 \pm 0.05) \times 10^{17}$ eV and $B = 1.025 \pm 0.007$ [107, 108]. In the reconstruction of hybrid events, the resolution of E_{FD} is ~8%, and the systematic uncertainty is around 15% at an energy of several EeVs [32, 109].

3.2 Scientific goals of the AugerPrime project

Rich science outcomes concerning the ultra-high-energy cosmic rays (UHECRs) have been yielded from the Observatory in the last decade. Even so, there are still a series questions that remain open and need to be addressed. First of all, the flux suppression of the all-particle spectrum at the highest energy [107] has not been explained clearly. Almost all UHECR models ascribe the flux suppression above $4{\times}10^{19}$ eV to propagation effects. As there are some differences related to the index of the power-law spectrum and the mass composition among the models, different interpretations have been considered for the origin of the ankle [110–117]. Secondly, the hypothesis of an additional proton component appearing at very high energy range (~$4{\times}10^{19}$ eV) [118] needs to be precisely investigated. The major limitation for studying these open questions is the lack of composition data. By proposing the AugerPrime project, the collaboration aims at upgrading the Observatory for an advanced shower-by-shower measurements on the mass composition of UHE cosmic rays [119].

The main goals of AugerPrime can be described as followings:

- Elucidate the mass composition and the origin of the flux suppression at the highest energies. This is the primary objective of AugerPrime evolved from the primary motivation of the Pierre Auger Observatory to search for a GZK-like (Greisen–Zatsepin–Kuzmin) flux suppression. A series of studies would be established under this objective, such as,

the differentiation between the energy loss effects induced by the propagation, and the maximum energy of particles from astrophysical sources.

- Search for a flux contribution of protons up to the highest energies. The measurement of the proton fraction is crucial for estimating the physics potential of the current and future cosmic-ray detectors and clarifying the prospects of proton astronomy.

- Study extensive air showers and hadronic multiparticle production at the ultra-high energy range. The determination of the mass composition of UHECRs highly depends on hadronic interaction models. Reversely, determining the mass composition of UHECRs would allow us to explore the fundamental particle physics at the highest energies, which can not be generated in current man-made accelerators.

To fulfill these objectives, the collaboration, with the AugerPrime upgrade, foresees to add scintillator surface detectors (SSD) mounted above the existing water Cherenkov detector (WCD) to provide a complementary measurement of the muon density of the extensive air showers [119]. As the WCD and the SSD have different sensitivities for electromagnetic and muonic components of the air showers, their signals measured independently for a given shower can be used for decomposing the components. Therefore, this upgrade is expected to improve the sensitivity of the surface detector array to the mass composition. The main path for the identification with AugerPrime would be, at first to use the signals and the timing information from the SD array to deduce the primary energy and related muonic parameters, and then to determine the primary particle with these parameters.

In the study of the shower development, X_{max} and the number of muons at X_{max}, N^{μ}_{max}, are two key parameters. Figure 3.5 shows simulated N^{μ}_{max} and X_{max} and their correlations for showers induced by proton, Helium, Nitrogen and Iron, respectively. Clear separations are shown in the contours and the histograms of N^{μ}_{max} and X_{max} for different mass composition. This indicates that the primary mass of the air showers can be inferred based on their signature in the X_{max} and N^{μ}_{max} plane.

The “universality” of showers describes the average properties of the shower cascade in terms of primary energy and shower age [120]. It can be deduced from the overall shape and the time profiles of the particles arriving at the ground level, in spite of the complex interactions in the shower development. For the electromagnetic component of showers, a series of studies have been reported concerning the "universality" [120–124]. Following this experience, an additional parameter named the muon scale, N_{μ} [125–127] can be introduced to describe the hadronic showers. According to the simulation results presented in Figure 3.5, we can easily realize that it is crucial to increase the detector resolution for better measuring

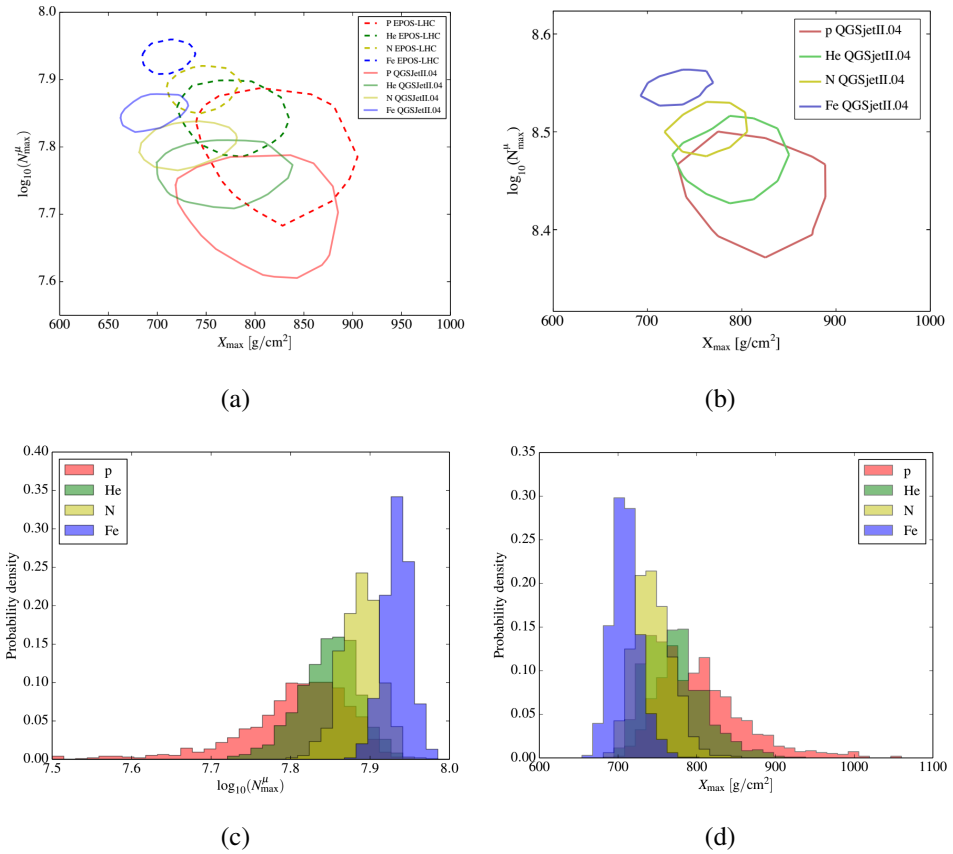

(a) (b)

(c) (d)

Figure 3.5 – Simulations with different hadronic models show clear separations for different mass compositions in the graphics of X_{max} and N^{μ}_{max}. 3.5(a) and 3.5(b) are the contour plots of $\log_{10}N^{\mu}_{max}$ vs. X_{max} for the air showers (θ=38°) with energies of 10^{19} eV and 5×10^{19} eV, respectively. 3.5(c) and 3.5(d) are the histograms of $\log_{10}N^{\mu}_{max}$ and X_{max}, respectively, for the air showers (θ=38°) with energies of 10^{19} eV (EPOS-LHC as the hadronic model). These figures are taken from [119].

the event-by-event correlation of X_{max} and N_{μ}. Furthermore, one expects to describe the air showers initiated by charged particles or photons with only three parameters E, X_{max} and N_{μ}.

3.3 AugerPrime implementations

The AugerPrime implementations include three main elements:

- **The Scintillator Surface Detectors (SSD) mounted above the existing WCDs**[128] This is the main component of the project. The design of SSD by the collaboration is introduced in subsection 3.3.1.

- **The Surface Detector Electronics Upgrade (SDEU) for surface detectors (WCD+SSD)**[129]

Along with the scintillator detectors, an essential component is the new electronics named Upgraded Unified Board (UUB), which is designed to record and process the signals from both WCD and SSD. Additionally, to extend the dynamic range of the existing WCD, a small PMT (SPMT) will be added into each WCD and will work together with the three large PMTs. In subsection 3.3.2, the main features of SDEU are introduced.

- **The current AMIGA (Auger Muons and Infill for the Ground Array) project**
  AMIGA is the sub-array of underground muon detectors co-located with the Auger Infill SD array [130]. It aims at extending the energy range of the primary particles to $3{\times}10^{17}$ eV at the Observatory [131]. Together with WCD and SSD, the muon detectors of AMIGA are expected to serve as a cross-check of the muon estimation techniques. The detailed information of AMIGA concerning the science case, the R&D and the progress of the project can be found in ref.[130–134].

3.3.1 The Scintillator Surface Detector

Figure 3.6 – Water-Cherenkov detector with a scintillator detector on top.

Figure 3.6 shows a photo of the AugerPrime SD detector. The SSD is mounted on top of the WCD. The new SSD basic unit consists of two modules of $\simeq 2$ m^2 extruded plastic scintillator, read out by wavelength-shifting (WLS) fibers coupled to a single photomultiplier tube (PMT) placed between them. The choice to collect the scintillation light by means of optical fibers on a single photodetector represents a cost-effective solution to reduce the number of read-out channels, especially for a large detection area. The active part of each module is a scintillator plane made by 24 pieces of 1.6 m-long plastic scintillator bars (see in

Figure 3.7). For large size detectors, WLS fibers are usually needed to deliver and collect the scintillation light towards the photodetector, to avoid the light attenuation effect in the plastic scintillators. The use of WLS is even more necessary when extruded scintillators are employed in the detector assembly, because of their reduced optical quality. As the SSD detector needs to operate for at least 10 years in the field, with strong winds and daily temperature variations of up to 30°C, it is required to be reliable, easy to realize and install, and operating with minimal maintenance. Therefore, the techniques employed in the SSD are all well understood and widely applied in large-scale experiments.

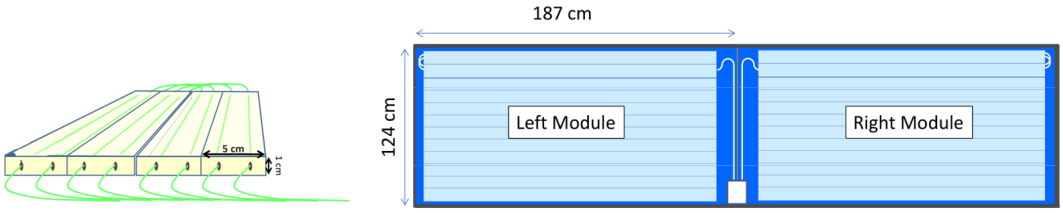

(a) (b)

Figure 3.7 – The module of scintillators 3.7(a) and WLS fibers and the SSD layout 3.7(b).

Once a particle passes through the detector, the light signal is emitted in the scintillator, then delivered by the WLS fibers, towards the PMT entrance window.

Plastic scintillator The plastic scintillators used to equip the SSD have a cross-section of 50×10 mm^2 with 2 holes to embed WLS fibers, as shown in 3.7(a). They are produced with the extrusion technique at the Fermi National Accelerator Laboratory (FNAL). This type of scintillators has been employed in several experiments [135].

Wavelength-shifting (WLS) fibers In SSDs, WLS fibers are inserted into the holes and turned into a U-route at the end of scintillators with a bending diameter of 10 cm. Fibers outside of scintillators are embedded in the fiber routers to be kept in place and protected from breaking. The WLS fiber ends are coupled to a PMT entrance window with an optical coupling module. In SSD configuration, the baseline option for WLS fibers is the Kuraray Y11 (300) MSJ (⊘ 1.0 mm) [136].

PMT and power supply The baseline PMT for SSD is the Hamamatsu R9420-10 (1.5″ diameter) [137], which has a 38 mm bialkali photocathode and 8 stages of multiplication. This type of PMT has a good quantum efficiency in the green region, which is the wavelength range of fiber emission. The high voltage for the PMT is supplied by means of a CAEN HV

module [138] or an ISEG base [139] and connected with an RG59 type coaxial cable. The HV module is located on top of the UUB enclosure. The signal of SSD is connected to the corresponding UUB with an RG58 type cable.

During the R&D phase of SSD, several candidate scintillator/WLS fiber configurations for SSD have been considered. The current detector configuration, as introduced in the previous paragraphs, was chosen based on a series of measurements and studies of the detector components. The IPN-Orsay group has been involved in this R&D activity, related contents will be discussed in chapter 4.

The whole detector is placed in an aluminum box which is designed to guarantee enough robustness for at least 10 years of operation. The PMT module of the detector is fixed with 4 screws and removable for maintenance. The whole detector is maintained in place with supporting bars, which are connected to the WCD using lifting lugs present on the tank structure. In 2016, the first batch of SSD detectors was produced at the Karlsruhe Institute of Technology (KIT), then transported to Argentina and finally installed in the AugerPrime engineering array in September. They have been in operation since October 2016, the SSD performance and the calibration with minimum ionizing particles (MIPs) are introduced in chapter 5.

3.3.2 Surface Detector Electronics Upgrade

The Surface Detector Electronics Upgrade (SDEU) aims at increasing the data quality, to enhance the local trigger and processing capabilities and to improve calibration and monitoring capabilities of the Surface Detector stations. The implementation of SDEU allows us to replace the old Surface Detector Electronics (SDE), which has been employed for more than 15 years, with a newly designed single board, named the Upgraded Unified Board (UUB). The UUB includes all the functionalities required by the SDEU specifications. The UUB is designed based on the current technology and has a faster sampling for ADC traces, a better timing accuracy, and an increased dynamic range compared to the old electronics in the SD station. Furthermore, the UUB also has interfaces for the scintillator detector and the added small PMT in the WCD. Figure 3.8 shows one of the UUB prototypes.

UUB features The signal from the anode of the PMTs is split into low-gain and high-gain channels. The high-gain channel is amplified by a factor of 32. The signal in SSD LG channel is divided by a factor of 4. Therefore the WCD and SSD HG-to-LG ratios are 32 and 128, respectively. After the amplification, signals are filtered and digitized by 12bit 120MHz AD962 Flash ADCs (FADC). This type of FADC has a low power consumption with rather

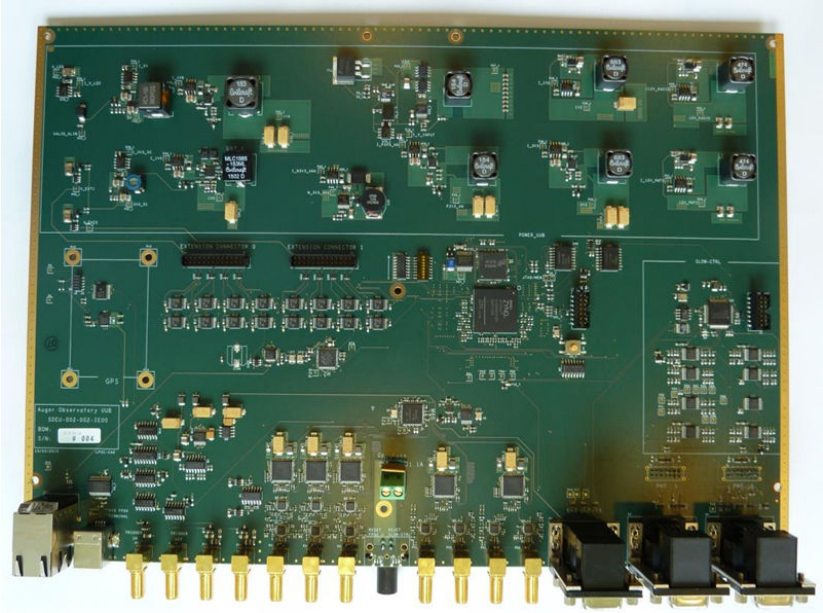

Figure 3.8 – UUB prototype

good performance in terms of signal digitization and signal sampling, which commendably fits the specification of the SD station with a total power budget of ~10 W. All these components are designed to be integrated into the UUB architecture, which is based on a Xilinx Zynq FPGA (field-programmable gate array). The FPGA carries two ARM Cortex A9 333MHz micro-processors, a 4G-bit LP-DDR2 memory and a 2G-bit Flash memory (storage memory) as the core components for signal processing [129].

Dynamic range of WCD Figure 3.9 shows the global dynamic range for the WCD signals. The anode signals from the large PMTs are split into the high-gain (HG) and low-gain (LG) channels. In the HG channel, the signal is amplified with a gain of ~32. These amplified signals can be used for the VEM calibration or be used for shower event measurements. The signals from the channels which are not amplified can be used for measuring large signals in shower events. With these two channels for the large PMTs, the dynamic range is up to 17 bits. The channel connected to the small PMT is designed to process the very large signals in case large PMTs are saturated for the signals induced in the WCD close to the shower core. It covers a dynamic range up to 22 bits. Compared to the dynamic range of old electronics, the dynamic range in this design has an increase of 7 bits allowing us to measure the events as close as about 200 m from the shower core.

Dynamic range of SSD Figure 3.10 shows the global dynamic range for the SSD. The anode signal from the SSD PMT is split into two channels. One channel amplifies the signals

Range	Intent	Dynamic Range																					
bits		1	2	3	4	5	6	7	8	9	10	11	12	13	14	15	16	17	18	19	20	21	22
LowGain	VEM	AnodeX32																					
HighGain	Showers						Anode																
VeryHighGain	Cores											SPMT											
Ipeak (mA)		0.0006					0.02		0.08			1.2						40					
Vpeak (mV)		0.03					1		3.9			64						2000					
Ipeak SPMT (mA)												0.02						1.25				40	
Vpeak SPMT (mV)												1						64				2000	
Npart (VEM)		0.01					0.3		1.2			10						600				20000	

Figure 3.9 – WCD dynamic range [119]

with a gain of ~32 and the other one divides the signals by a factor of 4. This aims at extending for a full range up to 19 bits. The sampling and filtering process for SSD signals is similar to that of WCD signals.

Range	Intent	Dynamic range																	
bits		1	2	3	4	5	6	7	8	9	10	11	12	13	14	15	16	17	18	19
LowGain	MIP	AnodeX32																		
HighGain	Showers								Anode/4											
Ipeak (mA)		0.0006				0.01			0.1				1.25			10				160
Vpeak (mV)		0.03				0.5			4				62.5			500				8000
Npart (MIP)		0.07				1.2			10				156			1250				20000

Figure 3.10 – SSD dynamic range [119]

For the timing aspect of the UUB, an advanced GPS Receiver by I-Lotus, LLC (Singapore) [140] is employed. It offers an accuracy of ~4 ns, which satisfies the UUB specification of $\leqslant$ 5.0 ns. A new slow control system similar to that of AERA (The Auger Engineering Radio Array) is used in the UUB. A USB serial connector is integrated in this module, which offers the convenience for controlling and maintaining the SD station. Furthermore, the corresponding slow control software is capable to deal with more than 90 monitoring variables, which can afford for a comprehensive study of the monitoring data.

In October 2016, the first batch of UUB board prototypes was deployed in the AugerPrime engineering array (EA). The performances of the AugerPrime EA and the analysis of the first data are introduced in chapter 5.

4

R&D for AugerPrime scintillator detectors

In section 4.1 of this chapter, the general components of a plastic scintillator detector are introduced. The R&D work for AugerPrime SSD by the author is presented in section 4.2, including the tests of candidate SSD components and related discussions on the results. In the section 4.3, a design of the fiber/PMT optical coupling module for SSD with polished fiber ends is introduced, including the fabrication procedures and the preliminary results of the test on the SSD equipped with this type of coupling module.

4.1 General components of plastic scintillator detectors

A scintillator detector is mainly composed of scintillators coupled through a light collection element to photodetectors. The most important advantage of plastic scintillator detectors is the broad adaptability to the environment. Besides the general characteristics in detector performances, plastic scintillator detectors also have an appreciable cost effectiveness. Therefore, it is widely used as particle detectors in cosmic-ray experiments. The general components of plastic scintillator detectors for cosmic-ray detection are introduced as follows:

4.1.1 Plastic scintillators

Plastic scintillators are generally composed of three parts: the plastic substrate, the first scintillation material, and the wavelength-shifting agent. The first scintillation material and the wavelength-shifting agent are dissolved in each plastic monomer and the monomers are polymerized to form the scintillators. The plastic substrate receives radiation energy and transfers energy to the first scintillation material. The first scintillation material has a very high quantum efficiency and is a major luminescent substance that emits photons at the wavelength around 360 nm. The wavelength-shifting agent absorbs these photons and emits photons at around 420 nm.

Plastic scintillators have been widely applied and rapidly developed since they were invented, due to their many advantages listed as follows [141–143]:

- **Easy to process** Plastic scintillators can be easily processed and made into a variety of shapes to meet the needs of different situations.

- **Good stability** The plastic substrate has a good physical and chemical stability, this makes scintillators usable under harsh conditions.

- **Fast time response** A large proportion of hydrogen in its composition makes plastic scintillators having a very short decay time, generally less than 10 ns. Therefore, the detectors made of plastic scintillators always have excellent time resolutions.

- **Low cost** The cost of plastic scintillators are usually very low since more than 95% of the components are plastic substrates.

- **High transmittance** In plastic scintillators, the loss of light in the transmission process is small, and the luminous efficiency is very high.

- **Low self-absorption** The self-absorption of light in plastic scintillators is kept at a very low level, due to the chemical shift between its absorption and emission spectra. This lead to a high conversion rate from the energy released by the incident particles to the light yielded by the scintillator.

However, plastic scintillators also have some drawbacks. For example, the small density and low effective atomic number lead to a relatively low detection rate for heavy particles, and a low efficiency of γ-ray detection. Therefore, in cosmic-ray experiments, they are often used as detectors for the electromagnetic component of the air showers.

4.1.2 Wavelength-shifting fibers

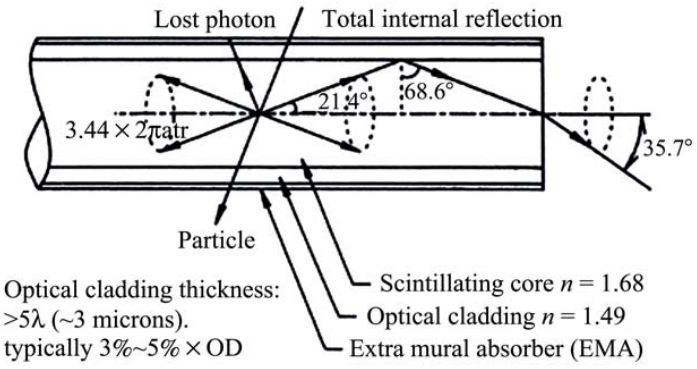

Figure 4.1 – Structure of wavelength shifting fibers [144]

The wavelength-shifting (WLS) fiber is generally an important part of the scintillator detectors. It is composed of two parts: the core layer and one or more cladding layers, Figure 4.1. The working principle of WLS fibers is that the wavelength-shifting material in the core absorbs the incident photons and is excited. The excited atoms emit light with longer wavelengths over a 4π space solid-angle. When the photon's exit angle (the angle between the exit direction and the normal to the interface) is larger than the critical angle, a total reflection occurs. The total reflection photon is transmitted to both ends of the fiber and is received by the photodetectors. Compared to the ordinary fibers, there is no dependency on the incident angle of the photon for the light signal readout in WLS fibers. Therefore, WLS fibers can be coupled to the scintillators through the sides of fibers, thereby, reducing the deployed number of fibers and saving the cost. As a crucial component, the technical parameters of WLS fibers such as light attenuation length, light loss rate and light absorption and re-emission efficiency, directly affect the total performance of the detector.

4.1.3 Photoelectric conversion devices

Photoelectric conversion devices used in this type of detectors are generally photoelectric tubes or photomultiplier tubes (PMT). In some new designs of detectors, semiconductor optoelectronic devices, with high quantum conversion efficiency, low power consumption and a smaller size than traditional vacuum tubes have been applied to miniaturize the detectors and improve the spatial resolution. Microchannel plates (MCP) are also used as the photoelectric conversion device in some experiments, which can offer the detectors a high sensitivity, good time characteristics and a precise position resolution.

4.1.4 Detector design

The practical design of scintillation detectors should take into account the following factors:

- The emission wavelength of the scintillator or the WLS fiber should match the sensitive response region of the photoelectric conversion devices to assure a high detection efficiency.
- In order to offer a high light output to the photodetector, the light collection efficiency has to be optimized.

R&D studies have been carried out in order to optimise the detector configuration balancing the total production cost, the detector performance, and the long-term stability. The R&D studies carried out at IPN-Orsay are presented in the next section.

4.2 Test of candidate SSD components

The specification of SSD performance requires the signal of MIP charge ≥12 p.e. after 10 years of operation. According to the previous studies on the aging of scintillator detectors, the total light loss over 10 years of operation is estimated to be 30% [119]. Therefore, the MIP signal produced by a new SSD is expected to be ≥17.1 p.e. The basic aim of the R&D study is to select out a proper configuration of the SSD detector which satisfies this specification and is also cost-effective and reliable.

During the R&D phase of the SSD detector, our group at the IPN-Orsay and the RDD (R&D Détecteurs) division of our laboratory were involved in the study of scintillator-fiber-PMT configurations together with Auger collaborators from KIT[1], INFN-Lecce[2] and other laboratories. We report on the light-yield measurements we performed for different candidate scintillator/fiber configurations (see subsection 4.2.3, subsection 4.2.4). The aim was to investigate the effect of the scintillator fabrication methods (extruded or casted), the profile and geometry of the bars, and the particular type of WLS fiber to the collected light yield for the different tested configurations. By using a numerical method, we also estimated the light-collection efficiency of scintillators with different profiles to explain the experimental results (see subsection 4.2.6). Finally, we present the results on the light-collection efficiency for a variety of optical coupling methods, tested with the aim to optimize the matching between the fiber ends and the PMT entrance window (see subsection 4.2.7).

4.2.1 Plastic scintillator, WLS fibers, and optical coupling

The plastic scintillator samples tested in this study were procured by the Fermi National Accelerator Laboratory (FNAL) and the Chinese Gaonengkedi (GNKD) Company. All samples have been cut to a length of 20 cm for comparison. The FNAL scintillators, which have been already used in several large-scale experiments [135], are produced with the extrusion technique. The maximum emission in the fluorescence spectrum of the FNAL scintillators is around 420 nm [145]. The extrusion technique works in the way of pushing the scintillation material out of the extruder through a die of the desired cross-section. The FNAL extrusion line is active since 2003. A. Pla-Dalmau et al. have demonstrated the effectiveness of the extrusion technique in ref.[146]. For extruded scintillators read out with WLS fiber, the authors measured a light output comparable to that obtained with the Polyvinyltoluene based Bicron BC-404 scintillator.

[1] Karlsruher Institut für Technologie
[2] Istituto Nazionale di Fisica Nucleare - Lecce

In this work, we tested in total 6 types of scintillator bars from FNAL (at least two sample bars for each type), provided with different cross-section dimensions and geometry for the WLS fiber hosting:

- 40 mm × 10 mm lateral dimension with one v-shaped groove
- 40 mm × 10 mm lateral dimension with one hole
- 45 mm × 10 mm lateral dimension with two holes
- 50 mm × 10 mm lateral dimension with two holes
- 50 mm × 20 mm lateral dimension with two holes
- 100 mm × 10 mm lateral dimension with four holes

The GNKD company provided three bars of two types, two produced with standard casting technique and one with extrusion technique [147]. The maximum emission of GNKD scintillators is also around 420 nm [148]. The cross-section geometries of the GNKD scintillators are listed as follows:

- 40 mm × 10 mm lateral dimension with one Ω-shaped groove
- 40 mm × 20 mm lateral dimension with one Ω-shaped groove (casted)

Figure 4.2 summarizes the geometric characteristics of the scintillators tested in this work, including the provider, the fabrication technique, the cross-section view and the dimension of each sample. The FNAL samples are all coated with TiO_2 white reflective/diffusive material. The GNKD samples are wrapped with Teflon tapes to improve the light collection on the photodetector.

In this work, we used WLS fibers BCF-91-A and BCF-99-29-AMC (⊘ 1.2 mm) from Saint-Gobain [144] and Y11(200)-MSJ, Y11(300)-MSJ (⊘ 1.0 mm) from Kuraray [136]. BCF-91-A has a single-cladding structure while the other three have multi-cladding structures. All tested fibers are blue-to-green shifters, but they have slightly different light absorption and emission spectra. In particular, the light absorption and emission maxima are at 420 nm and 494 nm respectively for BCF-91-A, at 410 nm and 485 nm for BCF-99-29-AMC [132] and at 430 nm and 476 nm for Y11 fibers.

Figure 4.4 shows the spectra of absorption/emission spectrum of the Kuraray Y11 fibers and the emission spectrum of FNAL scintillator. The emission peak of FNAL scintillators is around 420 nm, and the absorption/emission peaks of Kuraray Y11 fibers are 430 nm and 476 nm, respectively. The absorption spectrum of the fibers matches well with the emission

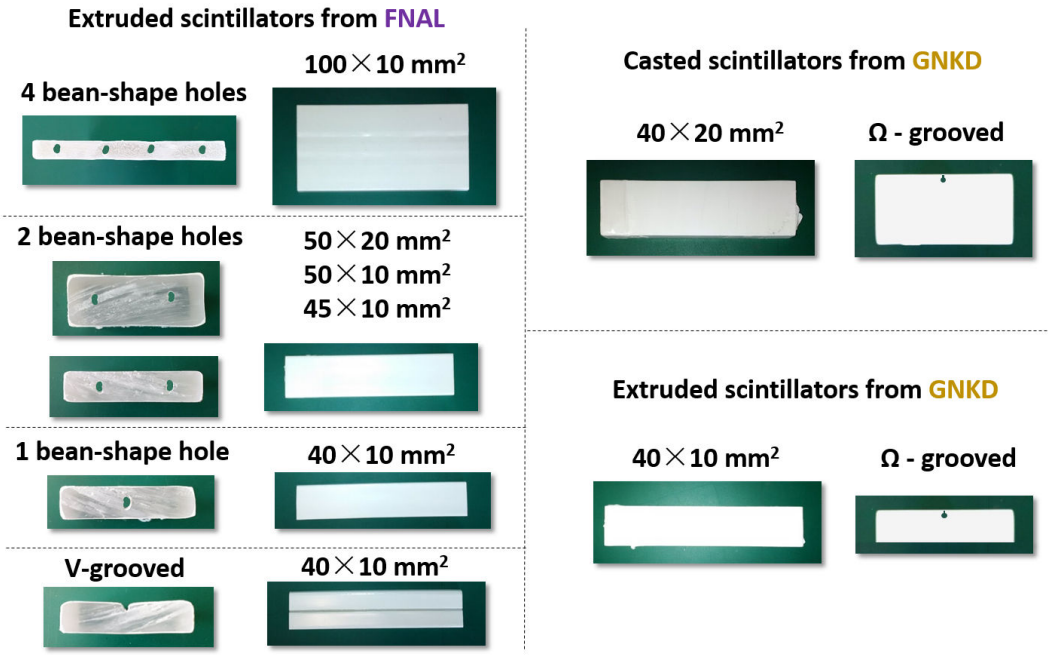

(a)

Provider	Fabrication technique	Dimension (mm)	Cross-section
FNAL	extruded	100×10	
FNAL	extruded	50×20	
FNAL	extruded	50×10	
FNAL	extruded	45×10	
FNAL	extruded	40×10	
FNAL	extruded	40×10	
GNKD	extruded	40×20	
GNKD	casted	40×10	

(b)

Figure 4.2 – Plastic scintillators studied in this work

spectrum of scintillators. The fiber emission spectrum is shifted to a larger wavelength range and separated from the fiber absorption, this allows a long attenuation length for delivering the light.

The different scintillator/fiber tested configurations are presented in Figure 4.3. As shown in the picture, one end of each fiber is coupled the PMT entrance window and then run along the grooves or holes of the scintillator bar samples. The other end of the fiber is cleft (so-called the "cut" mode) at the end of the scintillator bar or "U-routed" towards the PMT again. The bending diameter for U-route is kept at 10 cm, thus assuring the light loss in the bending lower than 5% [136]. For each configuration, 50 cm of fibers are reserved between the scintillator and the PMT entrance window. The fiber ends are polished with 800 and 1200-grit sandpapers

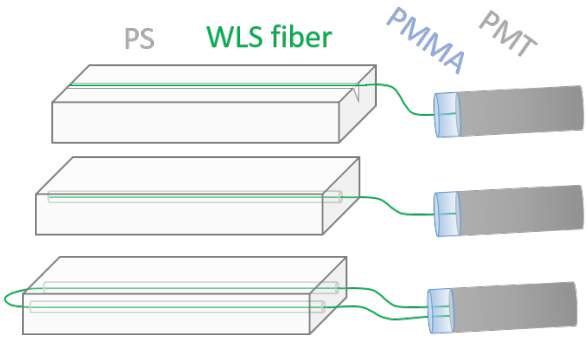

(a)

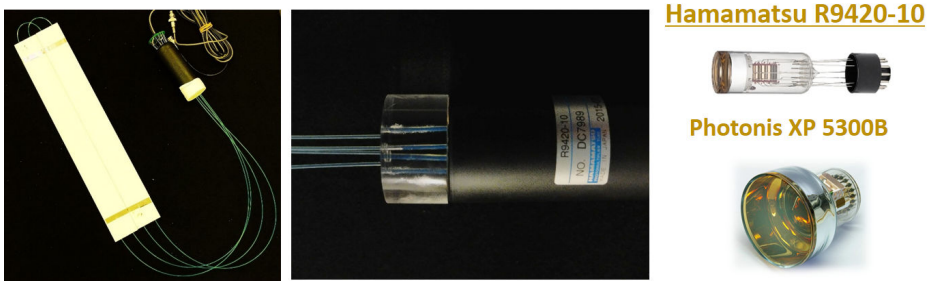

(b)

Figure 4.3 – Plastic scintillator/WLS-fiber configurations connected to a PMT by means of a PMMA support

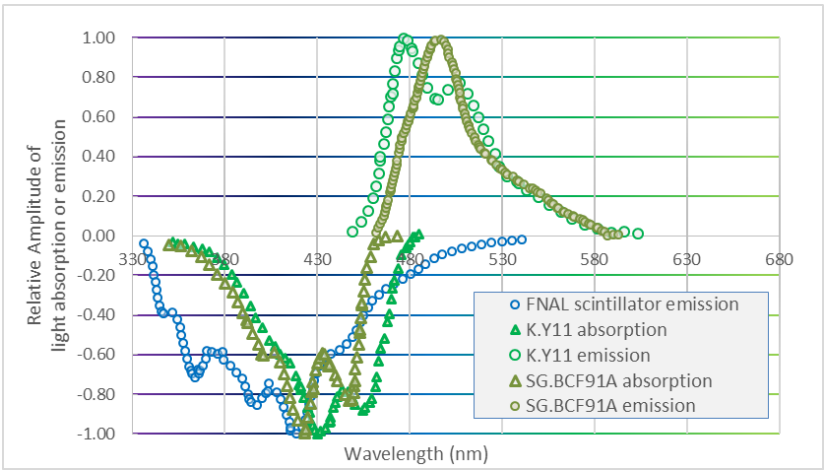

Figure 4.4 – The absorption/emission spectra of FNAL scintillators, Kuraray Y11 and Saint-Gobain WLS fibers

and kept in place in front of the PMT window by means of a drilled PMMA cylinder. We tested two different optical couplants to assure a good optical matching between the fiber ends and the PMT entrance window. In particular, we used Dow Corning Q2-3067 grease [149] and Rhodorsil RTV 141 A&B silicone [150]. The RTV silicone is fabricated by mixing two

reagents (A and B) with a ratio of 100:10. After a full mix of the reagents, the RTV silicone is cast into a pad-shape aluminum mold and let for a curing time of 48 hours. The silicon pad that we produced for this test is 6 mm thick. Four holes with a depth of 3 mm are drilled on it to contain the fiber ends.

In our work, VM2000 (reflector) and Teflon tape (diffuser), have been employed as wrapping materials around the fiber/PMT coupling part to increase the light-collection efficiency (LCE). The reflective coefficients of Teflon tape and VM2000 are reported to be larger than 90% and 95% around 440 nm, respectively [151].

Gluing fibers in scintillator grooves is observed to offer serious advantages in terms of the light collection with respect to the normal fiber hosting. On the other hand, the process of gluing the fibers might be difficult and time-consuming, especially for certain types of glues that require long curing time. In order to investigate the effect of gluing the fibers in the scintillator grooves, we employed Saint-Gobain BC-600 optical glue and Dow Corning 3145 silicone glue. At room temperature, the curing time for these two types of glue is about 24 and 48 hours, respectively.

4.2.2 PMT and test bench

In this work, two different PMTs have been employed to read-out the scintillation light: the R9420-10 by Hamamatsu (1.5″ diameter) [137], which is the baseline PMT of SSD design, and the XP5300, which is a high quantum efficiency PMT from Photonis (3″ diameter) [103]. Both PMTs have been calibrated with a LED (blue light) and supplied with a high voltage of 1100 V corresponding to a gain of 5.2×10^5 and 3.9×10^5 for the R9420-10 and the XP5300, respectively.

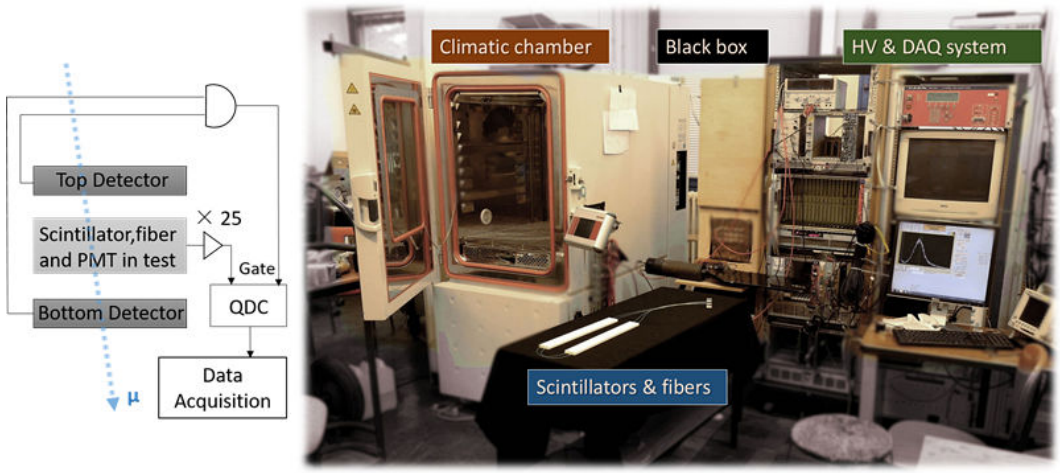

Figure 4.5 – Test bench scheme

A schematic view of the test bench realized for this study is presented in Figure 4.5. The scintillator detector, coupled to the PMT, is placed in a black box and two plastic scintillator paddles, laying above and below the black box, are used as the trigger for the acquisition: the signal coincidence of these two detectors provides the gate to a QDC (Charge-to-Digital Converter). This way every time a minimum ionizing particle (MIP) gets across the telescope. The QDC registers the total charge of the signal produced by the scintillator under test. The charge histograms are then fitted with a Landau distribution. The most probable value (MPV) of the Landau fit provides an estimate of the number of photoelectrons (p.e.) produced at the PMT photocathode.

4.2.3 Plastic scintillator tests

We tested the light yield for the different scintillators. In this set of tests, the type of WLS fibers employed is Kuraray Y11(200)-MSJ, 1.0 mm in diameter, and the PMT used is XP5300B. Aluminium tapes have been used to fix and cover the fibers in the grooved scintillators. For all the assembled detectors we used Dow Corning optical grease as couplant and Teflon tape as wrapping material to optimize the light collection at the fiber/PMT interface. Table 4.1 lists the signal amplitude at the peak of the muon spectra (in p.e. number) for each tested configuration. The spectra of the configurations i.d. #2, #4, and #5 are shown in Figure 4.6. The main effects on the signal amplitudes are summarized as follows:

- Thickness effect: For similar geometry, a 2-cm-thick scintillator provides $\sim 60\%$ larger signal than a 1-cm-thick one (comparison between sample i.d. #2 and sample i.d. #4)

- The effect of fiber deployment density: For similar geometry, we measured a $\sim 50\%$ larger signal when two fibers, instead of one, are inserted in the scintillator sample (comparison between sample i.d. #4 and #5).

- The effect of "U-route": The "U-route" fibers provide $\sim 64\%$ more photoelectrons than the cut ones (comparison between sample i.d. #3 and #4).

- Fiber hosting in the scintillator: We obtain essentially similar results for scintillator bars equipped with a groove or a hole for the WLS fiber hosting (comparison between sample i.d. #5 and #6).

- The effect of gluing fiber in the grooves on scintillators: If we use optical glue in the scintillator groove, the light-collection efficiency improves considerably, in particular, we observed an improvement of $\sim 64\%$ and $\sim 38\%$, when using BC-600 and silicon glue, respectively (comparison between sample i.d. #7 and #8).

- The effect of providers: Our test shows that the performance of GNKD extruded scintillator is close to the FNAL corresponding one, with a similar shape (sample id. #6 and i.d. #9).

- The effect of production techniques: For the casted GNKD scintillator samples (i.d. #10) we measured a signal amplitude of ~ 50 p.e. A direct comparison between casted and extruded scintillator cannot be realized as we had no 1-cm-thick casted sample available for testing. Anyway, as previously discussed, we can estimate the thickness contribution to the light yield improvement to be ~ 60% , when passing from 1-cm-thick to 2-cm-thick scintillators. So, if we take into account this contribution, then we can estimate that the signals produced by casted scintillator are roughly a factor of ~1.9 higher that the signals produced by the extruded ones for GNKD scintillators with similar geometry.

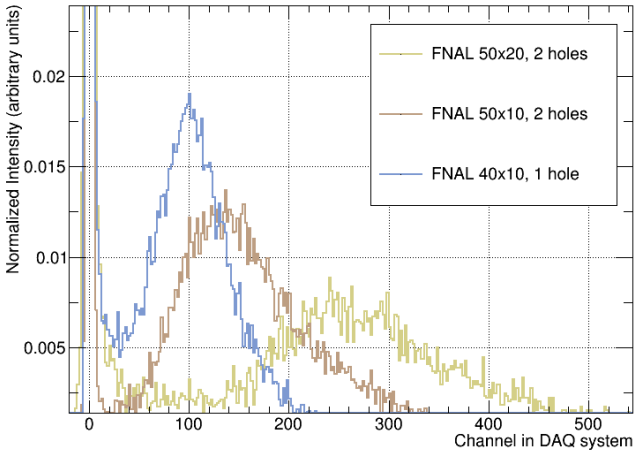

Figure 4.6 – Cosmic muon spectra measured with FNAL 50 × 20 mm^2 2-hole, 50 × 10 mm^2 2-hole, and 40 × 10 mm^2 2-hole scintillators equipped with "cut" mode fiber configuration. The intensities of spectra are normalized by the total number of counts of particles in each spectrum.

Scintillators fabricated with casted technique, having a higher thickness and deployed with more pieces of fibers can certainly yield more photoelectrons than others. In the AugerPrime SSD specifications, the detector is expected to have a minimized weight, an appreciable light yield (> 12 p.e.) and a stability in a hostile environment, with strong winds and daily temperature variations of up to 30 °C [119]. A final choice of FNAL 50 × 10 mm^2 2-hole scintillators was made, as it yields a number of photoelectrons that satisfies the detector's

No.	Scintillator profile (mm)	Fiber end & glue in groove	Results (p.e.)
1	FNAL 100×10, 4 holes	cut	26.7 ± 1.4
2	FNAL 50×20, 2 holes	cut	42.3 ± 1.9
3	FNAL 50×10, 2 holes	U-route	43.7 ± 1.9
4		cut	26.6 ± 0.6
5	FNAL 40×10, 1 hole	cut	18.0 ± 0.4
6	FNAL 40×10, 1 Groove	cut	18.8 ± 0.5
7		cut, D.C.3145	26.0 ± 0.2
8		cut, BC600	30.9 ± 0.9
9	GNKD 40×10, 1 Groove	cut	16.6 ± 0.4
10	GNKD* 40×20, 1 Groove	cut	50.4 ± 2.0

Table 4.1 – Results on light yield of plastic scintillator samples (* casted plastic scintillator)

requirements. Furthermore, this scintillator material has already demonstrated good reliability in many large-scale experiments.

4.2.4 WLS fiber comparison test and attenuation properties

Four types of WLS fibers have been tested in this work: BCF-91-A, BCF-99-29-AMC ⊘ 1.2 mm and Y11(200)-MSJ, Y11(300)-MSJ ⊘ 1.0 mm. For this set of measurements, two pieces of WLS fibers, in U-route mode, were used to collect the light produced by one pair of FNAL 45×10 mm^2 2-hole scintillator bars on the entrance window of the R9420-10 PMT. In these measurements, optical grease has been used to couple the fiber ends to the PMT entrance window.

The spectra acquired with the different fibers are presented in Figure 4.7. The number of photoelectrons measured for the different configurations are reported below:

- Signal Amp. (K.Y11(300)-MSJ) = 24.8 ± 0.4 p.e.
- Signal Amp. (K.Y11(200)-MSJ) = 21.9 ± 0.3 p.e.
- Signal Amp. (S.G.BCF-91-A) = 19.7 ± 0.4 p.e.
- Signal Amp. (S.G.BCF-99-29-AMC) = 17.1 ± 0.2 p.e.

It is interesting to observe that, despite the larger diameter of the Saint-Gobain fibers, the Kuraray ones yield more photoelectrons. If we normalize all the results to the best one

(Y11(300)-MSJ), the ratio of the fiber performances in the tested configuration can be summarized as follows:

$$Y11(300) : Y11(200) : BCF\text{-}91\text{-}A : BCF\text{-}99\text{-}29 \simeq 1.0 : 0.87 : 0.79 : 0.68$$

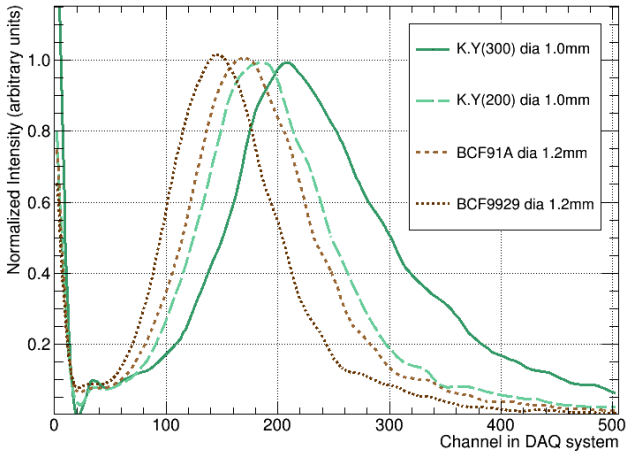

Figure 4.7 – Test results of WLS fiber comparison. The spectra are smoothed for a more clear comparison of the fiber performance.

We measured the attenuation length for the fibers BCF-91-A and Y11(200)-MSJ. In this test, we used a small piece of the scintillator FNAL ($100 \times 100 \times 10$ mm^3) with 4 holes. Four 200-cm-long pieces of the same type of WLS fiber were inserted through the holes of the scintillator, delivering the scintillation light to the PMT R9420-10. We moved the small scintillator bar along the length of the fibers. In this way, we measured the signal amplitude induced by cosmic rays as a function of the distance between the scintillator and the PMT entrance window. The results are shown in Figure 4.8. The data distribution can be fitted by the sum of two exponential terms:

$$I(x) = I_{0s}\ exp(-\frac{x}{L_s}) + I_{0l}\ exp(-\frac{x}{L_l})$$

where L_s is the short attenuation length (cm), L_l is the long attenuation length (cm), and $I_{0s} + I_{0l}$ is the light yield at $x = 0$ cm. The fit results show that $L_s \simeq 28$ cm, $L_l \simeq 276$ cm for BCF-91-A fiber and $L_s \simeq 21$ cm, $L_l \simeq 240$ cm for Y11(200)-MSJ fiber. In this test, the light reflected at the interfaces between the fiber ends and the air (at the cut ends) and between the fiber ends and the optical grease (at the ends attached to the PMT entrance window) is neglected.

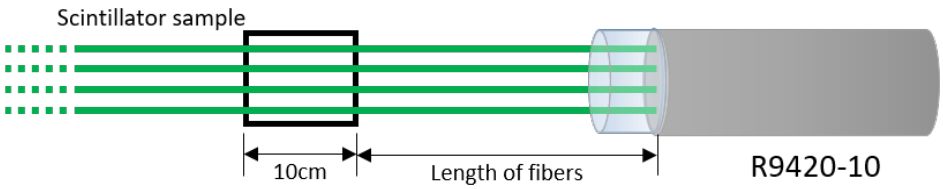

(a)

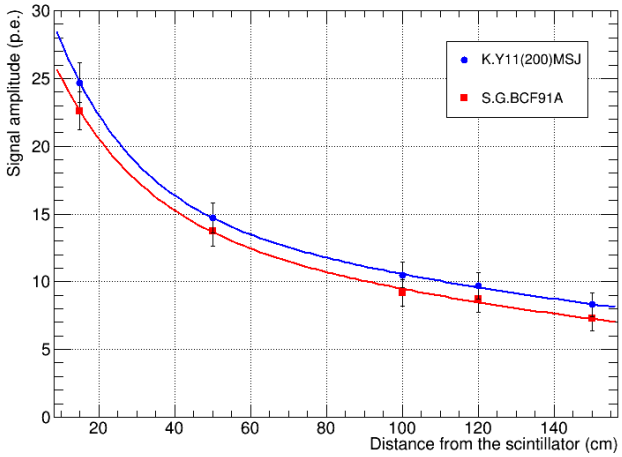

(b)

Figure 4.8 – 4.8(a) and 4.8(b) show the setup of the test and the results of light attenuation in Y11(200)-MSJ (blue) and BCF-91-A (red) WLS fibers

4.2.5 Test of temperature effect on scintillator and WLS fibers

The SSDs is planned to be deployed to operate in a harsh environment with heavy temperature variations. For this reason, the temperature effect on the plastic scintillators and WLS fibers has been investigated within a temperature range from 0 to 60 °C. One pair of FNAL 45 × 10 mm^2 scintillator bars, working with the Kuraray Y11(200)-MSJ (⊘ 1.0 *mm*) and Saint-Gobain BCF-91A (⊘ 1.2 *mm*) fibers, respectively, has been tested into a climatic chamber. The R9420-10 PMT has been placed out of the climatic chamber and used to measure the light yield of the scintillator/WLS fiber configuration. Figure 4.9 shows the setup of this test and the measured number of p.e. from both configurations as a function of temperature. The scintillator light yield has been measured in steps of 10 °C. The light yields are normalized to the p.e. number measured at 20 °C, and show a decreasing rate ∼1% per 10 °C for both scintillator/WLS fiber configurations.

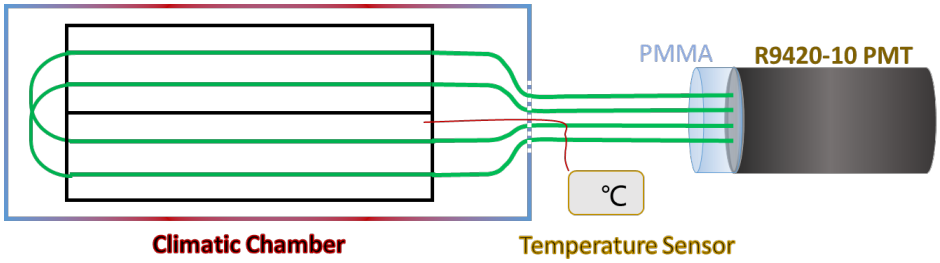

(a)

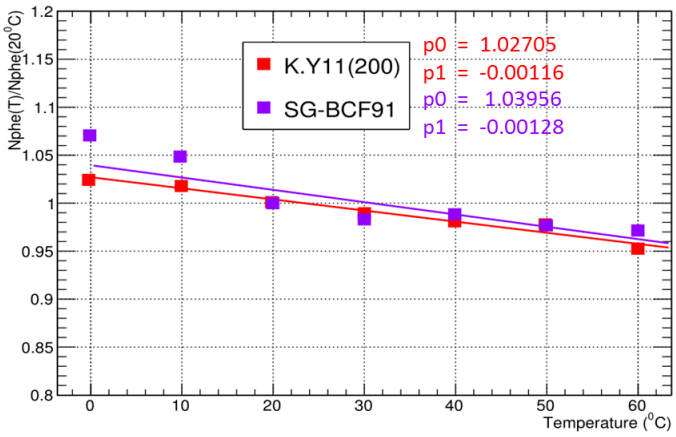

(b)

Figure 4.9 – Figure 4.9(a) shows the setup of the test of the temperature effect. Scintillator and fiber samples were put into the climatic chamber and the PMT was kept outside. A sensor was attached on the surface of scintillators to monitor the temperature. Figure 4.9(b) shows the results of temperature dependence of relative light yield of scintillator/WLS fiber configuration with Kuraray Y11(200)-MSJ and Saint-Gobain BCF-91A fibers (0 to 60°C)

4.2.6 Light-collection efficiency estimate for different scintillator/WLS-fiber configurations

In order to explain the results of this study, we estimated the number of photoelectrons yielded by different scintillator/WLS-fiber configurations. We followed the procedure proposed by M.Crow et al. in ref.[152] and by B. Loehr et al. in ref.[153].

When a cosmic muon passes through the scintillator bar it releases a defined amount of energy and, as a consequence, the scintillator produces scintillation light. This light is then collected, by means of wavelength-shifting optical fibers, to the entrance window of a PMT, which then produces an electric signal. The signal produced by a plastic scintillator with specific profile can be estimated as:

$$S_{profile} = LY_{scint} \cdot \bar{\varepsilon}_{LCE} \cdot \varepsilon_{att\_fiber}(l) \cdot \varepsilon_{PMT}$$

where LY_{scint} is the light yield of the scintillators per cm, $\bar{\varepsilon}_{LCE}$ is the mean LCE along the width of the scintillator profile, $\varepsilon_{att\_fiber}(l)$ is efficiency of the light attenuation in WLS fibers, l is the length of fiber to the PMT, ε_{PMT} is the total efficiency to convert a photon into a photoelectron and thus takes into account not only the QE of PMT photocathode but as well the LCE. For a specific scintillator material and for a given deposited energy, the light yield LY_{scint} is constant. So, since the fiber length is fixed, $S_{profile}$ is proportional to $\bar{\varepsilon}_{LCE}$. For a specific position in the profile, $\varepsilon_{LCE}(x, y)$ can be described as:

$$\varepsilon_{LCE}(x, y) = \sum_{i=1}^{n} p(i) \cdot f(i)$$

where $p(i)$ is the probability of the light collected by a single "collector" element, which consists in a fiber embedded in a hole or a groove, and $f(i)$ is a function that takes into account the possible shielding by other collectors, along the path from the position (x, y). The summation in the formula takes into account the effect of the reflective material coated on the surface of the scintillator, which artificially produces reflected "image" collectors (see Figure 4.10).

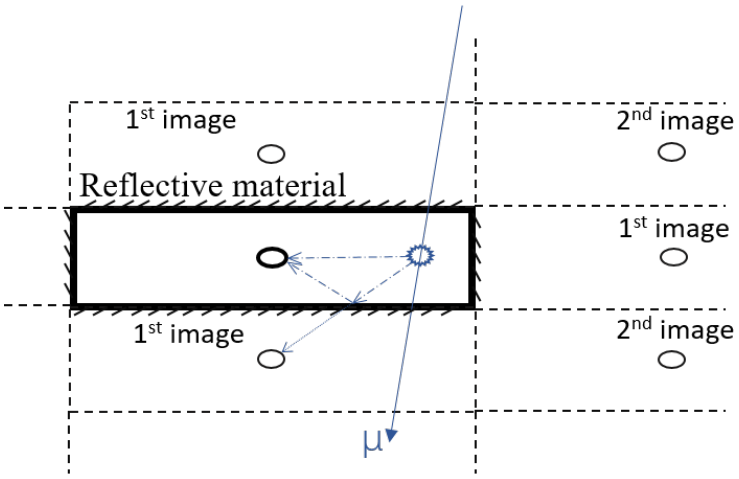

Figure 4.10 – Scheme of the estimate method with optical images reflected by the reflective material coated on the scintillator surface

In our calculation, we count the original collector and its 1^{st} and 2^{nd} reflected images in the "mirrors". The images with more than two reflections provide little contribution to the signal due to the limited solid angle and the light attenuation in the scintillator after a long distance of transportation.

$p(i)$ can be expressed as:

$$p(i) = R^m \cdot \frac{b_0}{r} \cdot [\ I_{fast}|_{r=0}\ \cdot exp(-\frac{r}{\lambda_{fast}}) + I_{slow}|_{r=0}\ \cdot exp(-\frac{r}{\lambda_{slow}})\ ],\ (r > r_0)$$

where R is the reflectivity of the coating material and m is the number of multiple reflections. For TiO_2, R is reported to be 90% at 420 nm [151], the wavelength of maximum emission of the used scintillator. The b_0/r term is taken from ref.[153]. b_0 only depends on the radius of the "collector", r_0. λ_{fast} and λ_{slow} in the attenuation term are the attenuation lengths of fast and slow components in the PS, respectively. For FNAL extruded scintillators, we set $\lambda_{fast} = 5$ cm, $\lambda_{slow} = 24$ cm and the ratio of $\frac{I_{fast}|_{r=0}}{I_{slow}|_{r=0}} = 1$ as introduced in ref.[145]. r_0 is the radius of the hole or the groove, for the tested samples it is approximately 2 mm. In the presented calculation b_0 is kept as a constant value since we assume all the collectors are ideal circle-shape with the same radius.

The estimates of relative LCE distribution over the whole profile and the projection along x-axis for different types of scintillator profile are displayed in Figure 4.11. The mean LCE $\bar{\varepsilon}_{LCE}$ of the profile can be obtained as the quotient of the integral of $\varepsilon_{LCE}(x, y)$ divided by the width of the scintillator. Therefore, the total signal can be calculated by integrating $S_{profile}$ along the length of the scintillator bar.

$$S_{scint} = \int_{l_0}^{l_0+l_{scint}} LY_{scint} \cdot \bar{\varepsilon}_{LCE} \cdot \varepsilon_{att\_fiber}(l) \cdot \varepsilon_{PMT}\, dl$$

where l_0 is the length of fibers from the scintillator to the PMT and l_{scint} is the length of scintillator bar. For U-route mode, a term of the U-route contribution can be added to the total signal:

$$S_{scint}|_U = S_{scint}|_{cut} + \int_{l_0+l_U+l_{scint}}^{l_0+l_U+2l_{scint}} LY_{scint} \cdot \bar{\varepsilon}_{LCE} \cdot \varepsilon_{att\_fiber}(l) \cdot \varepsilon_U \cdot \varepsilon_{PMT} \cdot dl$$

where ε_U is the efficiency of the U-route bending. For the bending diameter of 10 cm, ε_U is set to 95%. The ratios of different configurations can be obtained by comparing their relative S_{scint} values. Table 4.2 lists the estimated results and the corresponding experimental results. The estimate has a good agreement with the experimental data. The total difference of each profile comparison is up to 7%. This can be induced by the assumption of an ideal circular shape for the collectors. The holes of FNAL scintillators are actually in bean shapes and the grooves are in v-shapes.

4.2.7 Fiber/PMT optical coupling method tests

This study aims at proposing an effective way to couple the fiber to the PMT entrance window. To this aim, we used one pair of FNAL 45×10 mm^2 2-hole scintillators, two pieces of Kuraray Y11(200)-MSJ WLS fibers bended in U-route mode at the ends of scintillators and two different PMT, the R9420-10 from Hamamatsu and XP5300 from Photonis. The scintillator

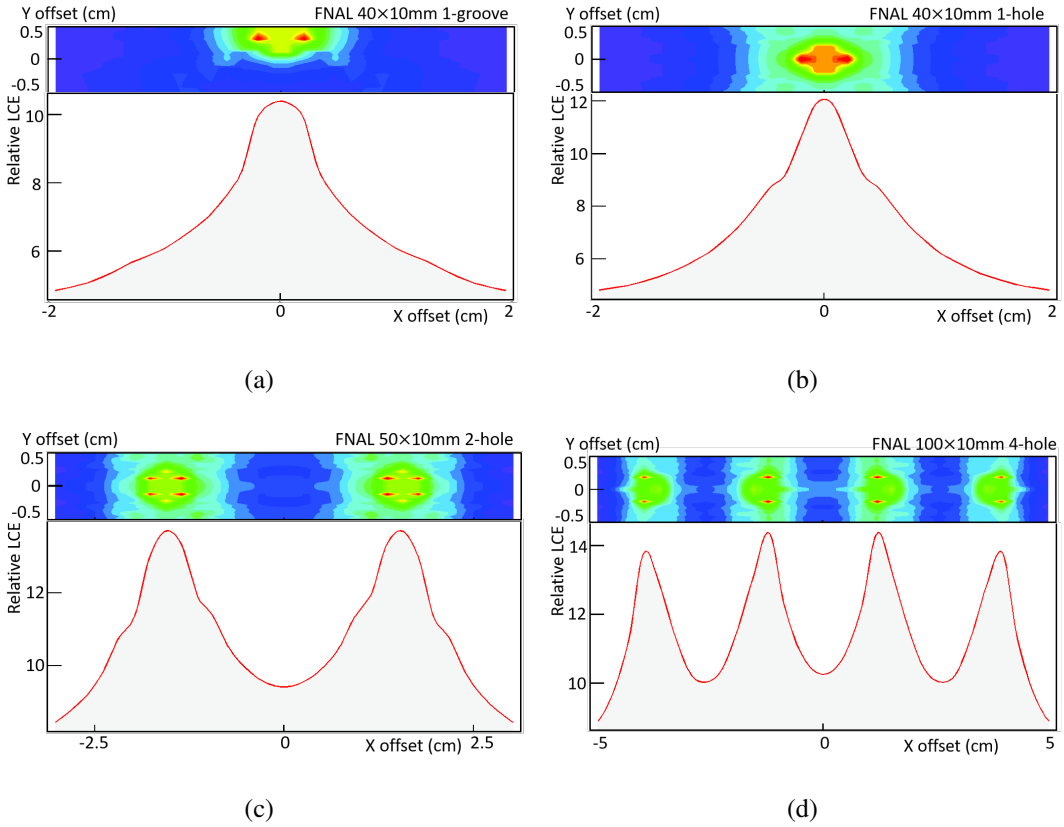

Figure 4.11 – The distribution of relative LCE over the whole profile and LCE projection along x-axis for different plastic scintillator bars.

No.	Profile comparison	ratio	
		experiment	estimate
1	50mm-wide PS, Thickness 2cm/1cm	1.59	1.64
2	50mm×10mm 2-hole PS, U-route/cut	1.64	1.71
3	PS: 50mm 2-hole/40mm 1-hole	1.48	1.53
4	100mm 4-hole/50mm 2-hole	1.00	1.06
5	1-groove/1-hole	1.04	1.01

Table 4.2 – A comparison between experimental and estimated signal ratios at PMT by different scintillator/WLS-fiber configurations.

detector was then coupled to the PMT entrance window using five different optical coupling configurations:

I. No couplant or wrapping material

II. Optical grease

III. RTV silicone pad

IV. Optical grease + Teflon tape wrapping

V. Optical grease + VM2000 wrapping

The optical grease used is Dow Corning Q2-3067 and the RTV silicone is Rhodorsil RTV 141. The results of this test have been summarized in Figure 4.12.

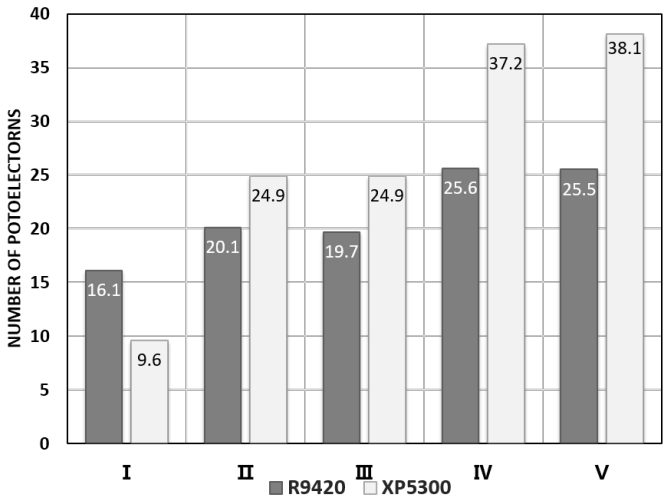

Figure 4.12 – Measured number of photoelectrons for different coupling configurations (see text).

It is interesting to observe that the actual light yield improvement depends on the structure of the particular PMT. For R9420-10, which is particularly designed to optimize the focalization of photoelectrons onto the first dynode, the use of couplant materials can increase the signal amplitude by 25% (from 16 p.e. to 20 p.e.), while the wrapping materials can provide another increase of ~ 25% (up to 25 p.e.). For the PMT XP5300, which is not optimized for the photoelectron collection at the first dynode, a muon peak signal amplitude of 9.6 p.e. is obtained without any couplant and wrapping material. With the help of couplants and wrapping materials, the signal amplitude is increased considerably, up to ~ 38 p.e..

4.2.8 Summary

We have performed several studies on each component in the scintillator/WLS-fiber configuration and discussed the effects of scintillator cross-section properties, WLS fiber type, and optical coupling method on the final signal amplitude. A numerical estimate of LCE is also presented to explain the experimental data of scintillator tests. These results offer

a quantitative comparison between the candidate scintillator/WLS-fiber configurations of SSD. Furthermore, the results can also be used for other general designs of scintillator-based detectors with WLS fiber read-out.

Considering the actual condition on site and the total cost of SSD, the Auger Collaboration has chosen the configuration of (FNAL 50 $\times$ 10 mm^2 2-hole scintillator + Kuraray Y11(300)-MSJ ($\oslash$ 1.0 mm) WLS fiber + RTV silicone pad) for the SSDs in AugerPrime.

4.3 Assembly of optical coupling module for SSD

In the SSD detector of AugerPrime, the light generated in scintillator bars is transported along the 48 pieces of fibers to the entrance window of the PMT. For each piece of fiber, there is a U-routing at the ends of scintillator bars. Thus, for an entire detector, 96 fiber ends are coupled to the PMT entrance window. As the fiber/PMT coupling is a crucial interface for optimal light collection efficiency, the fabrication method of this module plays a key role in the performance of the entire detector.

Two different approaches are used to fabricate fiber/PMT optical coupling module of SSDs. One is the so-called "melting method", which is developed by the KIT group. With this method, the fiber ends are first melt and then bundled in the coupling module. The details of this method are introduced in ref.[154]. The other approach is the so-called "polishing method" proposed by the IPN-Orsay group (see Figure 4.13). In the following, only the method developed and tested as a part of this thesis work will be presented in details.

4.3.1 Polished fiber/PMT optical coupling module for SSD

In this design, the fiber ends are bundled and glued inside a PMMA cylinder, then polished with an electric polisher or by hand. The module is finally coupled to the PMT entrance window with an RTV silicone pad as couplant.

This design of optical coupling module has many advantages. First of all, it can offer a high light collection efficiency for SSDs, since the fiber ends are polished to be clear and tightly attached to the surface of the RTV silicon pad. Secondly, it has a simple structure with only two optical interfaces between the fiber ends, the couplant and the PMT entrance window. This minimizes the light loss at the coupling part of the detector. Thirdly, the cement is only used to fix the fibers in place, not used as an optical element, which avoids the potential risk due to the aging of the cement in a long-term operation. Finally, the procedures of its fabrication are simple and can be easily realized in a large-scale production.

In April 2016, one SSD detector of the AugerPrime Engineering Array (EA) was assembled

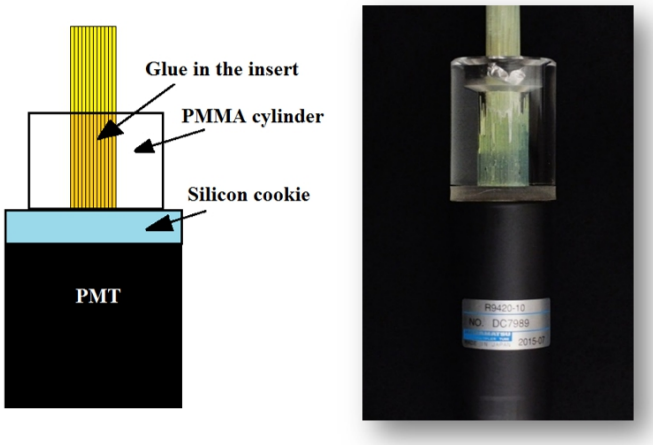

Figure 4.13 – The design of the polished optical coupling module

and fabricated with a polished fiber/PMT optical coupling by the IPN-Orsay group. In the following subsections, we present the fabrication procedures of this polished coupling module (subsection 4.3.2) and the preliminary test results of this detector obtained by using the muon tower at KIT (subsection 4.3.3).

4.3.2 The fabrication of the coupling module

The SSD detector is designed to be fixed in an enclosure box. We first assembled the entire detector including the scintillator bars, the optical fibers and the fiber routers, in the enclosure frame. The fiber ends are bundled and aligned to be at the same level with a tolerance range of up to 5 mm. Then, the fiber bundle is glued with a PMMA cylinder in a Teflon container by using the Saint-Gobain BC600 optical cement. The dimension of the PMMA cylinder follows the SSD coupling module design presented in ref.[154]. Finally, the whole coupling module together with the fiber bundle was kept still for a cure time of 12 h. In this design, the glue is not used as optical element but only to provide more rigidity and stability to the bundle and to fill the empty spaces between the fibers. Therefore, the cure time can be shorter than that suggested in the datasheet (48 h).

When the glue is completely cured, we separate the coupling module out of the Teflon container. As mentioned in the previous paragraph, a 5mm-long excess of fibers outside the PMMA support was reserved and thus ensures that all the fiber ends can be adequately polished in this step. We first polished this protruding part by hand with 200-grit and 320-grit sandpapers until the excess is removed and the surface is even. Then, we employ an electric polisher with a 1-inch loose cotton wheel installed on it to finish the last buffing procedure. As the loose cotton is quite soft, it will collapse and not damage the surface when touching the

surface of fiber ends. When doing the buffing, we keep the spindle speed of the polisher below 10000 revolutions per minute as a proper speed both protecting the surface from splitting off and ensuring it is buffed well. After the buffing with the loose cotton, the surface of each fiber ends gets clear and the emitted lights of the fibers are uniformly distributed throughout the whole bundle surface.

After the fabrication of the optical module, the whole module was fixed on top of the PMT aluminum housing. A silicone pad is attached to the fiber bundle as optical couplant between the fiber ends and the PMT entrance window The silicone pad is made of Room Temperature Vulcanization (RTV) silicone materials. In our design, the RTV silicone type we used is RHODORSIL RTV 141 A&B. The silicon pad is fabricated by mixing two reagents (A and B) with a ratio of 100:5. Similar RTV silicones are also produced by some other companies like Wacker and GE silicone. The GE6136 RTV silicone has been applied in the Auger Surface Detector as optical couplant for more than 10 years. Thus, the RTV silicone pad is expected to have a good performance against the aging when working in the field for a long time.

Figure 4.14 shows the pictures of this optical coupling module assembled in the detector. Detailed statements and pictures of the fabrication procedure are presented in Appendix A.

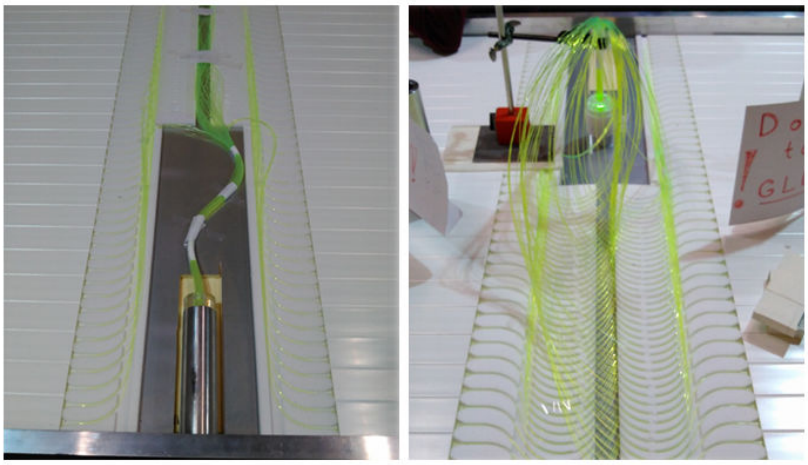

Figure 4.14 – Fabrication of the optical coupling module of SSD.

4.3.3 Tests of the SSD module

The detector is closed with a cover-board and tested in the muon tower hosted in the in the mechanics workshop of KIT. The muon tower consists of three position sensitive muon detectors from the KASCADE experiment. The SSD detector is placed inside the muon tower and tested with cosmic rays under a quadruple coincidence trigger condition (see Figure 4.15). The PMT employed in the tests is Hamamatsu R9420 provided by the INFN-Lecce group and

supplied with a high voltage of 1500 V in the measurement.

The results of the detection efficiency distribution and the signal histogram of the SSD detector are shown in Figure 4.16 and Figure 4.17, respectively. In the left plot of Figure 4.16, we can see a good agreement between the efficiency distribution and the scintillator and fiber layout, which means that all the scintillator bars are working well and none of the fibers is broken. In the right plot of Figure 4.16, the efficiency distributions along the X and Y axes are uniform over the scintillator area. The scintillation light is transported along the fiber length towards the PMT entrance window and it is collected at the photocathode by means of the coupling module. Before reaching the PMT, each piece of fiber is bended several times according to the detector layout. This effect, together with the individual optical matching of each fiber end in the coupling module can induce a variation in the final light yield of the entire detector. The results of our tests show that all 96 fibers have comparable conditions in terms of both scintillation light transportation and the optical matching to the PMT. In the plot of the efficiency distribution along Y-axis (Figure 4.16, right), we can identify the three little peaks between the two plateaus corresponding to the fiber routes in the detector. In Figure 4.17, the charge distribution shows a peak at about 6.5 pC. Taking into account the PMT gain, it corresponds to 32.6 p.e./MIP. The Peak-to-Valley ratio (P/V) is used to describe the significance of the MIP peak. In this spectrum, the peak and the valley refer to the counts of the MIP peak and the lowest point between the two peaks, respectively. The P/V shown in the histogram is larger than 40.

This SSD detector, equipped with a fiber/PMT coupling module fabricated with the polishing method, has been shipped to the Pierre Auger Observatory in September 2016 and deployed in the Auger Prime Engineering Array in the station Didi (i.d. 136). In March 2016, this SSD detector was moved to the station Peteroa (i.d. 62) in the EA area to be studied for its performances together with other SSD detectors. The data of the EA has been analyzed and is presented in chapter 5.

4.4 Summary

Within the framework of AugerPrime, we have performed a series of R&D work for optimizing the SSD configuration in terms of scintillator types, WLS fiber types, and the fiber/PMT optical module. Plastic scintillator samples with different geometries from two providers, FNAL and GNKD, are tested and compared. Main effects on the measured results are summarized in subsection 4.2.3. The performance of four types of WLS fibers, Y11(300) ⊘1.0 mm and Y11(200) ⊘1.0 mm from Kuraray, BCF-91-A ⊘1.2 mm and BCF-99-29-AMC ⊘1.2 mm from Saint-Gobain, equipped with the SSD candidate scintillators in terms of measured signal

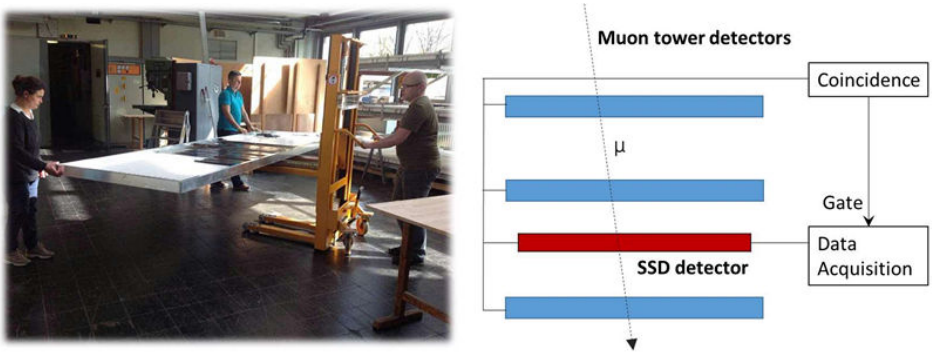

Figure 4.15 – The detector frame is closed with a cover-board and tested in the muon tower with cosmic rays.

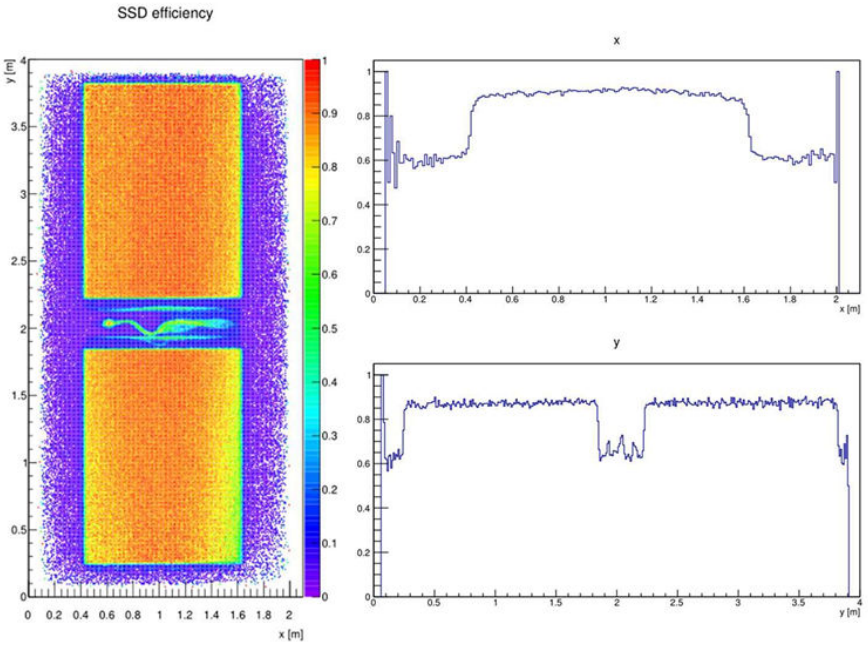

Figure 4.16 – The detection efficiency distribution of the SSD detector shows a good agreement with the scintillator and fiber layout (left). The efficiency distributions along X and Y axes are uniformed for the scintillator area. In the plot of the efficiency distribution along the Y-axis, we can see three peaks between the two plateaus corresponding to the fiber routes.

amplitude and light attenuation are presented in subsection 4.2.4. The configuration of (FNAL 50×10 mm^2 2-hole scintillator + Kuraray Y11(300)-MSJ ($\oslash$ 1.0 mm) WLS fiber + RTV silicone pad) was chosen by the collaboration for the SSD detectors. When supplied by a HV of 1100 V, the output signal of this detector configuration is > 30 ph.e. which is much larger than that required in the SSD specifications (> 12 ph.e.). The candidate fiber/PMT coupling methods are tested and the measured results presented in subsection 4.2.7. We assembled an

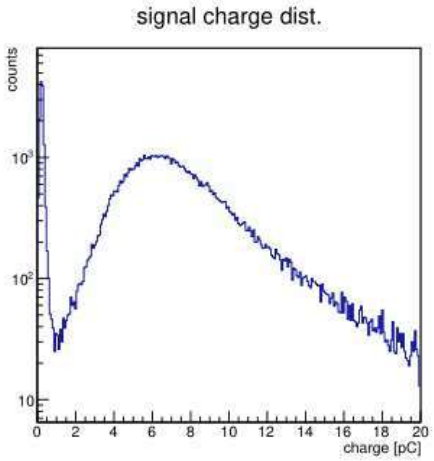

Figure 4.17 – The charge distribution shows a peak at about 6.5 pC, corresponding to 32.6 p.e./MIP. The Peak-to-Valley ratio is larger than 40 which means that there is a good separation between the signal and the pedestal.

SSD detector and fabricated the fiber/PMT coupling module with polished fiber ends for this detector. Currently, it works in Station i.d.25 of the EA.

The results of this work have been presented in the Auger collaboration meetings and discussed with the collaborators in the SSD group. Three technical reports and a manuscript of journal paper for NIM-A were written by the author of this thesis. The technical reports are stored in the website of Auger collaboration. The manuscript of journal paper is currently under review by the collaboration:

- GAP2015_085 *Fiber and coupling method selection for SSD*
- GAP2016_034 *Scintillator tests for SSD*
- GAP2016_037 *Polished fiberPMT coupling procedures for SSD*
- *Study of light yield for different configurations of plastic scintillators and WLS fibers*

5

Analysis of first data from AugerPrime engineering array

The AugerPrime implementations for the existing SD array are introduced in section 3.3. In October 2016, the AugerPrime engineering array was installed within the existing array of the Observatory. In this chapter, we will discuss the first results from the AugerPrime engineering array. In particular, we will present the detector calibration in units of vertical equivalent muon (VEM) for WCD and minimum ionizing particle (MIP) for SSD. Furthermore, we will discuss the temperature dependence of the detector parameters, show the lateral distribution function of the showers measured with both detector types, and present the preliminary results of the study on signals from doublet stations.

5.1 Deployment of the AugerPrime engineering array

5.1.1 Layout of the Engineering Array

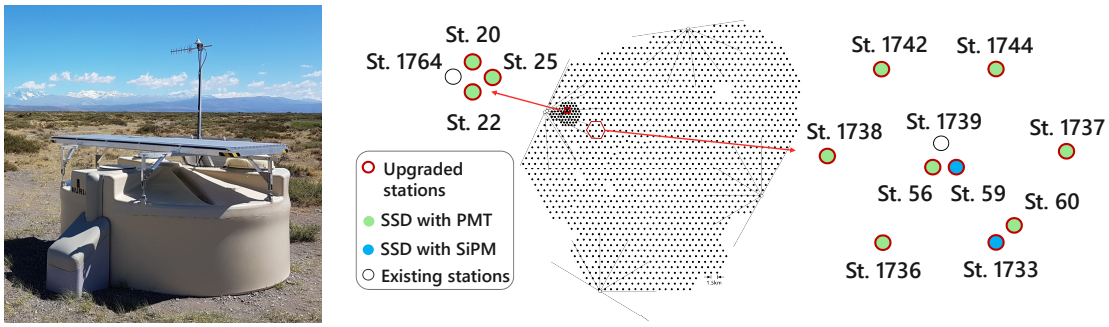

Figure 5.1 – *Left:* Photograph of an AugerPrime surface detector (St. 56) in operation. *Right:* Layout of the AugerPrime engineering array. Several groups of multiple stations are deployed in the EA: stations (1739, 56, 59), (1733, 60), and (1764, 20, 22, 25).

The AugerPrime engineering array (EA) of 12 upgraded detectors, equipped with SSDs, UUBs and added small PMT (SPMT), was deployed in October 2016 and has since then continuously been taking data. Figure 5.1 shows a photo of an AugerPrime detector and the

layout of the AugerPrime EA. In the EA, 9 upgraded stations are located in a hexagon shape surrounding the existing SD station 1739 in the regular SD array (1500 m spacing) and three upgraded stations are deployed in the so-called AERAlet area near the station 1764 (433 m spacing). Some stations are deployed close to each other (with 11 m spacing) as doublet or multiple stations for signal accuracy and other studies (see Figure 5.1).

5.1.2 EA Data in CDAS

The development of the UUB firmware/software as well as the CDAS software are still in progress. Therefore, the analysis can not be performed by using the standard Auger data analysis program. The author of this thesis developed for this purpose a user code of CDAS for the data analysis.

The EA stations are equipped with the upgraded electronics having 10 FADC channels (CH.). They are capable of processing the data from both WCD and SSD detectors, which have in total 5 PMTs in operation. Table 5.1 shows the arrangement of signals in UUB channels. The high-gain (HG) and low-gain (LG) signals of the three large PMTs (LPMT) are processed and recorded in CH.1 to CH.6, respectively. The signal from the SPMT, which is added to extend the dynamic range of the WCD, is delivered by the channel CH.7. The SSD HG and LG signals are in the channel CH.9 and channel CH.10. Currently, CH.8 is a spare channel for further development.

No. of Channel	Signal from	No. of Channel	Signal from
1	WCD PMT 1 LG	6	WCD PMT 3 HG
2	WCD PMT 1 HG	7	WCD small PMT
3	WCD PMT 2 LG	8	spare
4	WCD PMT 2 HG	9	SSD PMT LG
5	WCD PMT 3 LG	10	SSD PMT HG

Table 5.1 – Signal in each channel of the UUB.

The upgraded stations (WCD and SSD) can be operated with various trigger modes [119] (see also subsection 3.1.2). The current trigger for the AugerPrime EA stations (10/2016 to 06/2017) is a WCD-trigger mode (down-scaled 40 MHz T1 threshold trigger), which means that the signals of WCD and SSD are both triggered by the WCD. The SDEU group is currently implementing new trigger modes. In particular, a new mode of the SSD MIP signal triggered in coincidence with the WCD VEM signal for the detector calibration is being developed. The new trigger mode will be helpful for us to better understand the performance of SSD detectors. Figure 5.2 shows the FADC traces for an event delivered to the CDAS system.

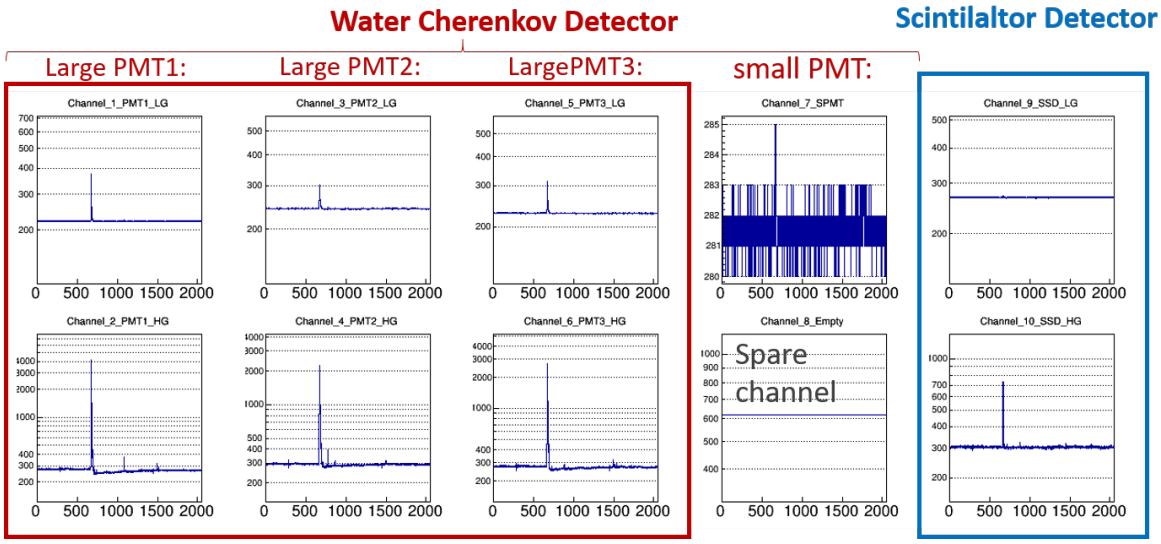

Figure 5.2 – The FADC traces delivered to CDAS.

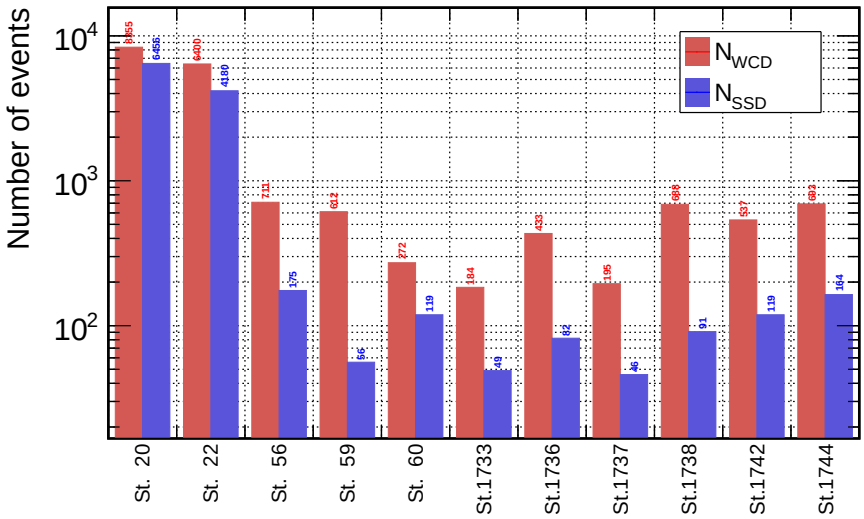

Figure 5.3 – Number of events from WCDs and SSDs.

During the operation of the EA from October 2016 to May 2017, more than 8000 shower events were recorded. Figure 5.3 shows the number of WCD and SSD events in each station. We can see that the St.20 and St.22, which are in the AERAlet area (433 m spacing), have much higher trigger rate than the others deployed in the regular SD array area and are mostly triggering on small showers. As we have been maintaining and optimizing the detectors in the last few months, some of the stations were not working with a full duty cycle. The number of events recorded by EA stations have slight differences but are comparable with the event numbers from stations nearby. As the active SSD area is much less than the WCD area (about two-fifths), the trigger rate of the shower events for SSDs is relatively lower than that for

WCDs. The area of detectors also affects the signal amplitudes of each shower event. For most events, the signal ratio of S_{SSD}/S_{WCD} is less than 1 (average ratio around 0.65). However, for a given shower, the correlation of S_{SSD} and S_{WCD} depends on the distance from the station to the shower axis. The related results are shown in subsection 5.4.3.

5.2 Calibration and dynamic range of the EA stations

5.2.1 Calibration of WCDs and SSDs

In the WCD calibration, the main parameter is the average charge deposited by an incident vertical, central muon passing through the WCD [155]. This parameter can be obtained from the charge spectrum of background muons measured by each PMT in the WCD (see Figure 5.4-left). In the muon charge spectrum, the second peak is induced by the muons crossing the WCD from all directions. By fitting the peak position, the approximate charge value of a vertical equivalent muon (VEM) can be determined. Based on simulations and measurements with test-detectors, the final VEM charge used in the detector calibration is determined with $Q_{VEM} = Q^{raw}_{VEM}/1.01$, where 1.01 is the factor of the conversion from omni-directional to vertical muons.

For the SSDs, the charge deposited with a minimum ionizing particle (MIP) is used for the calibration (see Figure 5.4-right). The *raw MIP charge* is obtained by fitting the second peak position in the charge spectrum from SSD and the final MIP charge is determined with $Q_{MIP} = 0.87\, Q^{raw}_{MIP}$, where 0.87 is determined based on related measurements and simulations [128, 156].

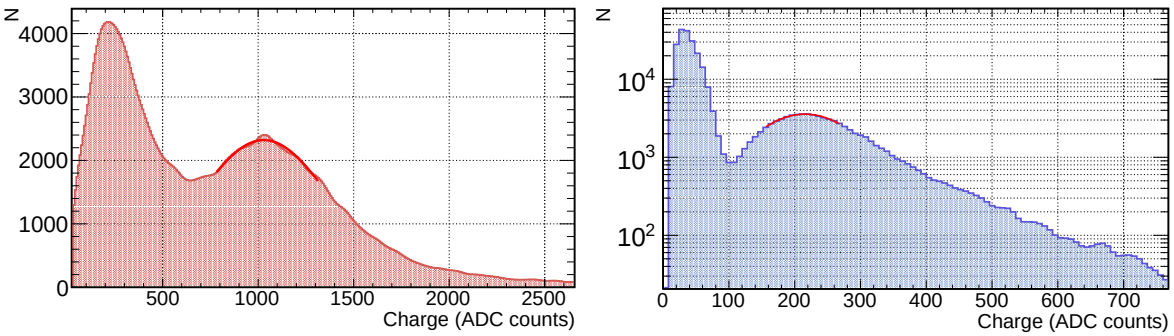

Figure 5.4 – *Left:* The VEM charge spectrum measured by one of the WCD PMTs. The second peak corresponds to the charge deposited by single muons traversing the detector station. *Right:* The MIP charge spectrum from the SSD PMT.

The VEM or MIP charge spectra from WCDs and SSDs are stored in the muon buffer of each local station and sent to the central data acquisition system (CDAS) every 6 minutes.

Therefore, the evolution of the calibration information can be monitored to study the long-term performance of the detectors.

The VEM charge measured by a large PMT in St.20 as a function of time over a period of 10 days in May 2017 is shown in Figure 5.5-left. The data are binned over 2 hours and the mean VEM charge values of each bin are plotted as a function of time with the RMS of the data in the bin as the error bars. The measured VEM signal can be affected by temperature effect on the complex detector system (eg. PMT, water, and electronics). In order to investigate this temperature effect on the VEM charge, the correlation between the VEM charges and the real-time temperature values over the whole month of May 2017 are shown in Figure 5.5-right. It is noted that the monitoring data from WCD and SSD is not yet available in CDAS. Therefore, the temperature measured by the central laser facility (CLF) deployed in the SD array area is used in this analysis. It can be seen that they have a negative correlation and the fitted slope is -26.5 ADC counts / 10°C, which corresponds to ~1.4% / 10°C.

Similarly to the VEM charge, the MIP charge measured by the SSD is also affected by the outside temperature since the scintillation materials and the PMT photocathodes have a certain sensitivity to the temperature. Figure 5.6-left and Figure 5.6-right show the MIP charge measured by the SSD in St. 20 as a function of time and temperature, respectively. A slope of ~6 ADC counts / 10°C (~2.5% / 10°C) for the negative correlation between the MIP charge and the temperature can be obtained by fitting the data presented in Figure 5.6-right.

These results give a general description of the correlation between the VEM or MIP charge and the temperature. The slope of their correlation also depends on the situation of each individual PMT and other parameters. Since for both detectors, the calibration is performed nearly continuously based on the real-time muon spectra, the temperature dependence does not affect the data of shower events in the measurement of cosmic rays.

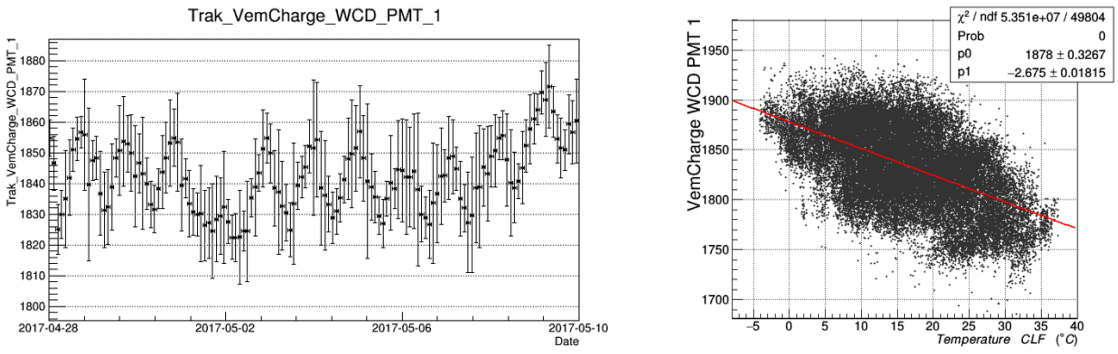

Figure 5.5 – *Left:* Measured VEM charge of the WCD PMT 1 in St.20 over the period of 28/04/2017 to 10/05/2017. *Right:* The correlation between the VEM charge of St.20 and the CLF temperature over the month of May 2017.

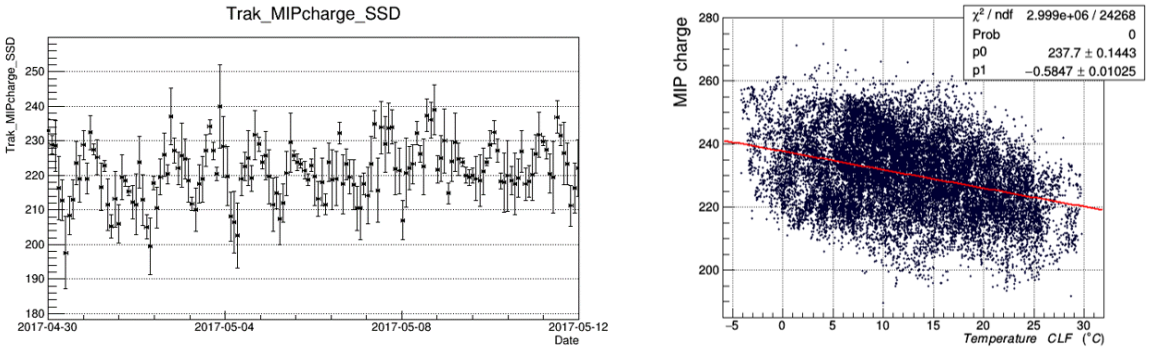

Figure 5.6 – *Left:* Measured MIP charge in Station i.d.20 over the period of 30/04/2017 to 12/05/2017. *Right:* The correlation between MIP charge of the SSD in St.20 and the CLF temperature over the month of May 2017.

5.2.2 Dynamic range of the detectors

In the measurement of UHECRs, the existing SD array is limited by a saturation of the FADC channels and the large PMTs for the shower signals close to the shower axis. An extra small PMT was added to the upgraded WCDs to extend the dynamic range and to improve the uncertainty for very large shower signals. The SSD PMTs were selected among several candidates to have a large dynamic range and a good linearity. The HV of SSD PMTs used in the EA is ~850V for the study presented here. Benefiting from the technical implementation of the SPMT, the SSD PMT, and the upgraded electronics, the AugerPrime stations are capable of measuring the signals 32 tiles larger than those measured by the existing stations.

Figure 5.7-left shows the correlation between the signals measured by the SSDs in MIPs (S_{SSD}) and by the WCDs in VEMs (S_{WCD}) recorded during four months of EA operation. The LPMT signals and the SPMT signals are colored in black and red, respectively. In the Figure 5.7-left, it can be clearly seen that the dynamic range of the EA stations is extended to particle densities as high as few tens of thousands VEMs or MIPs. The extension of the WCD dynamic range by the SPMT from around one thousand to more than thirty thousand VEMs can be clearly seen in Figure 5.7-left. Figure 5.7-right shows the S_{WCD} measured in a single station by the LPMTs (blue) and by the SPMT (red and cyan). The blue, red histograms referring to the LPMT and SPMT signals continue up to the saturation following the power law behavior as expected. The cyan histogram stands for the saturated signals in the SPMT. The overlap of the LPMT and SPMT signals from hundreds to one thousand VEMs are used to calibrate and crosscheck the SPMT signals. The EA stations can measure the shower signals of cosmic rays at the ground down to a core distance of ~250 m [119].

As a new detector type installed in the SD stations, the dynamic range of the SSDs has also been assessed during the EA operation. Since SSDs have a rapid response to the secondary

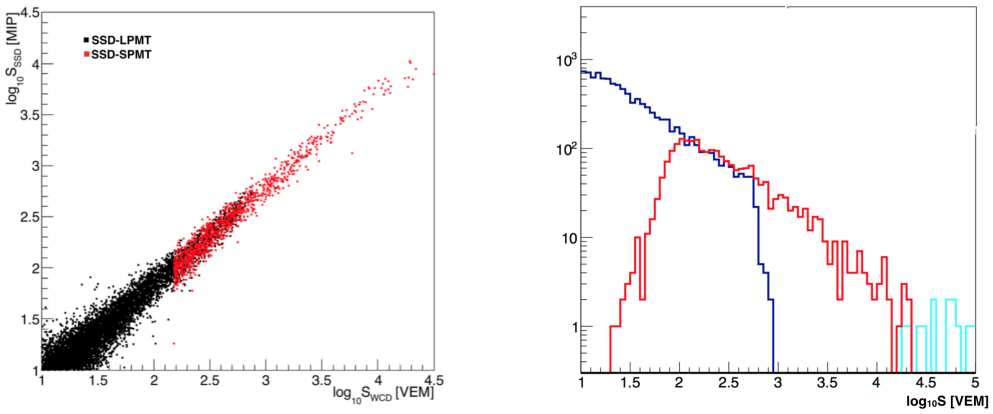

Figure 5.7 – *Left:* Relation between the WCD and the SSD signals measured by the EA stations. *Right:* The WCD signals measured by the LPMTs (red), the SPMT (blue, cyan for the SPMT saturation) in a certain EA station. These figures are taken from ref.[157].

particles of air showers, their signals are narrower and sharper than the corresponding WCD signals. The SSD signal is split into the HG (×32) and LG ($\times\frac{1}{4}$) channels. Each FADC channel of 12 bits will get saturated when the signal height is above 4096 ADC counts. The dynamic range of the SSD is up to the saturation of the LG channel. The linearity over the whole range (from baseline to 4096 ADC counts) of the HG and LG channels is also crucial for the EAS detection. In order to investigate the linearity and the dynamic range of SSD, the signal height ($SigPeak$) and the S_{SSD} in MIPs measured in each shower event are taken for the analysis. Figure 5.8 shows the relation between the S_{SSD} and the signal peak of the SSD HG and LG channels, respectively. As it can be seen in Figure 5.8-left, the SSD has a good linearity for measured shower signals from a few to around 100 MIPs in the HG channel up to the HG saturation and from ~100 to few tens of MIPs in the LG channel up to the LG saturation.

The dynamic range of SSDs is also obtained with another approach based on the hardware test on site by the SSD group [158]. Most of SSD detectors have a dynamic range up to ~ 10000 MIP. These results are in good agreement with the dynamic range obtained with the data of shower events.

5.3 Performance of the EA

Monitoring the detector performance is important for the EA operation. Based on the monitoring data, we can evaluate the stability of the detector components and gather experiences for further operation of the detector stations.

With the data from EA stations in CDAS, the important quantities indicating the real-time detector performances can be obtained. The relevant monitoring parameters are listed as

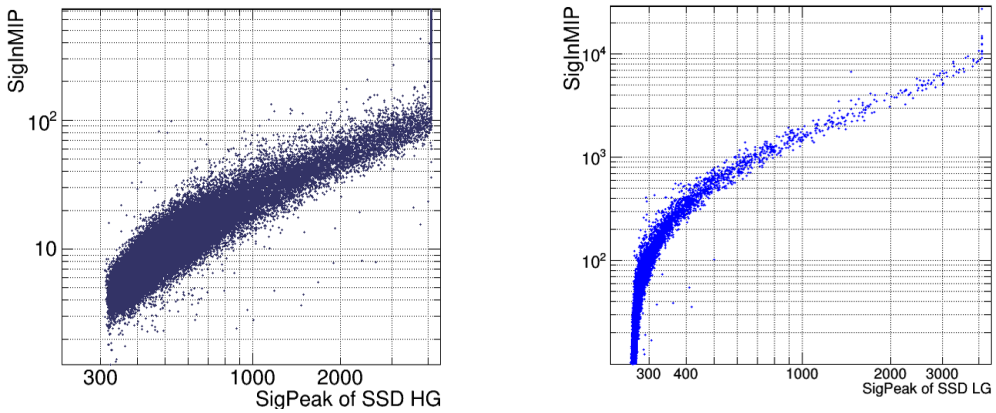

Figure 5.8 – Correlation between S_{SSD} and the signal peak in HG (left) and LG (right) FADC channels of the SSDs.

follows:

Electronic parameters:

- **Baseline**: The baseline refers to the pedestal of the trace in each FADC channel of the UUB board. Baselines are important to monitor the stability of the electronics.
- **Noise Level**: The RMS of the baseline is used to indicate the noise level in the UUB channels. The noise level can be affected by various hardware factors, e.g. the performance of the PMT base, the layout of the electronic circuits, the quality of each electronics components, etc..
- **HG/LG ratio**: The ratio of the HG signal height and the LG one for the VEM or MIP signals. In the design of the UUBs, which is introduced in subsection 3.3.2, the HG/LG ratio is ~32 for the WCD PMTs and ~128 for SSD PMTs. Since the HG channels are used for the absolute calibration with VEM and MIP, the measurement of the HG/LG ratio and its fluctuations is crucial to improve the accuracy of the overall calibration.

Detector parameters:

- **VEM Charge**: The VEM charge is fitted from the real-time muon spectrum measured by the PMTs and it's a quantity used to monitor the calibration of the WCDs.
- **Area-over-peak (AoP)**: The ratio of the amplitude and the peak of the VEM signals measured by WCDs. As the AoP has a direct relationship with the decay time of the muon signals, it is introduced to describe the WCD performance and is available from the detector in real-time. The unit of AoP is the width of the time bin ($T_{bin} = 8.33\,ns$) or called "FADC sampling slots".

- **MIP charge**: Similarly to the VEM charge, the MIP charge is used to monitor the SSD calibration.
- **SSD signal width**: The FWHM value of the MIP signals measured by the SSDs. This parameter can be obtained from the average MIP signal in the SSD and is used to describe the stability of the SSD detector system.

The operation status of each EA station has been investigated based on these quantities. In this section, the significant features of these detector parameters referring to the EA operation status are reported.

5.3.1 Baseline and noise level

The baseline of each FADC channel is evaluated according to the trace from the 50th to the 550th bin, where the main signal of the shower event has not arrived yet (see Figure 5.9). The baseline and the noise level are described by the median value of the signal and the RMS of baseline offset over this range, respectively.

The baseline fluctuates about ±3 ADC counts during day and night with the environmental temperature going up and down, due to the temperature effect on the PMTs and electronic components. The survey of the noise level for 10 EA stations is shown in Figure 5.10. We can see that the average noise levels are below 1.0 ADC counts for the SPMT channels and the LG channels of WCD LPMTs and SSD PMTs, while for the HG channels, they are below 3.0 ADC counts. During the operation of the EA, the baselines and the noise levels remain stable, which verifies the reliability of the UUBs. The noise level for the HG channels is not perfect but acceptable for the 12-bit FADC, which supports for a maximum pulse of 4096 ADC counts in each channel. Currently, new UUB prototypes are being fabricated. Special care has been taken to reduce noise in this new design (better layout and front-end protection).

5.3.2 HG/LG ratio

The HG/LG ratios calculated with the shower events of a certain station in the EA are shown in Figure 5.11. The data for this analysis is selected with the signal height in the HG channel above 1000 to reduce the effect of electronic noise. For the WCD PMTs, the measured HG/LG ratio is around 32 with a fluctuation of ~2% (see Figure 5.11(a)). The measured HG/LG ratio for the SSD PMT shown in Figure 5.11(b), is around 120 with a fluctuation of ~5%. For all the EA stations, the HG/LG ratios are comparable to the ones of this station. As these results are acquired from the signals of shower events saved in CDAS, which have different properties compared to the muon signals, further confirmation is needed with the slow control

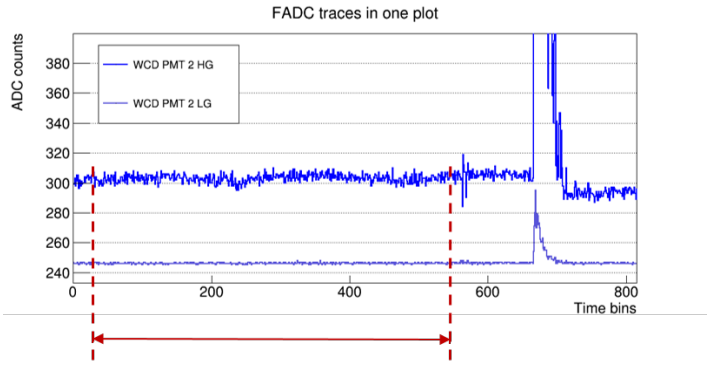

Figure 5.9 – The range (50th to 550th bin) of the FADC trace used to evaluate the baseline and the noise level of the channel.

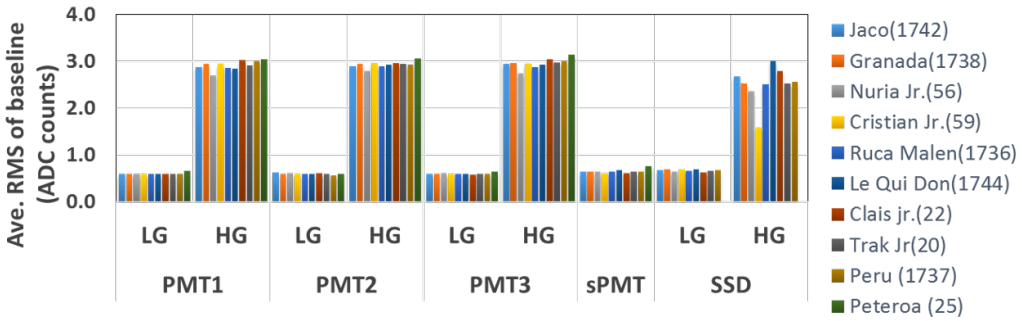

Figure 5.10 – The average noise level for the EA stations: < 1.0 ADC count for LG channels and < 3.0 ADC counts for HG channels.

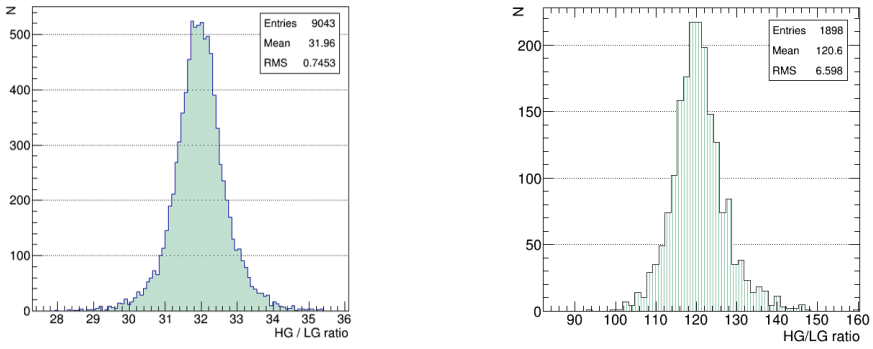

(a) (b)

Figure 5.11 – HG/LG ratios of the WCD PMTs (5.11(a)) and the SSD PMT (5.11(b)) calculated with the signals of shower events.

data, which is going to be implemented to the monitoring system. It is noted that for the new UUB prototypes the tolerance of the front-end components was reduced (1% to 0.1%) and therefore a better accuracy is expected for the HG/LG value.

5.3.3 Area-over-peak of the WCDs

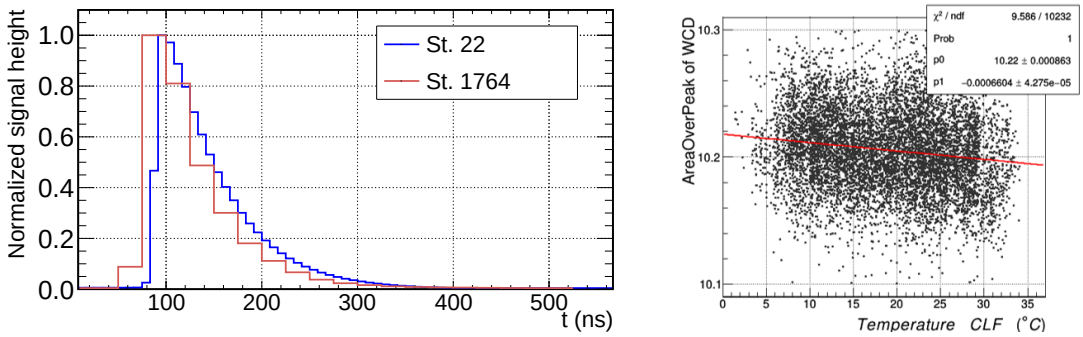

Figure 5.12 – *Left:* Comparison of muon signal shapes from the existing station 1764 and the upgraded station 22. The signals are normalized by their signal heights. *Right:* The correlation of the AoP and the temperature taken from one of the EA stations.

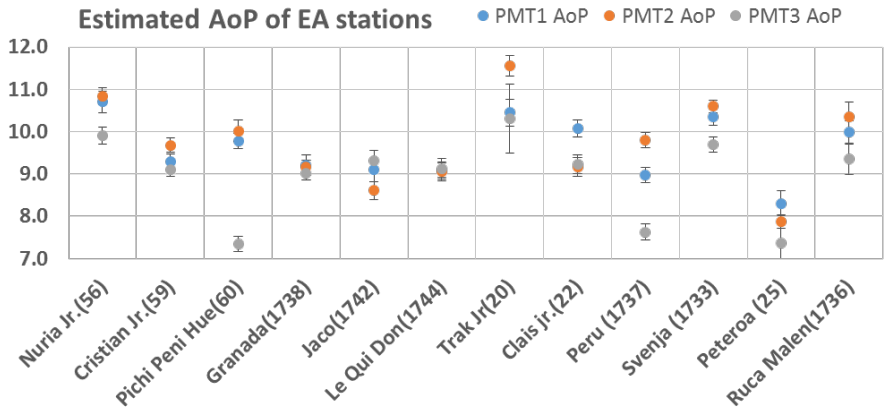

Figure 5.13 – The average AoP values and their fluctuation levels of all WCD PMTs in the EA stations.

The average signal shapes of background muons from the WCDs are also recorded and sent to CDAS (see Figure. 5.12-left). Various quantities to evaluate the detector performance can be parameterized from the digitized average signal shapes. The PMTs have a fast response to a single muon, dominated by the Cherenkov light reflected only once at the tank liner. After reaching the peak, the signal exponentially decays due to the absorption both in the water and at the reflections on the liner. Therefore, the decay time of the muon signals in WCDs are related to the reflectivity of the liner and to the transparency of the water in each WCD.

Among the 1660 SD stations, the average value of the muon decay time is around 60 ns (distributed between 50 to 70 ns). The area-over-peak (AoP) ratio of the muon signal, proportional to the signal width, is relevant to describe the detector performance and is

available from the detector in real-time. Previous studies by the Auger collaboration have shown the long-term evolution of AoP and its importance for detector monitoring [159]. For the current SD stations, the average value of AoP is around 3.5 T_{bin}, or in time units, around 88 ns. In the upgraded stations with new faster electronics (120 MHz), we see essentially the same AoP ratios of around 10.5 which corresponds to 88 ns in time units (see Figure 5.12-left).

Figure 5.12-right shows the relation between the AoP and the CLF temperature for the data taken over the month of May 2017 from an EA station. Very weak correlations can be seen for the two parameters, and the fitted slope referring to the temperature dependence of the AoP is less than 0.1%/10°.

The average AoP of the EA stations is distributed within the range of 7.0 to 12.0 T_{bin}. Figure 5.13 shows the survey of the AoP values with the corresponding RMS fluctuation as errors for all upgraded stations. These data are taken during the period of 03/2017 to 05/2017.

5.3.4 FWHM of the SSD MIP signals

The average MIP signal from the SSD of an EA station is shown in Figure 5.14-left. The shape of the MIP signal is narrow since the plastic scintillator bars with a thickness of 1 cm have a fast time response and a good time resolution for the measurement of background particles. Here, the width (FWHM) of the SSD MIP signal is used to monitor the detector performance. The temperature dependence of the SSD MIP signal width is shown in Figure 5.14-right. A positive correlation of ~1% / 10°C can be fitted from the data. From the experimental data, the average value of the MIP signal widths is around ~35 ns for all SSDs. The survey of this parameter for all EA stations is shown in Figure 5.15.

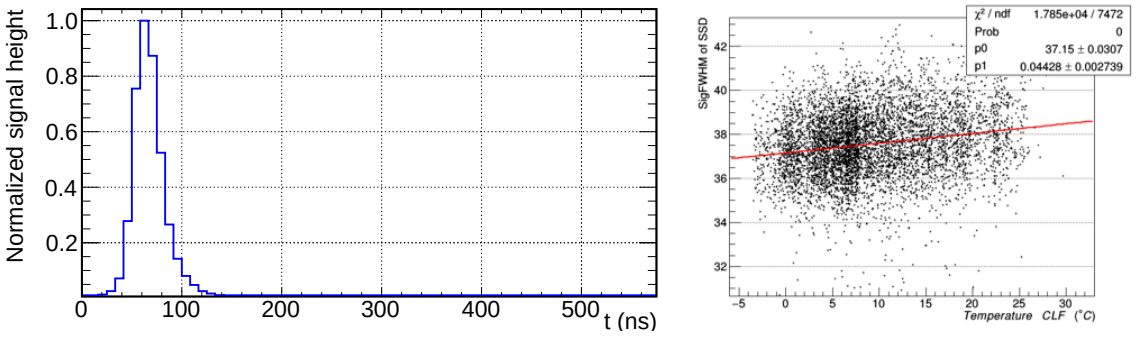

Figure 5.14 – *Left:* The MIP signal shape from an SSD PMT. *Right:* The correlation between SSD MIP signal width and the temperature.

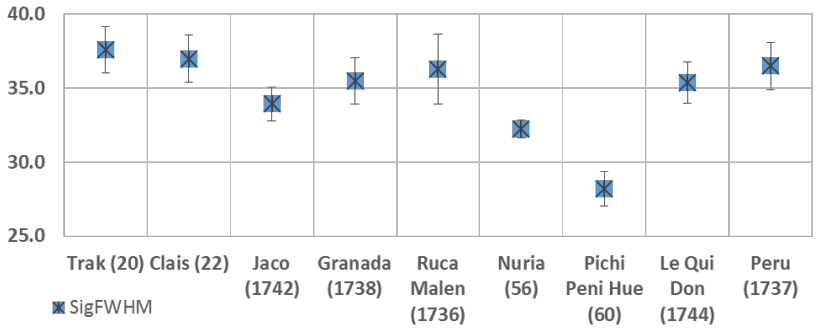

Figure 5.15 – Survey of the average width of SSD MIP signals.

5.3.5 Monitoring of the detector parameters

In the observatory area, the day-night temperature variation is around 20°C. Figure 5.16 shows the related parameters introduced above from the station 20 together with the temperature measured in the CLF as a function of time over the first week of May 2017. From the plots, we can see that the day-to-night fluctuation of these detector parameters due to temperature is: <3% for VEM charge, <5% for MIP charge, ~1% for area-over-peak from WCD and ~3 ns for the FWHM of SSD MIP signals. Concerning the WCD, similar variation was reported for the existing detectors [159]. The real-time monitoring and calibration of the detectors are necessary for precise measurement of shower events. Various monitoring parameters will be available directly in the observatory monitoring program in the near future.

5.4 Shower signals from EA stations

5.4.1 Signal characteristics

In this work, for the shower signals, the baselines are first evaluated by using the *TSpectrum::Background()* function integrated in ROOT-CERN [160]. The *TSpectrum::Background()* function is based on the Sensitive Nonlinear Iterative Peak Clipping Algorithm (SNIP) [161, 162]. It can be used to separate the continuous background from the peaks in the spectrum. The number of iterations (N_{iter}), which is actually the width of the clipping window in the SNIP algorithm, is an important parameter for the background rejection. In the baseline calculation, each FADC trace can be regarded as a spectrum. After calling the *TSpectrum::Background()* function, another spectrum (trace) of the background (baseline) will be generated. As introduced in subsection 5.3.1, the range defined to evaluate the baseline is from 50th to 550th time bin. By comparing the medians of the original and the background traces within this

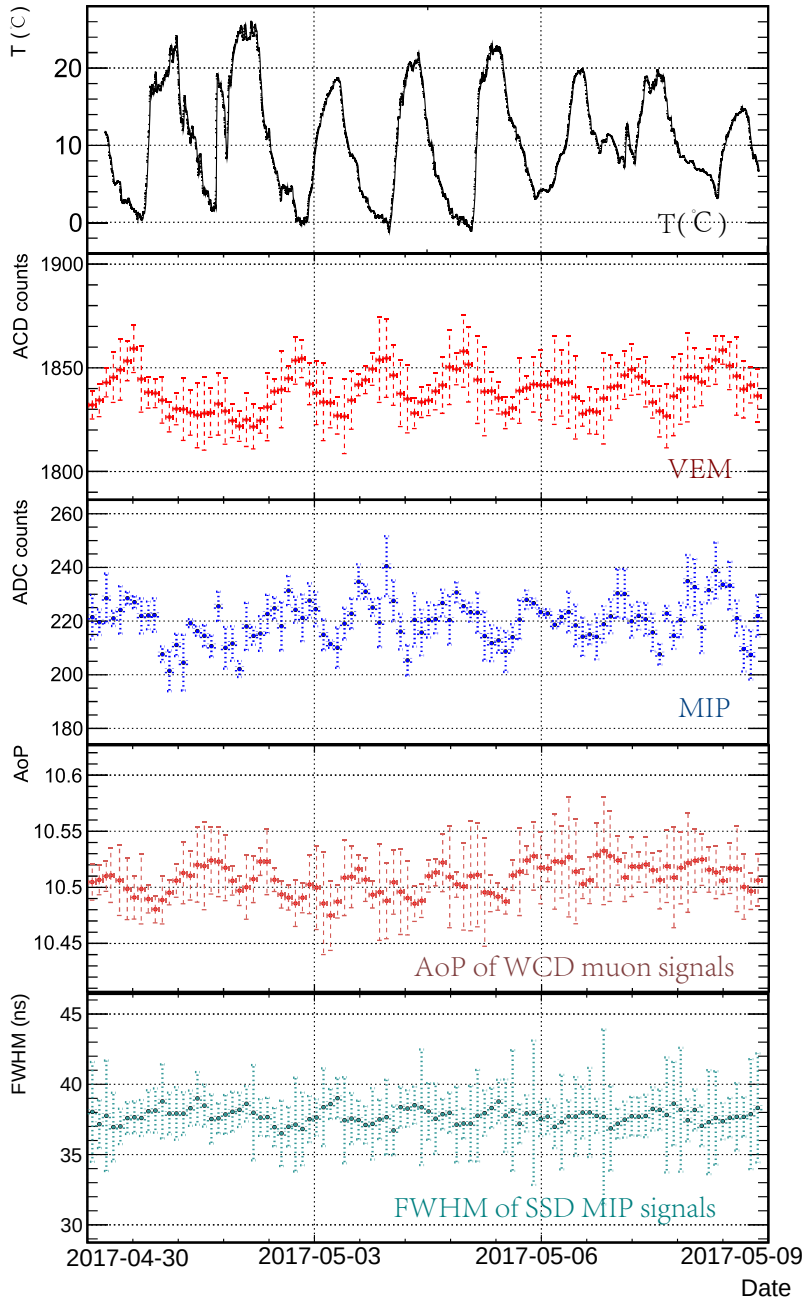

Figure 5.16 – The various detector parameters and the corresponding temperature as a function of time

range, we can evaluate the precision of this method and optimize the parameter, N_{iter} used in the function. In this work, $N_{iter} = 25$ was used as the optimal value since it leads to the lowest bias (<0.5 ADC counts) for the baseline of the FADC trace.

After the baseline evaluation, the baseline is then subtracted from the full signal for each time bin. (see Figure 5.17). The signal amplitude is finally calibrated in VEMs for the WCDs and in MIPs for the SSDs.

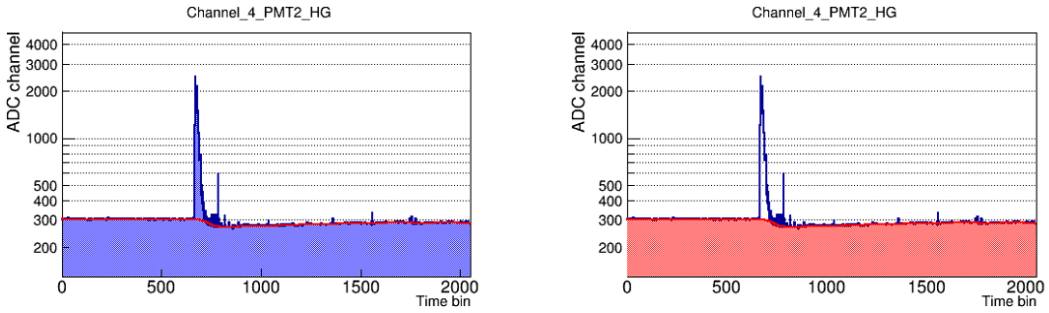

Figure 5.17 – Baseline evaluation and the integrals of the full trace (left) and the baseline (right).

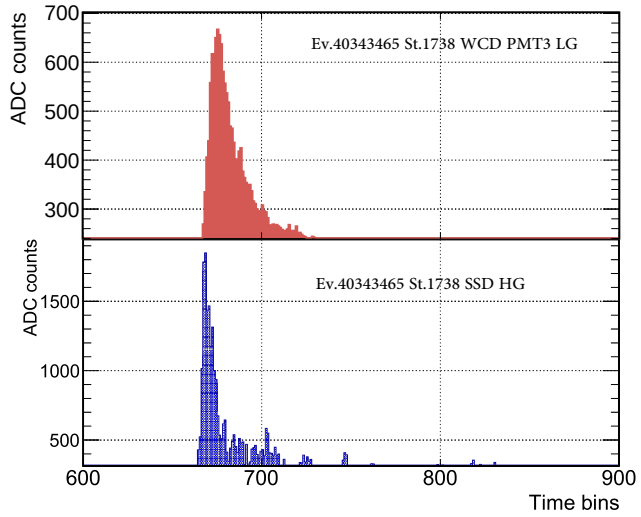

Figure 5.18 – The WCD and SSD signals of station 1738 for the same event.

The two detector types have different response to the electromagnetic (EM) and muonic components of the EAS. Their signals in VEM or MIP units are highly related to the EM energy flux and the muonic flux at ground. Therefore, signal densities sampled in the same position with the WCD and the SSD are essential for the determination of the muonic shower component, which is crucial for primary particle identification.

As explained previously, currently, for the detection of shower events in each station, the SSD is triggered by the WCD. However, a new trigger for WCD muons in coincidence with SSD is being developed. This new trigger mode can “clean” the current MIP peak in the near future.

Figure 5.18 shows the signals of the WCD and the SSD from station 1738 for the same event. The main signal in WCD spreads relatively longer than the one in SSD due to the multiple reflections of the Cherenkov light in the water tank. With the SSD signals, we can clearly see the particles which arrived later than the main flow of secondary particles produced

in the EAS development.

5.4.2 Signals from EA stations compared to the lateral distribution function

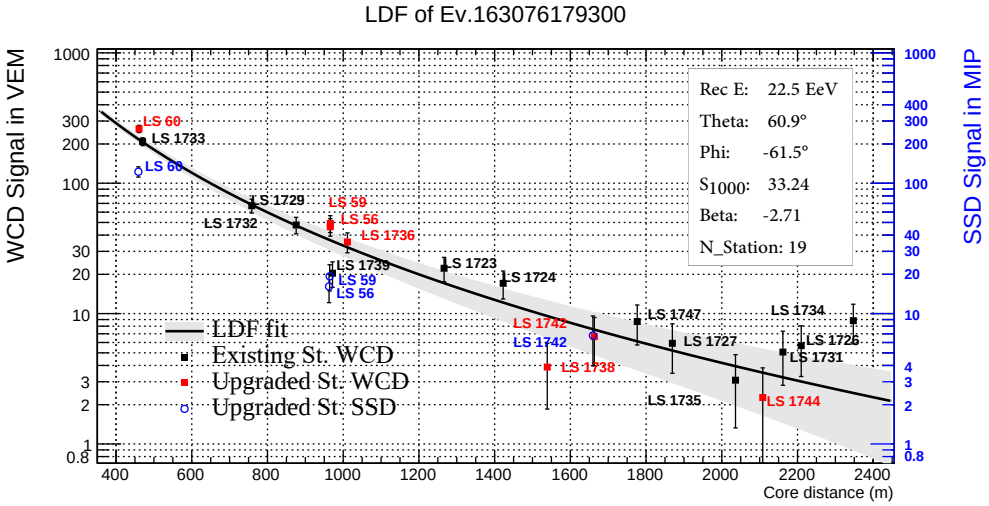

Figure 5.19 – Signals from upgraded stations compared to the LDF reconstructed by the existing stations. Signals from both WCDs and SSDs are not calibrated by the areas of detectors.

The events triggered by the SD array are first selected with the T4 and T5 triggers [101], which is explained in subsection 3.1.2. The arrival direction is obtained by fitting the start time of each SD signal to a plane front. The shower core on the ground can be obtained from the fits of the SD signals. The lateral distribution function (LDF) of the air shower can then be described as a modified NKG function introduced in Equation 3.2.

Figure 5.19 shows an example event with a primary energy of 22.5 EeV. For this event, 12 existing stations and 7 upgraded stations were triggered. The LDF in the plot is fitted with signals from the existing stations. As it can be seen in Figure 5.19, the WCD signals from upgraded stations are in good agreement with this LDF curve, and the SSD signals are relatively lower than the WCD signals, as expected.

5.4.3 Global LDF of the EA signals

The global LDF corresponding to the signals from upgraded stations is shown in Figure 5.20. Signals from WCDs and SSDs normalized by the shower size are plotted as a function of distance from the station to the shower core. The LDF of S_{WCD} from upgraded stations agrees

well with the LDF of $S_{\text{WCD-existing}}$ from the existing stations. Since in the area close to the shower core, the EM component has a higher proportion than the muonic component, S_{SSD} is higher than the LDF of S_{WCD} in the region close to the shower axis. In the region further away from the core, the muonic component turns to be dominant in the proportion compared to the EM component, S_{SSD} then gets lower than the corresponding S_{WCD} along with the increase of the core distance. Correspondingly, the ratio of $S_{\text{SSD}}/S_{\text{WCD}}$ is observed to be larger than 1 for the region near the shower axis and then tends to be the ratio of the detector areas ($\frac{A_{SSD}}{A_{WCD}}$~0.4) at large distances (>700 m). This can be understood as an effect of the SSD sensitivity to the EM component of the EAS and the relatively smaller area of SSDs.

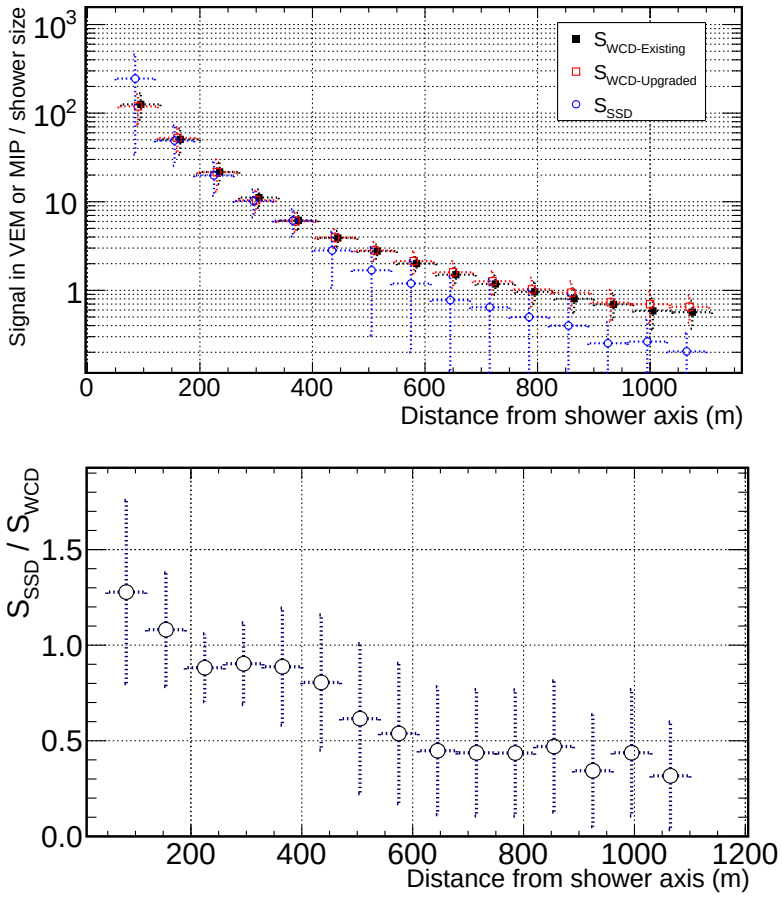

Figure 5.20 – *Upper:* The global LDF of the signals from upgraded stations and existing stations. 3084 events reconstructed with the Auger 750 m array are selected for this analysis (Event selection: T4 events, ≥4 existing stations triggered, no saturation in the stations.) *Bottom:* The ratio of $S_{\text{SSD}}/S_{\text{WCD}}$ as a function of distance from the shower axis.

5.5 Study of the doublet signals

Some detectors in the EA area are deployed close to each other (spacing ~11 m) as doublet or multiplet stations. Since the footprint of a typical EAS extends over several km^2, the signals from these multiplet stations can be regarded as measurements in the same point of the shower. Therefore, the doublet stations are usually deployed for the study of signal accuracy when they are equipped with the same detector components.

5.5.1 WCD signal accuracy of the existing stations

Before the AugerPrime upgrade was implemented to the EA stations, the shower events recorded by doublet stations from 04/2016 to 08/2016 were taken for the study of signal accuracy. With the method introduced in [163], the uncertainty of the WCD signals as a function of the signal in VEMs is shown in Figure 5.21. As we can see in Figure 5.21, the signal uncertainty is around 10% and imrpoves to ~1% for large signals (> 100 VEMs).

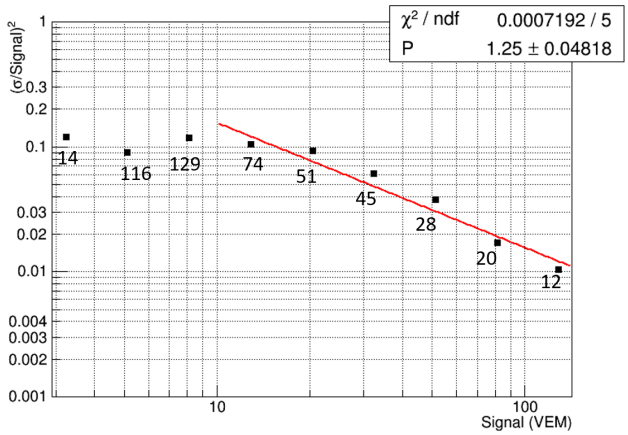

Figure 5.21 – Signal accuracy of the previous EA stations. The number of events in each bin is attached.

5.5.2 WCD signals from upgraded doublet stations

The signal correlations of upgraded doublets for WCDs and SSDs are shown in Figure 5.22 and Figure 5.23. The S_{WCD} from each station in the doublet is corrected by the LDF to the mean distance of the doublet. This correction can reduce the bias due to the difference of a steep LDF over the 11 m distance. Good correlation can be seen for S_{WCD} from both high-gain (HG) and low-gain (LG) channels. For S_{SSD}, therefore, the doublet signals of small amplitudes (<100 MIP) are in good agreement. Since, currently, there is no LDF fitted to S_{SSD} available

for the doublet signal correction, the signal difference for the large signals (from LG channels) measured near the shower axis is relatively larger than that for the small signals.

A preliminary result from the study of signal accuracy is shown in Figure 5.24. For the WCD signal, the signal accuracy is around 10%, which is comparable to the signal accuracy of the existing stations [163]. Further studies on signal accuracy will be performed with better statistics.

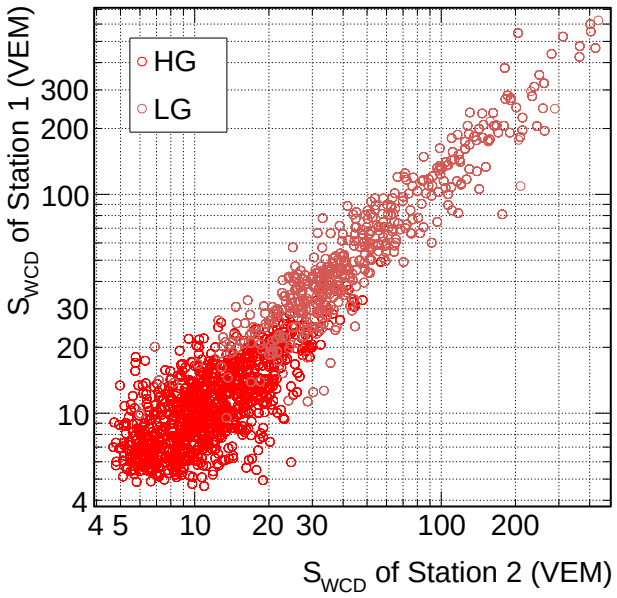

Figure 5.22 – The correlations of doublet WCD signals.

5.6 Summary

The AugerPrime engineering array has been taking data since October 2016. Detectors are calibrated with the charge of single VEM for S_{WCD} and single MIP for S_{SSD}. The upgraded stations with WCDs and newly deployed SSDs operate with good stability at the Auger site under a harsh environment with day-to-night temperature fluctuations of >20°C. Signals from EA stations are in a good agreement with the LDF curve fitted with signals from the existing stations. The global LDF for S_{WCD}, normalized by the shower size, agrees well with the results of the LDF fitted to the existing stations. Furthermore, the global LDF of S_{SSD} shows the SSD sensitivity to the EM components of the EAS, as expected. The signals from doublet stations are well correlated and the measured signal accuracy for WCD is around 10%. Further studies with better statistics are currently underway. This work has been reported by the author of this thesis as a proceeding for ICRC 2017 (*First results from the AugerPrime engineering array*,

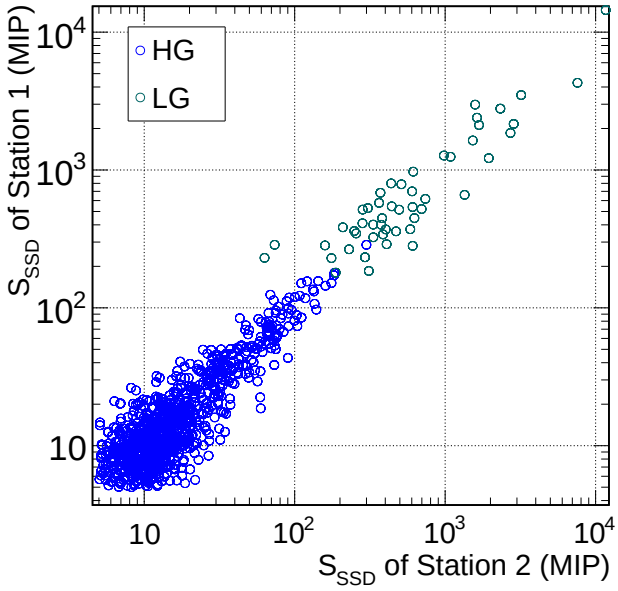

Figure 5.23 – The correlations of doublet SSD signals.

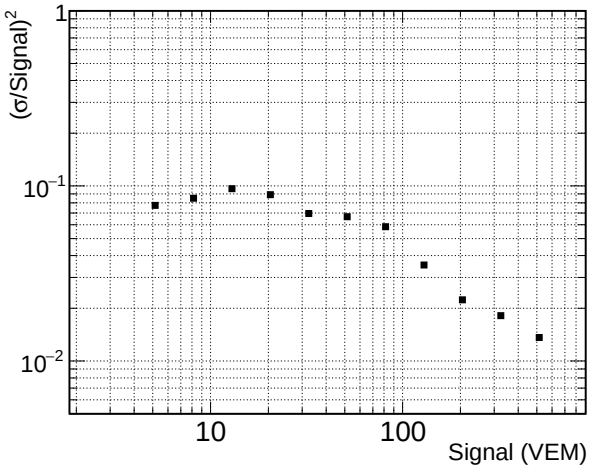

Figure 5.24 – The measured WCD signal accuracy of upgraded stations with respect to the signal amplitude in VEM.

PoS (ICRC2017) 449).

6

The LHAASO project

The Large High Altitude Air Shower Observatory (LHAASO) is a ground-based EAS observatory located at 4410m a.s.l. in Sichuan Province, China. The LHAASO project is a multipurpose project for the detection of high-energy gamma rays and cosmic rays with hybrid techniques. The three main goals of LHAASO are surveying the gamma sky above 100 GeV, searching for cosmic-ray origin among galactic gamma-ray sources and measuring the cosmic rays above 30 TeV. The LHAASO observatory covers an area of 1.3 km^2 and consists of four types of detector arrays, the 1 km array (KM2A) of electromagnetic particle detectors (ED) and muon detectors (MD), the Water Cherenkov Detector Array (WCDA), and the Wide Field of view Cherenkov/fluorescence Telescope Array (WFCTA). Currently, the Observatory is under construction. One fourth of the Observatory is expected to be finished in 2018 and the whole site is expected to be completed by the beginning of 2021.

In this chapter, the science case (section 6.1) and the detector arrays of LHAASO (section 6.2) are introduced.

6.1 Scientific case of LHAASO

LHAASO is expected to be the most sensitive instrument aiming at solving the open questions in galactic cosmic ray physics by studying EAS induced by both charged particles and gamma rays. The LHAASO observatory consists of a complex detector array. The fundamental techniques used in LHAASO detectors are similar to the ones which have been used in other related experiments like the Pierre Auger Observatory [69] and KASCADE [164]. Based on the experience from these experiments, the four detector arrays (KM2A-ED, KM2A-MD, WCDA, and WFCTA) in LHAASO have been designed and organized to fulfill the specifications requested by the corresponding physics purposes. The main goals of the LHAASO project are summarized as follows:

Search for cosmic-ray origin among galactic gamma-ray sources

As about 170 very-high-energy gamma-ray sources have been found in the last two decades [165–167], a comprehensive observation of VHE gamma rays with a precise measurement of their energies is requested to provide evidence for the origin of cosmic-ray photons and to distinguish between scenarios involving a hadronic origin with π^0 decays and purely electromagnetic scenarios where VHE gamma-rays are produced by inverse Compton scattering of accelerated electrons [168, 169].

Survey of the gamma sky above 100 GeV

A deep survey of very-high-energy (VHE) gamma-ray sources for the northern sky will certainly contribute to the global monitoring of transient emissions from active galactic nuclei (AGN) and gamma-ray bursts (GRB). The survey is also significant for the multi-wavelength investigation, which aims at a better understanding of the evolution of galaxies and the acceleration mechanisms in gamma-ray sources. With the large ground-based arrays (KM2A and WCDA), LHAASO can provide a large effective area with a high duty cycle (>95%). A well-configured combination of different detectors in LHAASO offers a high capability of background rejection for gamma-ray observation. With these advantages, LHAASO is proposed to play an irreplaceable role in VHE γ-ray observation in the next decade. Figure 6.1 shows the sensitivity of LHAASO for the gamma-ray astronomy. In the energy range of around 100 TeV, LHAASO will be the most sensitive observatory for gamma rays. Since LHAASO

and the Cherenkov telescope array (CTA) [170] have different advantages in γ astronomy, there is also a possibility to combine the two observatories working complementarily to scan and discover gamma-ray sources above 100 GeV.

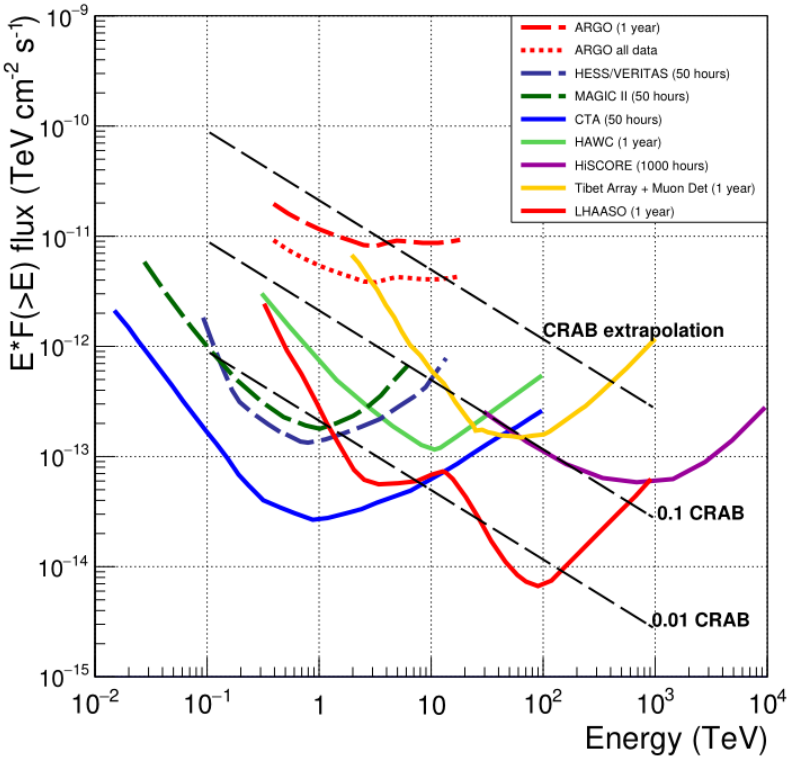

Figure 6.1 – Sensitivity of ground-based experiments for gamma-ray astronomy, LHAASO has a high sensitivity in the energy range of 1 to 100 TeV [171]

Measurement of the cosmic rays above 30 TeV

LHAASO proposes to measure the energy spectrum and identify the mass composition of cosmic rays around the "knee" region (> 10^{14}eV). In the reconstruction of air shower events, there is a strong mutual dependency between the primary energy and the primary particle type. Since the air showers of PeV level just reach the maximum of shower development around the observatory level of 4410 m a.s.l., this makes the shower-to-shower fluctuations to be minimal. Each detector array in LHAASO has its specialty in the EAS detection. Each detector array is described in section 6.2. The WFCTA is a precise calorimeter of the shower size. The WCDA supports for an accurate measurement of the shower geometry (shower core and arrival direction). The EDs and MDs of KM2A can sample the signal densities near the core on the ground induced by EM and muonic components of the shower, respectively. By combining the measured data from these detector arrays, an accurate reconstruction of

the shower properties can be performed. The related simulations and analysis preparation for this topic are presented in chapter 7. Benefiting from the advantages of the observatory elevation and the hybrid observation of EAS, LHAASO is capable of measuring the energy and classifying the chemical nature of the primary particle with a high accuracy [172].

Besides these major scientific goals, LHAASO is also expected to be used for the exploration of frontier topics in physics, such as searching for dark matter, exploring the quantum gravity or the effects of the Lorentz invariance violation with transient phenomenon and studying the particle physics phenomenon in the energy range of LHC (Large Hadron Collider) .

6.2 LHAASO implementations

To fulfill the physics objectives of LHAASO, a complex detector array consisting of 4 types of detectors is designed to be deployed. Figure 6.2(c) shows the layout of the LHAASO observatory. The whole observatory, covering an area of 1.3 km^2, is composed of various detector arrays, WCDA, KM2A (ED and MD) and WFCTA. The WCDA is located in the central area of the observatory, covering a 300 m $\times$ 260 m rectangular area. It consists of three large water pools, which are segmented into 5 m $\times$ 5 m grids as single detector units. WCDA has a large duty cycle (>90%), a good background-rejection capability, a wide field of view (~1.5 sr) and a high sensitivity for γ astronomy. One of the WCDA pools is used for the detection of shower geometry in cosmic-ray measurements. It has a good accuracy in the reconstruction of shower cores (~2.5 m) and arrival directions (~0.3°) [174]. The telescopes of WFCTA are settled beside this shower core detector array (See Figure 6.2(b)) and pointing to the sky. They work as calorimeters of air showers with an energy resolution of $\frac{\Delta E}{E}$ ~20%. The KM2A, surrounding the central area, is a complex array itself composed of electromagnetic particle detectors (ED) and muon detectors (MD). The KM2A detectors are uniformly distributed in the rest of the observatory area, covering nearly 1 km^2. Each detector array in LHAASO has its own specialty. In the EAS detection, the data measured by these detector arrays can be combined together. The measured data in this hybrid observation are used to achieve a precise reconstruction of the shower parameters such as primary energy, identification of the primary particle, and shower direction. In the following subsections, the detailed information of each detector type is introduced.

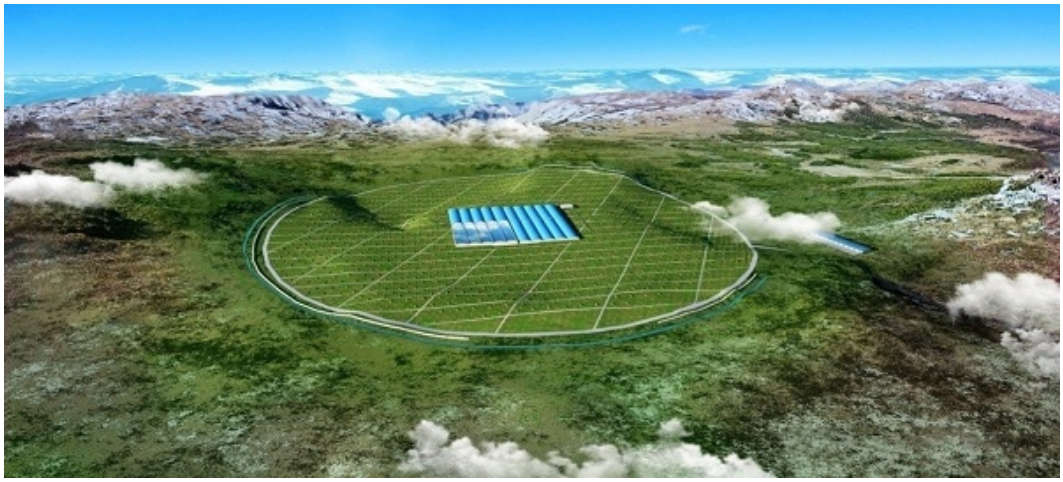

(a)

(b)

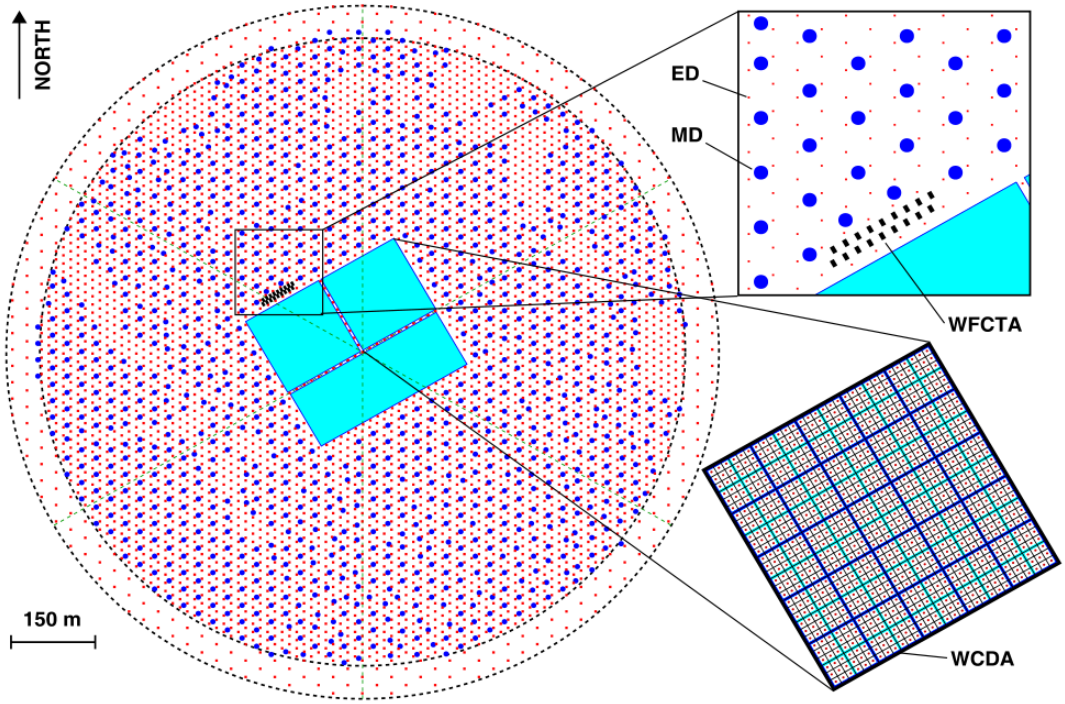

(c)

Figure 6.2 – 6.2(a) shows the preview of the LHAASO site, 6.2(b) shows the preview of the detectors. The layout of detector arrays is displayed in 6.2(c) [173].

6.2.1 KM2A

The KM2A, covering an area of one square kilometer (diameter ~ 560 m), consists of 5242 electromagnetic particle detectors (ED) with a spacing of 15 m and 1171 muon detectors (MD) with a spacing of 30 m. The configurations of EDs and MDs are described as follows:

Electromagnetic particle detector

Each electromagnetic particle detector in KM2A is a 1 m^2-area plastic scintillator detector, since the plastic scintillator has a fast response time and a high detection efficiency (above 95%). The basic structure of the detector unit is shown in Figure 6.3. Each detector unit is assembled with four modules of plastic scintillators. Each module of scintillators is 100 × 25 × 2.5 cm^3 and with 32 grooves on the upper surface. The outer surface of each scintillator module is covered with a layer of Tyvek material, which is a diffusion reflective material (reflectivity ~92%), to increase the light collection. Wavelength-shifting fibers of 2.7 m-long are embedded in the grooves of each module [148, 175]. The WLS fibers are bundled and coupled to a photomultiplier tube. The photomultiplier tube placed in the dark sleeve converts the light signals to electronic signals. In the electronics system, the signals are delivered through a coaxial cable to the data acquisition system. A KM2A-ED prototype array with 42 detectors, which corresponds to ~1% of the designed scale, was deployed at the ARGO-YBJ site in 2010 to study the long-term performance and stability of the detectors [176, 177].

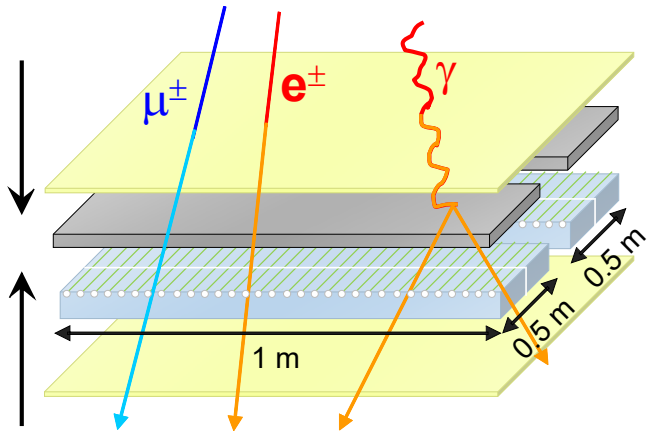

Figure 6.3 – An ED is composed of 4 scintillator units run along with WLS fibers in its grooves [175].

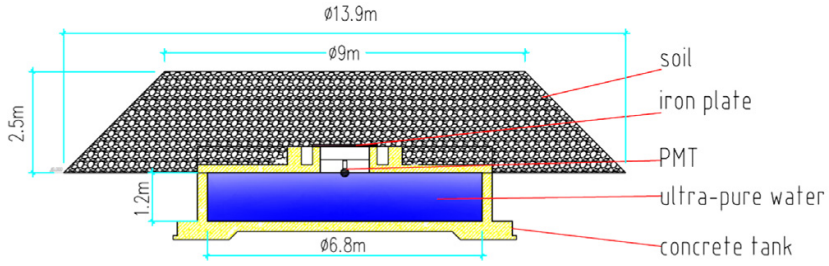

Figure 6.4 – The KM2A muon detector is filled with 44 tons of ultra-pure water and covered by a 2.5 m-thick layer of overburden soil to shield the low-energy electromagnetic components of air showers [178].

Muon detector

The muon detector in KM2A is a water Cherenkov detector, similar to that of the Auger surface detector. The muon detectors are buried in the ground with a 2.5 m-thick layer of soil shielding low-energy electromagnetic components in the air showers. Figure 6.4 shows the scheme of muon detectors. Each MD is a cylinder-shape water tank with a diameter of ~6.8 m and a height of ~1.2 m. The inner surface is made with Tyvek materials to reflect the Cherenkov light generated in the tank and increase the light collection. One photomultiplier tube of 8 inches is installed at the central axis of the cylinder to collect the light signals. Two MD prototypes have been deployed with a spacing of 30 m in the center of the ED prototype array at the ARGO-YBJ site to verify the detector design [178].

6.2.2 WCDA

The WCDA, which is designed to constitute the central area of the LHAASO site, has a total effective area of 78000 m^2 and is composed of two water ponds of 150 × 150 m^2 and one pond of 110 × 300 m^2. The depth of the water ponds is about 4.4 m. Figure 6.5 shows the layout of LHAASO-WCDA. The whole WCDA is divided into 3120 detector units and each unit is a 5 × 5 m^2 cell equipped with an 8-inch hemispherical PMT installed at the bottom and looking upwards into the water. One of the 150 × 150 m^2 ponds is also used as the shower core detector array. Each cell in this pond is equipped additionally with a 1-inch small PMT, which allows to extend the dynamic range for cosmic rays detection at the knee region (up to 10^{18}eV). The entire pond is light-tight and covered by shading and canvas materials. Black plastic curtains are used between the detector units preventing the Cherenkov light from entering the adjacent units. Detector units are not completely shielded by the curtains, and a certain height is reserved at the bottom of the curtain walls to allow for water recycling. The water purification system of WCDA is composed of various filters (multimedia, activated

carbon, fine, and ultra-fine filters) and UV lamps. This system can ensure the attenuation length of visible lights in WCDA above 15 m. The purified water can be poured into the ponds by pumps through a group of pipes distributed at the bottom of the ponds. The pipes have many small holes punched on the surface, which allows a uniform injection of the water. Another group of pipes is installed on the top of the ponds (~40 cm below the surface of the water), which draws the water into the purification system [179].

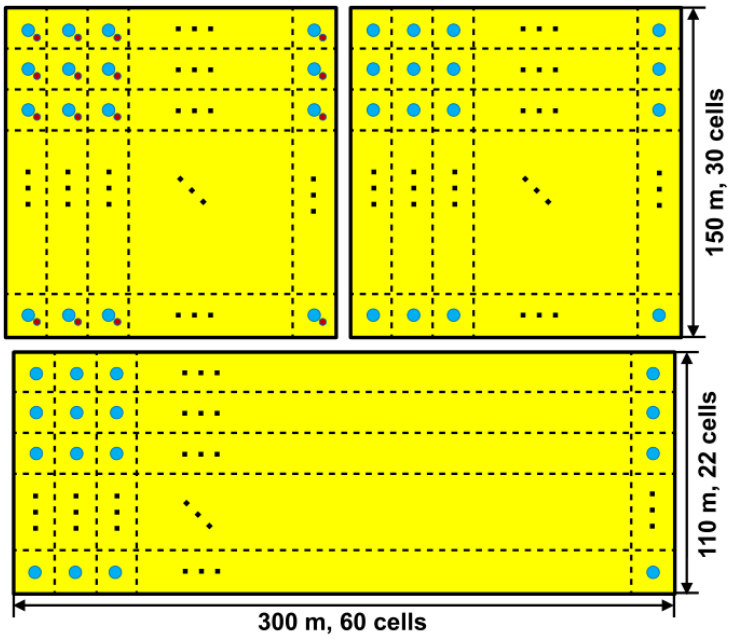

Figure 6.5 – The WCDA consists of 3 water ponds and is filled with totally 350000 tons of filtered clean water. Each detector unit is a 5×5 m^2 cell. [180].

The LHAASO-WCDA has a series of advantages in air shower observation [181, 182]. First of all, it's an all-weather detector array with a 100% duty cycle, which supports for a continuous detection for the sources in a burst status. Secondly, it has a large field of view of $\frac{2\pi}{3}$ and a low energy threshold down to 100 GeV, which is useful for the search of transient sources. Thirdly, it has a good capability for the γ/p separation, since the water Cherenkov detectors are sensitive to the secondary core structures of the shower. In the air shower development, nuclei-induced showers always have secondary cores while the γ-induced showers don't, which is the main characteristics used to distinguish γ from the background cosmic rays. Finally, in the measurement of the shower geometric parameters, WCDA has accurate resolutions of $\sim$ 2.5 m for the shower core and $\sim$ 0.3 $^\circ$ for zenith and azimuth angles [174]. This is crucial for the shower reconstruction of both γ-induced and charged-particle-induced showers. A WCDA prototype array of 3×3 units was constructed in 2011 near the hall of ARGO-YBJ. It has been operated to study the performance of the

entire WCDA system including water cycling system, detector modules, DAQ, slow control system and etc [183–185].

6.2.3 WFCTA

The wide field-of-view (FoV) Cherenkov telescope array (WFCTA) is designed to measure the Cherenkov light in the air showers based on the techniques used in the imaging atmosphere Cherenkov telescopes (IACT). Each telescope in the WFCTA has a 5 m^2 aluminized spherical mirror that reflects Cherenkov light onto the camera composed of 1024 pixels. Each pixel is a PMT or a Silicon photomultiplier (SiPM) with a Winston-cone light collector. The total FoV of each telescope is $14^\circ \times 16^\circ$ and each pixel corresponds to $\sim 0.5^\circ \times 0.5^\circ$. Once the incident Cherenkov/fluorescence light gets reflected by the mirror and enters the camera area, the SiPMs on the camera will convert light signals into electronic signals and then these signals will be processed by the electronics system and sent to the data acquisition system. A typical elliptic pattern for Cherenkov light or a track-like pattern for a fluorescence light can be imaged in the camera and displayed in the DAQ system. Each entire telescope can be packaged in a 1/4 standard sea container. A base with three wheels under the container and an electrical motor driven system equip the telescope, which facilitates for transporting or elevating the detector. A WFCTA prototype is shown in Figure 6.6.

In the LHAASO project, the WFCTA, consisting of 12 telescopes, is planned to be deployed near the WCDA to measure the cosmic-ray spectra at the knee region (see in 6.2(c)). WFCTA is an important part of the LHAASO project for measuring the cosmic-ray spectra across about five orders from 10^{13} to 10^{18} eV. In order to fulfill this goal, WFCTA is designed to be working in three phases. In the first two phases, WFCTA will work in the same mode of atmospheric Cherenkov light observation but in different layouts. In the first phase, eight telescopes will be divided into two groups and measure cosmic rays with primary energies of 10^{13} to 5×10^{14} eV. Four of them will point to the zenith and the other four to zenith angle = 30°. In the second phase, five telescopes will point to zenith angle = 25°, and the other seven to zenith angle = 38°. The concerned cosmic-ray energy range of this phase is from 10^{14} to 10^{16} eV.

In the third phase, WFCTA will be working in the mode of atmospheric fluorescence observation and measuring cosmic rays with primary energies from 5×10^{15} to 10^{17} eV. In this last phase, the telescopes are planned to be divided into three groups, located 4 or 5 km away from the center of the LHAASO site and overlooking the ground arrays (WCDA and KM2A).

From 2008 to 2010, two WFCTA prototypes, which were fabricated following the design described above and configured with a camera of 16×16 regular PMTs, have been operated at

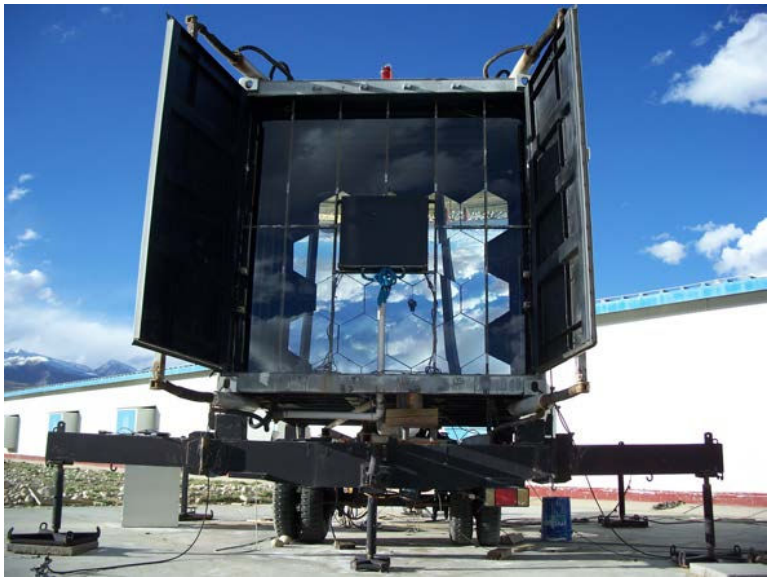

Figure 6.6 – The WFCTA prototypes at ARGO-YBJ site.

the Argo-YBJ site. It is verified that the entire telescope system has a good long-term stability and performance in the measurement of cosmic rays [186, 187].

7

Simulations and analysis preparation of LHAASO

7.1 Detection of atmospheric Cherenkov light in astro-particle experiments

In the development of the EAS, the majority of the secondary particles are charged particles. About one third of the charged particles in the shower front will generate Cherenkov light since their velocities have exceeded the speed of light in the air [188]. The Cherenkov light generated in the shower development can be measured to study shower properties.

The atmospheric Cherenkov light is mainly produced by electrons in the EAS. The electromagnetic and the Cherenkov light components almost simultaneously reach their maximum in the shower development. As introduced in subsection 2.3.4, the opening angle of atmospheric Cherenkov light (θ in Equation 2.9) is generally less than ~1.4°. The polarized Cherenkov light propagates in a narrow cone and arrives at the observation level in a small circular area. The diameter of the Cherenkov ring at the observation level is less than 250 m. (See in Figure 7.1). The arrival times of Cherenkov photons are generally rather short (3 to 5 ns) due to the instantaneous emission and the velocity of light [189, 190]. During their transportation in the atmosphere, Cherenkov photons can also be affected and get scattered or absorbed in some processes such as Rayleigh scattering, Mie scattering, and Ozone absorption [191].

The detection of atmospheric Cherenkov light is widely used in astro-particle experiments. The atmospheric Cherenkov detectors are generally designed in two types: non-imaging or imaging detectors.

Detectors using non-imaging methods are usually implemented as ground-based detector arrays vertically pointing to the sky measuring the densities and the arrival times of Cherenkov photons generated in the shower development. The shower geometry and the shower maximum can be reconstructed by fitting the lateral distribution of Cherenkov light or determined with the timing information obtained from the detector array [192–195].

Detectors using imaging methods are called imaging Cherenkov telescopes and are composed of a group of mirrors and a camera made of photodetectors. The mirrors can collect

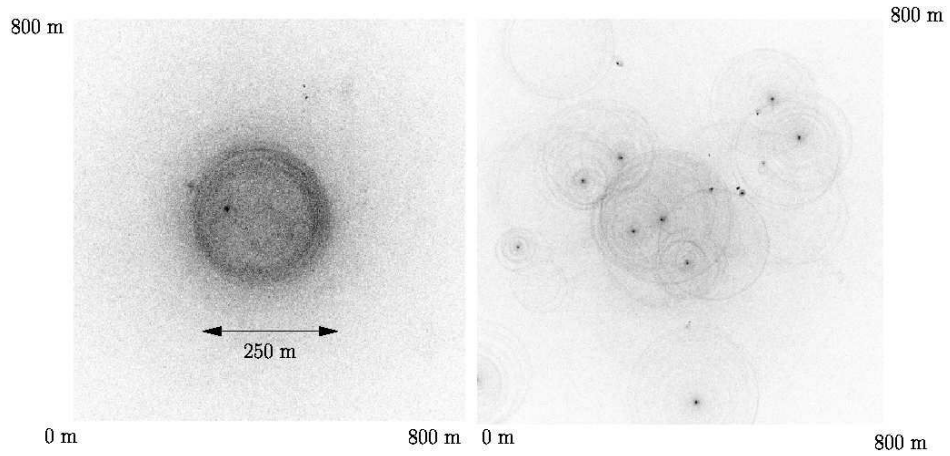

Figure 7.1 – The simulation results of Cherenkov rings of the shower initiated by a γ-ray of 300 GeV (left) and by a proton of 1 TeV (right), respectively. The picture is taken from ref.[191].

the direct Cherenkov light from the shower and focalize the photons onto the camera. The Cherenkov light reaching the image plane is measured by each photodetector in the camera. By recording the arrival time and intensity of the incident light in each pixel of the photodetector arrays, an image for a given event is available for the reconstruction of energy and direction of the primary particle.

The imaging atmospheric Cherenkov telescopes (IACT) are mainly used for high-energy gamma-ray observation. IACTs were first used in the Whipple experiment [196], and then developed and deployed in a series of experiments , such as HEGRA [197], HESS [198], CANGAROO [199], VERITAS [200], MAGIC [201] and the future CTA [202]. The IACTs are generally equipped with a mirror of large area. They are normally designed for pointing to a gamma-ray source with a narrow field of view and small pixels (0.1°). Therefore, IACTs have good angular resolution, high sensitivity and good separation capability between the primary γ and hadrons. IACTs have unmatched performances in the detection of gamma-ray sources around TeV energy range.

Compared to the IACTs employed in γ-astronomy experiments, the WCFTA telescopes, which are used to measure cosmic rays, need to cover a larger field of view (FoV) ($14^\circ \times 16^\circ$) for each telescope. Correspondingly, the pixel size of WFCTA telescopes is designed to be $\sim 0.5^\circ$. Furthermore, WCFTA telescopes also have the advantage of good cost-effectiveness and simple mechanical structure compared to IACTs.

Telescope type	Mirror effective area	FoV	Pixel
CTA-LST	~ 368 m^2	4.5º	0.1º
CTA-MST	> 88 m^2	> 7º	< 0.18º
CTA-SST	~ 6 m^2	~ 9º	~ 0.24º
LHAASO-WFCTA	~ 5 m^2	14º$\times 16$º	0.5º

Table 7.1 – Optical parameters of Small Size Telescope (SST), Medium Size Telescope (MST) and Large Size Telescope (LST) in CTA [203] and of WFCTA telescope in LHAASO.

7.2 Components of the WFCTA telescopes

The WFCTA telescope is composed of six main components: mechanical system, light collection system, imaging system, electronics system, power supply system, and slow control & monitoring system.

The mechanical system consists of a 1/4 standard shipping container (2.9 m × 2.5 m × 2.38 m), a base with feet and wheels and a set of electric motor-driven systems. The mechanical system of the telescope is a supporting structure protecting the whole detector system during its operation in the field.

The light collection system of WFCTA is a spherical-shape mirror made of 20 entire hexagon sub-mirrors and 5 half hexagon sub-mirrors (See in Figure 7.2). Each sub-mirror has a curvature radius of 5800 mm with a tolerance range of ±20 *mm* and is coated with a layer of aluminum on the surfaces. MgF_2 films are coated on the aluminum layer to protect it from being oxidated. The total area of mirrors is about 5 m^2. The reflectivity of the mirror in the ultraviolet band is larger than 82%. The assembled mirror module can reflect the incident light to the central area of the sphere, where the camera is installed. For a bunch of collimated incident light, the radius of the focalized spot at the camera surface is less than 1 cm.

The imaging system of WFCTA telescope consists of 1024 photodetectors (PMT or SiPM) installed in a 32 × 32 array as a camera. Each photodetector corresponds to 0.5° pixel. The whole camera is enclosed in an aluminum box and fixed at the focal plane, at a distance of 2870 mm from the mirrors. Optical filters are installed at the entrance window of the telescope and in front of the camera. These filters can reject the photons with wavelength from 500 to 650 nm, which is typical wavelength range of night sky background.

The electronics of WFCTA is implemented with either classical or ASIC-based electronics. The electronics in current prototypes is composed of a front-end electronics (FEE) module based on a 50 MHz high-speed Flash ADC (FADC) module, an FPGA-based online trigger module, and a Data Acquisition (DAQ) module. The FEE first filters the signal, amplifying, widening, and digitizing the analog pulses. Then the trigger module will discriminate between

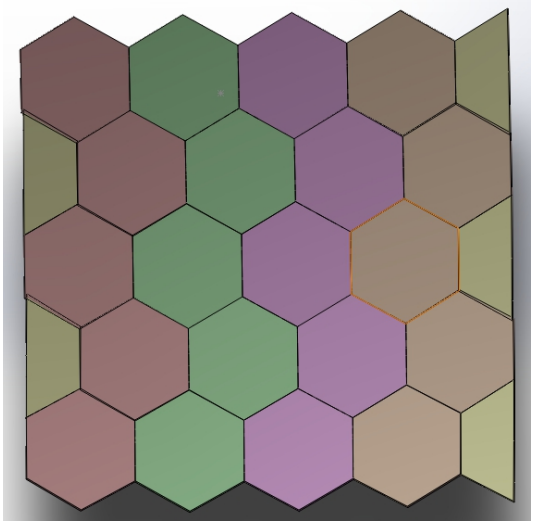

Figure 7.2 – The layout of the 25 mirrors in WFCTA telescope. Picture offered by the LHAASO-WFCTA team in IHEP.

the signal of Cherenkov light (or fluorescence light) and the night sky background (NSB). Finally, the DAQ module will record the triggered signals and save them onto hard disks. In order to avoid the effects of signal attenuation and noise interference, the electronic modules are installed together with the camera to reduce the cable's length. The whole electronic system is powered by two low-voltage power supplies, which are placed in the shipping container, with outputs of +7 V and -7 V, respectively. The DAQ module of the WFCTA electronics has serial ports and an additional ADC and supports for slow control and detector monitoring. Detector operation parameters such as the door switch status, temperatures from each sensor, voltages and currents of each module, can be remotely monitored.

7.3 Simulation code of the WFCTA

The simulation program of the WFCTA is designed to calculate the detector response based on the Cherenkov photons at the observatory level simulated by CORSIKA. For the previous prototypes of WFCTA telescopes, simulation codes in C/C++ have been developed and applied to the prototype experiments. Along with the new design of the telescopes, a new version of simulation code with better compatibility with the LHAASO software framework and a complete process for the simulation of hardware response is required.

7.3.1 Update of the "NewTel" simulation code

From 2015 to 2016, together with collaborators from IHEP, China, we have developed a new simulation code for LHAASO-WFCTA called "NewTel". The NewTel code was designed to be a user-oriented program with effective and maintainable modules. Therefore, the code is required to be resource-efficient in memory usage, complete in hardware simulation, modularized for maintenance, and flexible for various users' purposes. To fulfill these goals, we improved the code in several aspects:

- **Reorganize the frame of the code in a modularized structure.** For obtaining the final detector response of the WFCTA for the detection of Cherenkov light, the main processes to be simulated are optical ray-tracing of incident photons, signal process in the camera, pattern recognition of the Cherenkov image, and file Input/Output (I/O). The new version of "NewTel" is composed of a main c++ class "WfctaSimulation" and several branch classes ("WfctaSimConfig", "WTelescope", "WCamera", "CER_Event" and etc.) The class "WfctaSimulation" governs the whole simulation process. Each branch class implements the calculation in corresponding hardware or controls the calculation based on the simulation options. The modularized structure makes "NewTel" convenient for the WFCTA team to maintain and further develop the code.

- **Integrate the simulation options to an input file.** The definition of related options in the simulation such as the layout of the WFCTA, the pointing direction of each telescope, configurations of photodetectors, electronics, and trigger, and etc. are integrated into an ASCII file. The example of an input file with default options is shown in Figure 7.3. Users can adjust the configurations for their own purposes (layout optimization, algorithm comparison and etc.) by modifying these parameters in the input file.

- **Optimize the functions for faster computation.** The algorithms of each step in the simulation are improved in order to reduce the memory load and save the CPU time. For the file I/O of the code, C functions are used in the readout of binary files from CORSIKA since it is faster than the C++ stream functions. The WFCTA consists of 12 telescopes, each of which has 1024 photodetectors in the camera. During the simulation of optical ray-tracing, all the telescopes need to be kept "open" for a huge number of incident photons. Writing temporary files in the hard disk or creating storage objects in the memory are two ways to manage the telescopes for this simulation step. This leads to a potential issue of the balance between memory load and computational efficiency. According to a group of tests with Cherenkov events with different sizes,

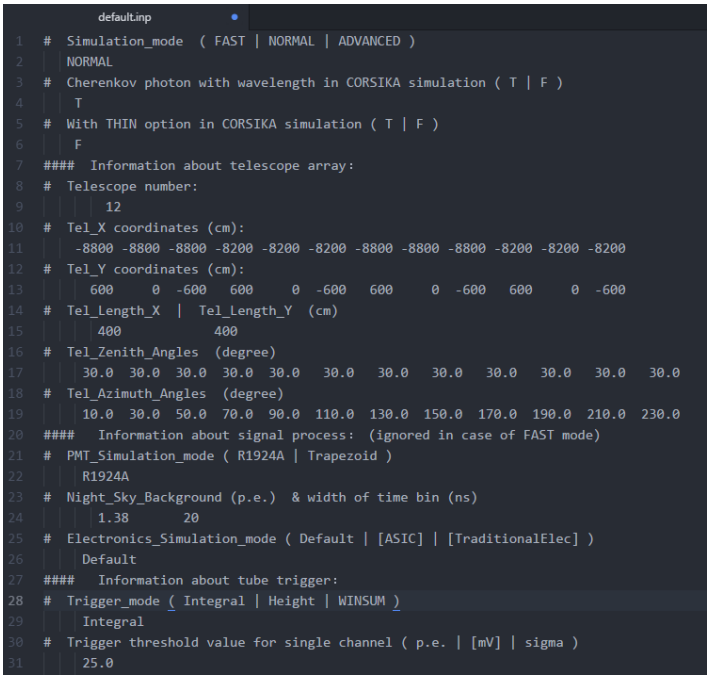

```
default.inp
#  Simulation_mode  ( FAST | NORMAL | ADVANCED )
   NORMAL
#  Cherenkov photon with wavelength in CORSIKA simulation ( T | F )
    T
#  With THIN option in CORSIKA simulation ( T | F )
    F
####  Information about telescope array:
#  Telescope number:
        12
#  Tel_X coordinates (cm):
    -8800 -8800 -8800 -8200 -8200 -8200 -8800 -8800 -8800 -8200 -8200 -8200
#  Tel_Y coordinates (cm):
      600     0  -600   600     0  -600   600     0  -600   600     0  -600
#  Tel_Length_X  |  Tel_Length_Y  (cm)
      400            400
#  Tel_Zenith_Angles  (degree)
     30.0  30.0  30.0  30.0  30.0   30.0   30.0   30.0   30.0   30.0   30.0   30.0
#  Tel_Azimuth_Angles  (degree)
     10.0  30.0  50.0  70.0  90.0  110.0  130.0  150.0  170.0  190.0  210.0  230.0
####   Information about signal process:  (ignored in case of FAST mode)
#  PMT_Simulation_mode ( R1924A | Trapezoid )
    R1924A
#  Night_Sky_Background (p.e.)  & width of time bin (ns)
      1.38       20
#  Electronics_Simulation_mode ( Default | [ASIC] | [TraditionalElec] )
    Default
####   Information about tube trigger:
#  Trigger_mode ( Integral | Height | WINSUM )
    Integral
#  Trigger threshold value for single channel ( p.e. | [mV] | sigma )
    25.0
```

Figure 7.3 – Input file of "NewTel" code in ASCII format.

C++ containers (e.g. *std::map*), instead of the temporary files, are chosen to be used and particularly constructed for parallel processing the photodetector arrays. With these upgrades implemented in the code, the performance of the "NewTel" code is obviously improved when executing the simulations for Cherenkov events with millions of incident photons, especially for the high-energy events above 10 PeV.

- **Upgrade the simulations for the functional components of the telescope.** Besides improving the structure and the algorithms of "NewTel", the simulations of each component are also improved to fit the hardware configurations of the telescope. Compared to the previous simulation code of WFCTA, the new version of "NewTel" has been enriched for the simulation of optical ray-tracing, electronics, and the trigger for Cherenkov image with characteristic patterns. Detailed information concerning these simulations is introduced in the following part of this section.

7.3.2 Simulation of the optical, camera, and trigger system

Optical ray-tracing

The main goal of the ray-tracing simulation is to obtain the wavelength, position, and timing information of Cherenkov photons arriving at each pixel in the camera. In the shower simulation by CORSIKA, in order to reduce the CPU time, the Cherenkov photons are usually

bundled in groups (up to 20 photons for each group) when they are generated in the shower development. Photons in the same group are assigned to have the same geometric and physics parameters. When a bunch of photons, with all its parameters recorded in a "CER_bunch" class, enters the telescope area, it will pass the following steps before finally reaching the photodetector.

- **Determine whether the photon can reach the mirror or not.** The shielding of the camera in front of the mirror and the transmittance of the optical filter and the glass at the entrance window of the telescope are considered.
- **Calculate for the reflection process of photons by one of the sub-mirrors.** In this step, the effect of the roughness ($\sigma_r \sim 0.75$ mm on the local radius of curvature) and the pointing error of each mirror ($\sigma_{exit\ angle} \sim 0.1°$) are considered based on the data measured in the tests of the optical system.
- **Determine which pixel in the camera does the photon reach.** The arrival photon at each pixel will be finally converted into photoelectrons. To fit the real layout of the pixels in the camera, only the photons arriving at the effective area of the photodetectors are counted in this step. The other photons reaching the gaps between circular photodetectors or the ineffective area of the photodetectors are neglected.
- **Consider the quantum efficiency (QE) of the photodetectors.** In the standard output of CORSIKA, the wavelength of Cherenkov light is not saved. The quantum efficiency (QE) of photodetectors is taken into account by CORSIKA at the photon's creation level in order to reduce the number of Cherenkov photons in shower simulation and save computation resources. By editing the QE configuration file in CORSIKA, we can simulate different types of photodetectors. In the current version of NewTel, we follow this setting of QE response. However, the QE curves are different for photodetectors even they are the same type. In order to obtain a more precise simulation, we modified the CORSIKA code to obtain the output with wavelengths of Cherenkov photons. Both standard and modified formats of CORSIKA output are acceptable for NewTel. In the input file, there is a binary option (True/False) to set the format of the Cherenkov photon database (see Figure 7.3). An interface to the QE configuration file of each photodetector is provided in the code for future development.

Responses of photodetectors and electronics in the camera

In the camera simulation, the signal processing and the trigger of each pixel are simulated individually for each photodetector. Firstly, Cherenkov photons of each pixel are filled in a

time window of 1000 ns according to their arrival times. Then, the night sky background noise is added into each pixel. The time intervals between the NSB photons follow an Poisson distribution:

$$p(x, \lambda) = \lambda e^{-\lambda x}, \tag{7.1}$$

where λ is the p.e. number of the NSB per ns, x is the interval in ns. The intensity of NSB can be set in the simulation-option input file. By default, we set it to 0.07 p.e./ns, which was measured on during the operation of the WFCTA prototypes.

For signal processing in each tube, we programmed three modes for different simulation requirements:

- **FAST mode**
  In the FAST mode, the signal in a time window of 1000 ns will be passed directly to the trigger process. The $N_{p.e.}$ of each tube will be stored and the trigger time will be calculated based on the distribution of photoelectrons in the time window. The FAST mode allows us to obtain the partial results of the image with a fast simulation.

- **NORMAL mode**
  In NORMAL mode, the signal will be processed with PMT response functions and electronic shaping functions (see Figure 7.4). The final signal from each electronic channel will be passed to the trigger process. The FWHM of each shaped signal will be calculated and stored in the output file. For PMT response functions, two signal models are currently integrated in the code: trapezoid wave model, which constructs each single p.e. into a trapezoid signal lasting for 13 ns; the PMT signal model, which converts each single p.e. into a PMT response according to a modified Landau distribution.

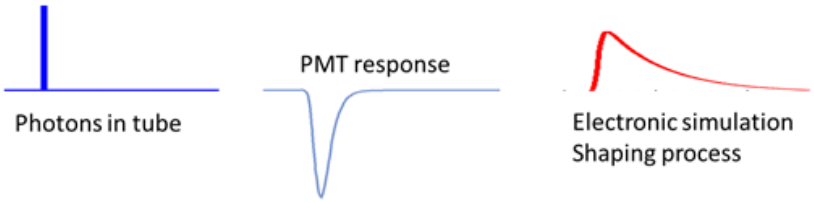

Figure 7.4 – Signal processing for single p.e. in the time window

The PMT model describes the signal p.e. response as:

$$i(t) = n_{p.e.} \cdot G_{PMT} \cdot e \cdot h(t) \tag{7.2}$$

where the $i(t)$ is the response to the photoelectron as a function of time, $n_{p.e.}$ is the number of photoelectrons, G_{PMT} is the gain and e is the charge of electron (1.6022×

10^{-19} C). $h(t)$ is the signal shape of single p.e. and can be expressed as:

$$h(t) = \frac{1}{t_p} exp\left(-\frac{(t-t_t)}{t_p} - exp\left(-\frac{(t-t_t)}{t_p}\right)\right) \tag{7.3}$$

where t_t is the electron transit time in the tube and t_p is the time characteristic of the PMT and expressed as $t_p^2 = t_r^2 + t_j^2 + t_l^2$, where t_r is the rise time, t_j is the transit time spread (TTS), and t_l is the integration constant of the RC circuit. The PMT signal model was developed by Yingtao Chen, who was working on the ASIC-based electronics for WFCTA [48]. The advantage of this model is the combination of PMT parameters and the single p.e. response spectrum by using a simple equation. In the current version, we set the four parameters of this model corresponding to the previous baseline PMT of WFCTA, Hamamatsu R1924A. Note that, currently, the SiPMs are planned to be used in the camera. By changing the parameters, this signal model can be made to fit the new photodetectors used in the telescope.

The time window with the PMT response is then passed to the shaping process, which is programmed to simulate front-end electronics. The whole module of front-end electronics is treated as a digital filter. The signal shaping process is simulated with the corresponding transfer function of this filter given by:

$$H(z) = \frac{Y(z)}{X(z)} = \frac{\sum_{k=0}^{M} b_k z^{-k}}{1 - \sum_{k=1}^{N} a_k z_{-k}} \tag{7.4}$$

where $Y(z)$ and $X(z)$ are output and input signals, respectively. b_k and a_k are the filter coefficients. This transfer function is expressed by using the z-transform, which is generally applied in discrete-time systems. The z is in a function of the s parameter in Laplace transform, $z = e^{sT}$, where T is the sampling period. The final coefficients can be set based on the test results with the prototype. By varying the filter coefficients, we can easily simulate the electronic module. A typical single p.e. response and the shaped signal in the time window are shown in Figure 7.5.

- **ADVANCED mode**
  In the advanced mode, additional physical information, including the number of photons arriving at each pixel, the mean arrival time of photons, the RMS of photon arrival times, and the leaked photon in each photodetector, are stored for further analysis.

For the trigger of each pixel, Three trigger modes (*Integral*, *Height*, and *WINSUM*) are programmed in the code for different electronic designs. For all trigger modes, a logic value "0" will be returned and stored if the signal in the time window doesn't match the trigger condition. In the *Height* and the *Integral* trigger modes, the signal height (signal peak) and

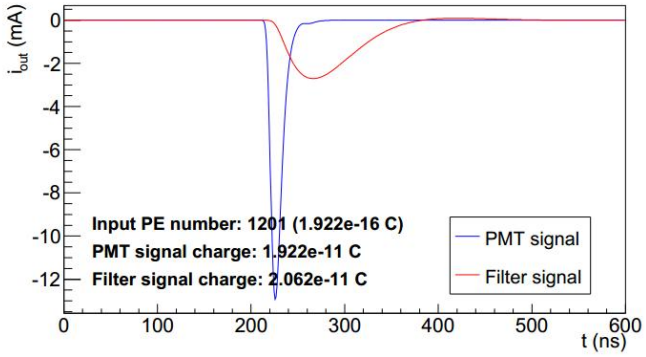

Figure 7.5 – A typical PMT signal of the Cherenkov light and the corresponding signal shaped by a 2-order low-pass filter.

the integral of the signal are compared to the threshold defined by users, respectively. The *WINSUM* mode is based on a sliding window average calculation. In this mode, the signal of each 20 ns is summed up as one bin, the integral of each 4 bins will be used for the trigger determination. If it's larger than the given threshold value, the signal will be triggered. This mode corresponds to the current design. After signal processing and trigger determination of each pixel, the image in the camera can be finally obtained. In a further step, the image will be used for telescope trigger and multiple image analysis.

Trigger of the Cherenkov image

Cherenkov events for WFCTA can be triggered with the individual image in a single telescope or the combined images from multiple telescopes. The candidate images will be compared to the predefined patterns shown in Figure 7.6. An agreement between a certain area of the image and the pattern will make the event triggered in "NewTel".

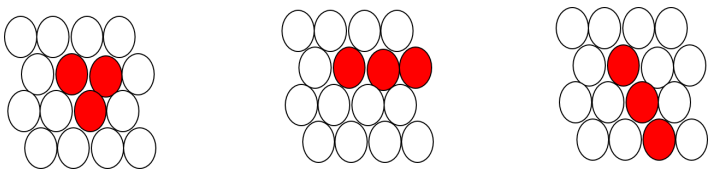

Figure 7.6 – Predefined patterns for trigger of Cherenkov events

The code of "NewTel" v1.0 was released for the collaboration in 2016 and has been integrated into the software framework of LHAASO. Currently, the code is being updated following the changes of hardware modules.

7.4 Image parameterization and event reconstruction

7.4.1 Image of Cherenkov light in WFCTA telescopes

The WFCTA telescopes are active calorimeters for the showers. A typical response of the WFCTA telescopes to a shower event is shown in Figure 7.7. The classic "Hillas parameters" [204], which has been widely employed in the experiments with Cherenkov telescopes, are used to describe the image. The Hillas parameterization, which attributes the shower image in the camera to an approximate elliptical shape, has the advantage of summarizing the signals from a large number of pixels to a group of quantities corresponding to the shower energy and the shower geometry.

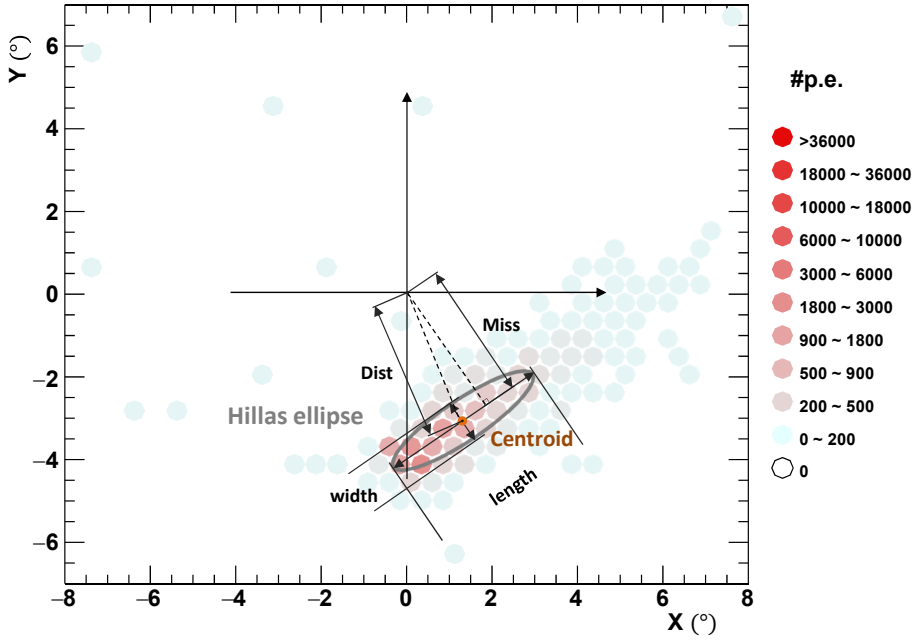

Figure 7.7 – WFCTA image and Hillas parameterization

The optical system of the WFCTA telescope is sensitive to the NSB noise and the changes of atmospheric transmittance due to the weather condition. In order to obtain precise parameters and to reject the NSB signals, each image is first cleaned by removing the pixels that meet the following conditions:

- Pixels with the charge of the signal below 10 p.e. are removed.
- Pixels with less than one neighbor are removed.

With the cleaned image, the following image parameters, which are meaningful for event reconstruction, can be deduced:

- $SIZE$: The integrated p.e number of the image.
- $Width$, $Length$: The parameters indicate the geometric dimensions of the ellipse.
- $Dist$, The distance from the centroid of the image to the camera center.
- $Miss$, The distance from the camera center to the long axis of the ellipse.
- δ, The angle between the major axis of the ellipse and the Y-axis of the camera.

The $SIZE$ is a crucial parameter correlated to the energy and the core distance from the telescope. The other parameters such as $Width$, $Length$, $Dist$, $Miss$, and δ are correlated to the shower geometry and to the longitudinal development of the shower (See Figure 7.7).

As the WFCTA telescopes are located at almost the same position and pointing to different directions in order to cover a large FoV, the nowadays conventional stereoscopic parameterization with multiple telescopes, which used in the γ-astronomy experiments, is inappropriate for event reconstruction with WFCTA. However, the WCDA shower-core detector can offer an accurate measurement for the shower cores (~2.5 m) and arrival directions (~0.3°). Therefore, the shower energy can be determined by combining the core position measured by the WCDA and the image parameters from WFCTA. This part will be presented in the following subsection.

7.4.2 Event reconstruction of the EAS

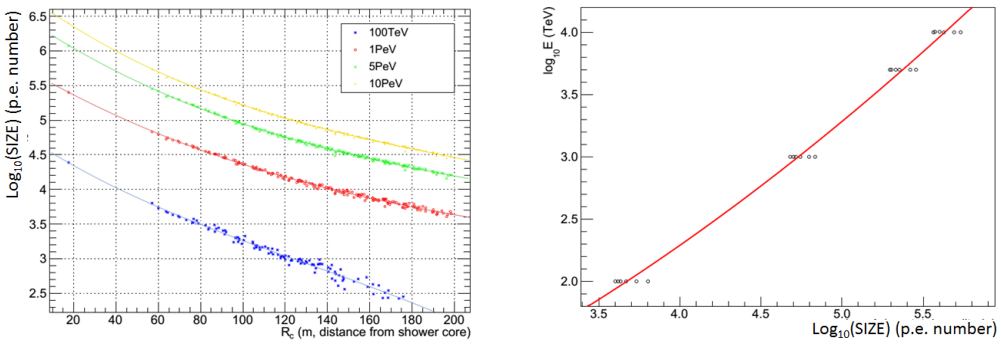

Figure 7.8 – *Left:* $log_{10}SIZE$ as a function of R_p (the distance from the telescope to the shower axis) for showers with various primary energies from 100 TeV to 10 PeV.
Right: Correlation between $log_{10}E$ and $log_{10}SIZE$ for R_p value from 60 to 70 m.

The majority of the Cherenkov light is emitted near the X_{max} of the shower, therefore, the $SIZE$ (total signal integral) value has a strong correlation to the N_{max}, which is proportional to the primary energy of the shower. Figure 7.8-left shows the lateral distribution of $SIZE$

from the simulation data for four showers with various primary energies of 100 TeV, 1 PeV, 5 PeV, and 10 PeV, respectively. In Figure 7.8-left, we can see that, the $SIZE$ value decreases with increasing R_p, for the shower with a fixed energy. For a fixed R_p value, $SIZE$ increases with the shower energy. Figure 7.8-right shows the correlation between $SIZE$ and the shower energy, E, for a fixed R_p range (60 to 70 m). $log_{10}\ E$ can be approximately described with a quadratic polynomial function of $log_{10}\ SIZE$.

To test the ability of WFCTA for event reconstruction, a two-step simulation of air showers and detector response in WFCTA is performed. For the first step, a shower library is simulated by the WFCTA team in IHEP with the CORSIKA package [205]. The parameters of this shower library in CORSIKA simulation are set as the following:

- Energy range: 100 TeV to 1 PeV.
- Power law index of the energy spectrum: -2.3.
- Zenith(θ): uniformly distributed from 22° to 38°.
- Azimuth (φ): uniformly distributed from 77° to 103°.
- Observatory level: 4400 m a.s.l, which is the altitude of the LHAASO site.
- Geomagnetic field: (B_{north}, B_{west}) = (34.845, 35.396) μT, where B_{north} is the positive X-axis pointing to the north and B_{west} is the positive Y-axis to the west. This data was the measured near the Observatory.

For the second step, one WFCTA telescope, pointing to $(\theta, \varphi) = (30°, 90°)$ is employed to work together with WCDA core detector. The range of zenith and azimuth angles can cover the FoV of this telescope. The shower events triggered by both the WCDA-core detector array and the WFCTA telescope are selected for further analysis.

According to the simulation data, the shower energy can be reconstructed with a function of the image parameters and R_p, as described in Equation 7.5.

$$log_{10}\ E_{rec} = f_1(log_{10}\ SIZE, R_p) + f_2(Dist, \delta) \tag{7.5}$$

This function is composed of energy-related and direction-related terms. The energy-related term, consisting of $log_{10}\ SIZE$ and R_p, plays the main role in the determination of E, while the direction-related term, consisting of $Dist$ and δ, gives the correction based on the detected shower geometry. Figure 7.9 shows the correlations between the energy-related term (f_1) and the primary energy of the shower over the energy range of 100 TeV to 1 PeV.

In order to compare the differences between the reconstructed energy, E_{rec}, with Equation 7.5 and the primary energy of the shower, E, the histogram of $\Delta E/E$ for all triggered

events is shown in Figure 7.10-left. The resolution of energy reconstruction is around 20% over the energy range from 100 TeV to 10 PeV.

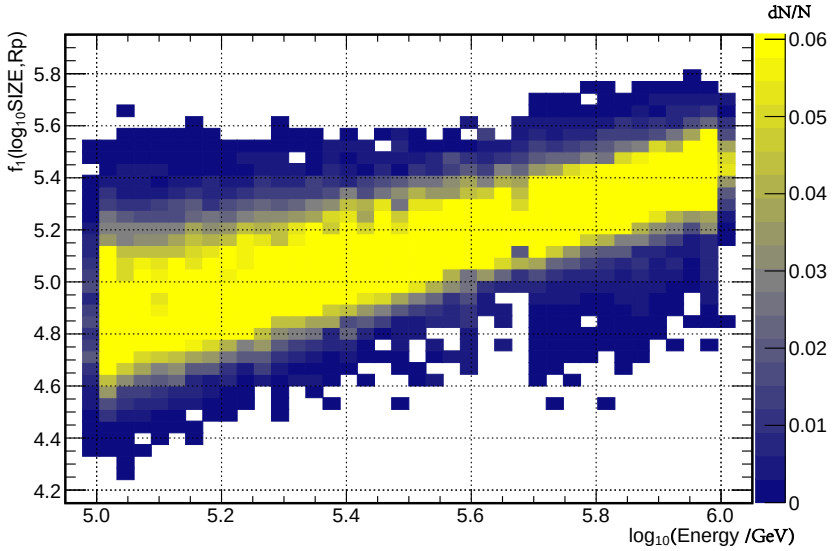

Figure 7.9 – Correlation of the energy-related term in Equation 7.5 and the primary energy of a shower event.

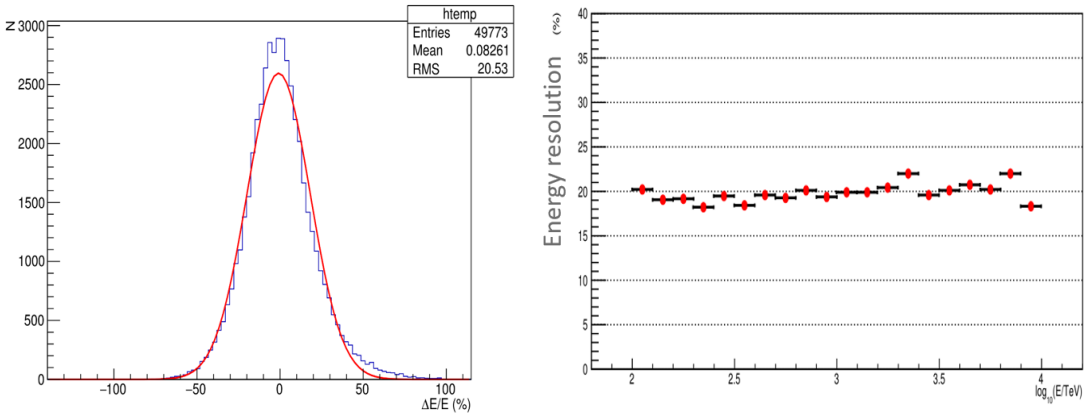

Figure 7.10 – *Left:* The distribution of $\Delta E/E$ for all triggered events.
Right: Energy resolution over the energy range from 100 TeV to 10 PeV

7.5 Hybrid detection of cosmic rays with LHAASO

7.5.1 LHAASO hybrid detectors

LHAASO proposes to measure the energy spectrum and identify the mass composition of cosmic rays around the “knee” region. The scheme of LHAASO Hybrid detectors is shown

in Figure 7.11. In the EAS detection, WCDA, KM2A-MD, and WFCTA can be combined together for hybrid measurements, yielding a precise reconstruction of the shower parameters. The detector layout of the Observatory and the characteristics of each detector array are introduced in section 6.2.

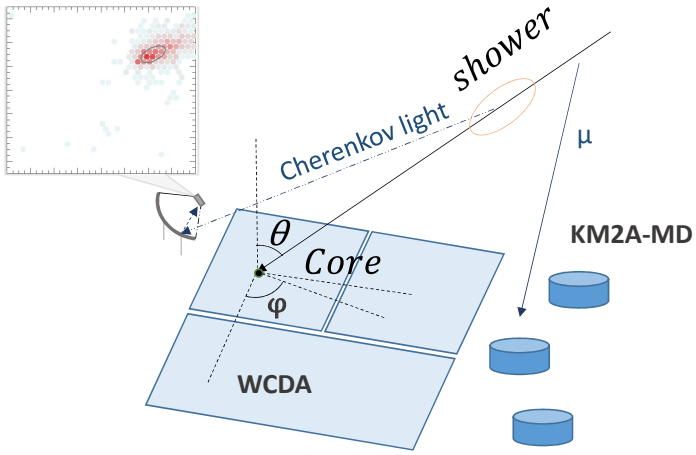

Figure 7.11 – Hybrid detection of the EAS at the LHAASO Observatory

The simulation of each LHAASO detector array has been developed [181, 206, 207]. Various parameters, correlated to the shower properties such as the primary energy, arrival direction, and primary particle, can be determined from the simulated data. Based on the shower library introduced in subsection 7.4.2, which consists of five mass groups for the cosmic rays: p, He, CNO, MgAlSi and Iron, the responses of the three detector arrays for each shower event are simulated. Since the WFCTA image was previously introduced in subsection 7.4.1, in this section, only the parameterization of data that will be measured by WCDA and KM2A-MD will be presented. Furthermore, the tuned parameters, that will be used for primary particle identification, are introduced.

7.5.2 Parameterization of the WCDA data

Figure 7.12 shows the signals in p.e. numbers measured in each cell of the WCDA for a shower event. The core position and the arrival direction of the shower can be obtained with a precision of ~2.5 m by fitting the hump in the S_{WCDA} data. Figure 7.12 shows the lateral distribution of S_{WCDA} (binned in each 5 m). By fitting the lateral distribution of S_{WCDA} with a NKG-type function (Equation 7.6), the reference parameter of WCDA signals, S_{ref}, can be obtained to describe the shower size. In Equation 7.6, R_{ref} is set to 700 m and β and γ are

variables related to the shower geometry and shower size.

$$S(r) = S_{ref} \cdot \left(\frac{r}{R_{ref}}\right)^{\beta} \left(1 + \frac{r}{R_{ref}}\right)^{\beta+\gamma} \tag{7.6}$$

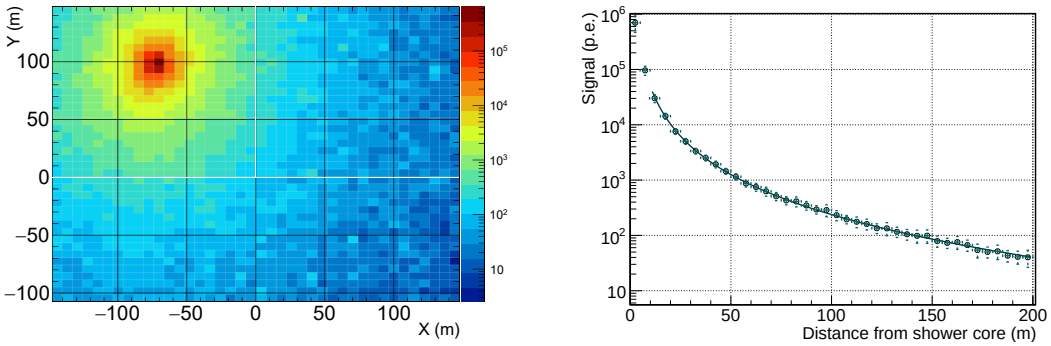

Figure 7.12 – *Left:* 2-D distribution of S_{WCDA} from each detector cell in the number of photoelectrons. *Right:* Lateral distribution of a given shower measured by the WCDA.

7.5.3 Parameterization of the KM2A-MD data

The muon detector (MD) of the KM2A consists of water Cherenkov detectors, which were previously introduced in subsection 6.2.1. The 2.5 m-thick soil layer above the detectors provides a shielding against the low-energy electromagnetic components of the air showers. Therefore, the response of the MDs in EAS detection is mostly induced by the muon component. This is of high importance for determining the primary mass of the EAS.

The complete information of the KM2A simulation is introduced in ref. [206]. The number of muons, n_μ, measured in each MD for a certain event is available for further analysis. Figure 7.13-left shows the distribution of n_μ for a given shower. The n_μ (binned over 50 m) with respect to the core distance is shown in Figure 7.13-right. Similarly to the S_{WCDA}, a reference of muon number, n_μ^{ref} can be obtained by fitting the n_μ with a lateral distribution function of a muonic shower (Equation 7.7) [208], where R_{ref} is set to 400 m and η depends on the zenith angle and the primary energy of the shower.

$$n_\mu(r) = n_\mu^{ref} \cdot \left(\frac{r}{R_{ref}}\right)^{-\frac{3}{4}} \left(\frac{r + 320}{R_{ref} + 320}\right)^{-\eta} \tag{7.7}$$

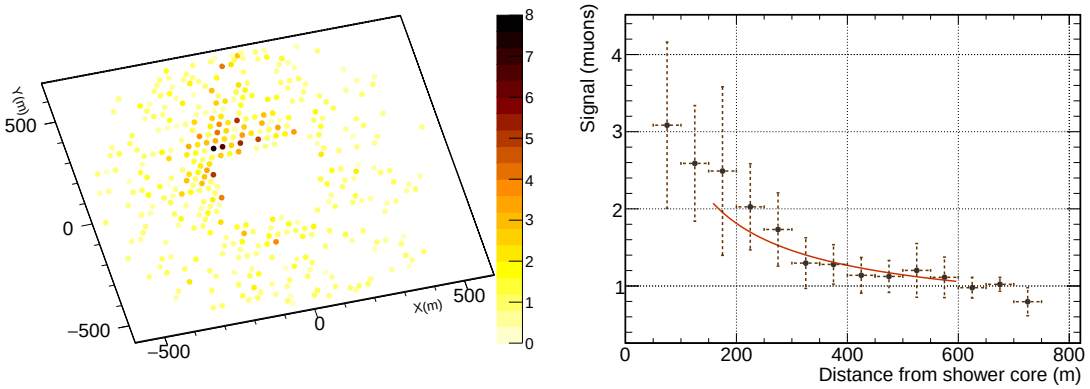

Figure 7.13 – *Left:* 2-D distribution of muon numbers measured by KM2A-MD. *Right:* Lateral distribution of muon shower measured by KM2A-MD.

7.6 Particle identification with the MVA method

7.6.1 Multi-variate analysis method and TMVA

Machine learning is an important area of big-data analysis. It has been developed in terms of algorithms, theory, and applications for several decades. For a machine learning algorithm, there are various ways to model the target problem by interacting with the accumulated experience or the input data. In the development of machine learning, each algorithm usually adopts one of the popular learning styles that suits the type of the target problem. The learning styles, also called "learning models", can be mainly grouped into three categories: "unsupervised learning", "supervised learning", and "semi-supervised learning", which are introduced as the following:

- **Unsupervised learning**

  Unsupervised learning algorithms usually work with the input data, which is not labeled and have unknown results. Therefore, the learning model of the algorithm has to be prepared by first deducing the structure of the data. Then, some general rules can be extracted based on the features of the data structure. Mathematical processes are generally implemented to the data samples for globally reducing the redundancies or organizing the entries of the data following their similarities. The typical example algorithms adopting the unsupervised learning style are the apriori algorithm, k-mean algorithm, etc..

- **Supervised learning**

  The input data for training the supervised learning models is always labeled or has exact results. During the algorithm training, supervised learning models are required to make

and to optimize their predictions for all samples according to the known results until the desired or the best accuracy is achieved. The target problems for supervised learning algorithms are mainly the classifications and the regressions for big data. Typical example algorithms include analytical learning, artificial neural network, decision tree learning, etc..

- **Semi-supervised learning**
  Semi-supervised learning models are designed to deal with the input data containing mixed labeled and unlabeled entries. Combining the methods used in both unsupervised and supervised learning algorithms, the way that semi-supervised learning models work is performed by both learning the data structures and generally making predictions based on smoothness, cluster, or manifold assumptions for unlabeled entries. Therefore, semi-supervised learning algorithms can be realized either as extensions of supervised or unsupervised learning models.

As an extension of the computer science, the multivariate methods for the data analysis based on these algorithms, especially the supervised learning models, have significantly evolved in the recent years. They have become a potential classification tool for most data analyses in the high-energy physics and astro-particle experiments.

Although the MVA methods are effective and have many advantages in data mining and process compared to traditional analysis method. They still have a potential issue of overfitting or called overtraining, which can lead to an illusion for us that the model or algorithm has a perfect performance. From the statistical point of view, the overfitting (or overtraining) phenomenon occurs when a model is extremely complex to describe the data in the only sample and lose the generalization to adapt to other data of similar types. It always happens when too many parameters are used to describe the data. Avoiding overfitting is a crucial work in the data modeling and the training of machine learning algorithms to ensure the results of the analysis reliable.

The Toolkit for Multivariate Analysis (TMVA) [209] is a code package for the processing, parallel evaluation, and application of multivariate classification integrated in ROOT-CERN [160]. The TMVA package contains many MVA sub-routines corresponding to different types of "supervised learning" algorithms. The MVA sub-routines are managed by a "TMVA::Factory" for the algorithm training with part of all event samples to generate the mapping relationships or the logic models for the classification. Then the trained sub-routines can be applied to classify all events in the data collection.

In order to foresee the performances of different MVA algorithms for the classification of cosmic-ray primary mass compositions with LHAASO, a group of MVA classifiers, integrated

in the TMVA package, has been tested based on the simulation data of the LHAASO hybrid detectors. The related contents concerning the comparison and the application of the MVA methods are discussed in the next subsections.

7.6.2 Parameters for particle identification

In order to increase the computational efficiency for particle identification and to simplify the multidimensional data modeling, a tuning of parameters is implemented. The tuning of parameters is based on two principles:

- The tuned parameter should be in a linear correlation with $log_{10}\ E$ or $log_{10}\ X_{max}$.
- In the optimization of the parameter, the candidate forms of the parameter are tested with the variable ranking process integrated in the data preparation of each algorithm of TMVA. The separation index of each parameter will be returned and is considered as an important factor for the tuning.

Four parameters, P_{lat}, P_{μ}, P_E, and P_{long}, are finally used as input parameters for the MVA classifiers (see Equation 7.8, Equation 7.9, Equation 7.10, Equation 7.11).

P_{lat} is expressed as Equation 7.8,

$$P_{lat} = log_{10}\left(\frac{S_{max}}{S_{ref}}\right) \tag{7.8}$$

where S_{max} is the maximum signal among WCDA cells and S_{ref} is the shower size measured by WCDA. This parameter is strongly correlated to the residual energy of the shower at the ground level and the X_{max} of the shower (see Figure 7.14-left).

The expression of P_{μ} is given by Equation 7.9

$$P_{\mu} = log_{10}(\ N_{\mu} + n_{\mu}^{ref}\ ) + log_{10}(\ N_{MD} \cdot n_{\mu}^{ref} + n_{\mu}^{ref}\ ) \tag{7.9}$$

where N_{μ} is the total muon number measured by the MDs located in the range of core distance from 150 m to 600 m. As the shower core is measured by the WCDA core detector, a fair proportion of muons arriving at the area close to the core can not be measured by the MDs due to the layout of KM2A. Therefore, the MDs near the shower core (<150 m) are removed from the counting of total muon number to unify the rule of parameterization and to reduce the bias induced by the detector layout. The upper limit is set to 600 m to reduce the bias due to the incomplete counting for the muons arriving at the edge of KM2A. n_{μ}^{ref} is the fitted parameter from Equation 7.7 and N_{MD} is the number of triggered MDs for a given shower. P_{μ} is strongly related to primary energy, E of the showers (see Figure 7.14-right) and is a crucial

parameter for particle identification, as the produced muons in the EAS are only affected by the ionization when propagating in the atmosphere and basically arrive at the ground with a very small degradation of energy.

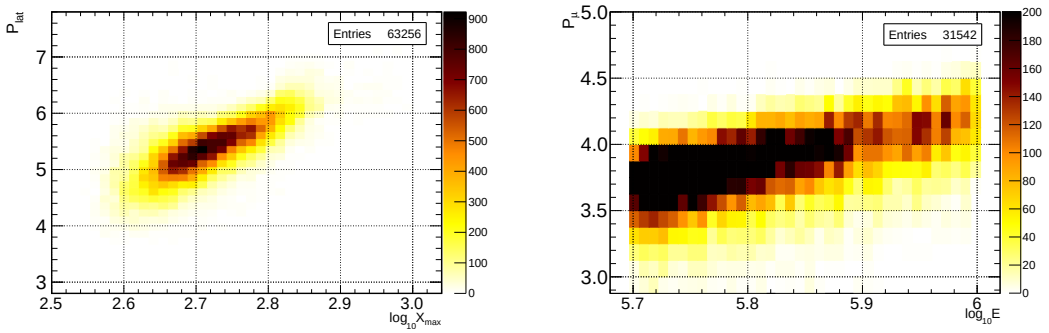

Figure 7.14 – Left: Correlation between P_{lat} and $log_{10}X_{max}$, Right: Correlation between P_{μ} and $log_{10}E$.

P_E is expressed as a logarithmic function of $SIZE$ corrected by R_p and given by Equation 7.10,

$$P_E = log_{10}(SIZE) + 0.0084 \cdot R_p \tag{7.10}$$

where R_p is the distance from the telescope to the shower axis. P_E is the main parameter correlated to the energy of the shower.

The expression of P_{long} is given by Equation 7.11,

$$P_{long} = \frac{Width}{Length + Dist + Miss} - 0.003 \cdot R_p \tag{7.11}$$

which is composed of the geometry-related parameters ($Width$, $Length$, $Dist$, and $Miss$) from the WFCTA image and also corrected by R_p. P_{long} is correlated to the X_{max} of the shower.

Figure 7.15 shows the distribution of these four input parameters for all the selected shower samples initiated by different mass compositions of cosmic rays.

7.6.3 MVA classifier comparison of the LHAASO simulation data

The MVA algorithms are often grouped based on the kernel technique that they use. There are more than ten groups of popular algorithms included in the TMVA for the classification. Compared to traditional cut-based analysis techniques such as likelihood classification, Fisher discriminants, etc., MVA methods such as support vector machines (SVM), neural networks (NNs), and boosted decision trees (BDT) have several advantages. Their main strength is the consideration of non-linear correlations between input parameters. Therefore, each group of

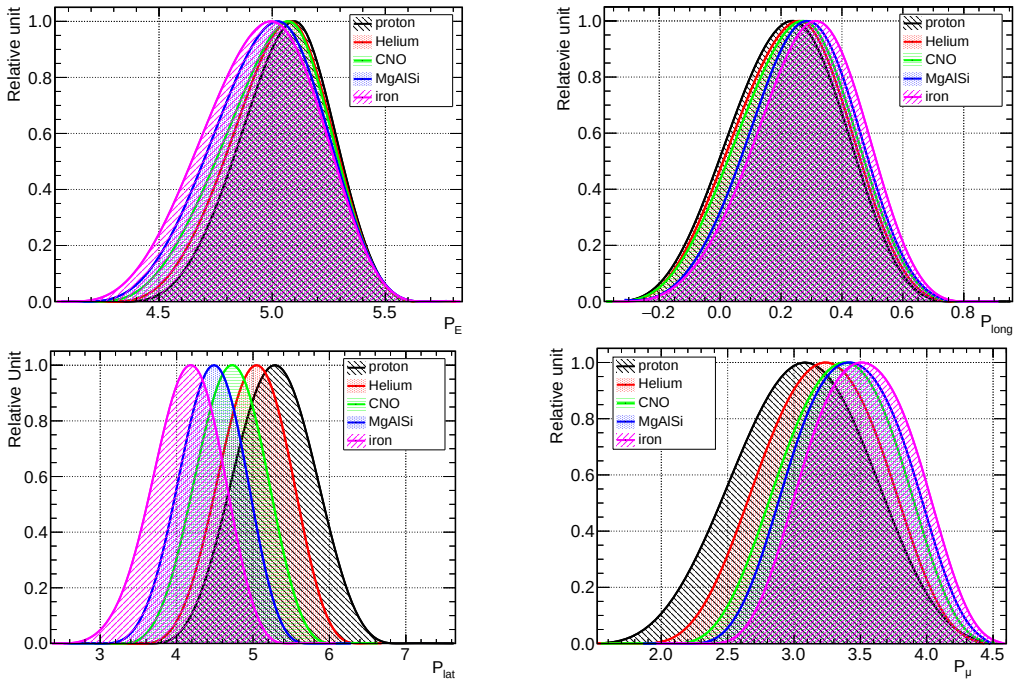

Figure 7.15 – Parameter distributions for different mass compositions

algorithms can be categorized as linear or non-linear classifiers in terms of how they work with the data. In order to survey the performances of the MVA classifiers, typical algorithms belonging to each group are selected to be tested with the simulation data of the LHAASO hybrid detection. The tested algorithms are listed below:

- Linear classifiers: Optimized cuts with principal component analysis (CutsPCA), projective likelihood estimator with PCA-transformed input variables (LikelihoodPCA), multi-variate probability density estimator based on range-searching (PDERS), and linear discriminant analysis (LD).

- Non-linear classifiers: Neural networks of multilayer perceptrons (MLP), Clermont-Ferrand neural network (CFMlpANN), boosted decision trees (BDT), and boosted decision trees with gradient boosting (BDTG).

These algorithms are mostly recommended by default in the templates of the TMVA classification scripts, Friedman-Popescu's RuleFit method (RuleFit) is ignored in the tests as it can be regarded as an advanced extension of cuts algorithms. The Fisher algorithms are also neglected since they are working similarly to the LD algorithms. The SVM is not selected for the test since the support vectors are solved by means of quadratic programming in the calculation, therefore, this algorithm is difficult to be implemented for large-scale training samples.

Aiming at comprehensively understanding the performance of each classifier for the particle identification and investigate the effect of the fit and the tuning of "measured" quantities, the selected algorithms are tested, with raw inputs and tuned parameters from the simulation data, respectively. The two groups of parameters are listed below and previously introduced in section 7.4, section 7.5, and this section:

- Raw inputs: $SIZE$, $Width$, $Dist$, $Length$, R_p, S_{max} and N_μ.
- Tuned parameters: P_{lat}, P_μ, P_E, and P_{long}.

The tests are performed for three separations of the mass compositions, respectively: $Iron/proton$, $Helium/proton$, and $Iron+MgAlSi+CNO/Helium+proton$ ($Heavy\ nuclide/p+He$). All the algorithms in the tests are run with the default configurations defined by TMVA. The tested results of the classifiers are discussed in two aspects, which are introduced below:

- **Signal efficiency (η_s) versus background rejection (η_{1-b})**
  The main indicators of the classifier performances are the signal efficiency (η_s) and the background rejection (η_{1-b}) for a certain separation. Figure 7.16, Figure 7.19, and Figure 7.22 show the plots of η_s versus η_{1-b} for the three separations, respectively. The η_s vs. η_{1-b} curves are generally in an arched shape and spread toward the extreme end of (η_s, η_{1-b}) = (100%,100%) corresponding to the ideal and perfect separation.

- **Responses of the concerned classifiers**
  Besides the result of η_s vs. η_{1-b}, the response (or called "output") of each classifier for different compositions is also crucial for evaluating the performance of the classifier. MLP and BDT are typical representatives of NNs and decision-tree-based algorithms. They are both potential candidates for this work. The responses tested with tuned parameters for the three separations of the two classifiers are shown and discussed in the following parts of this subsection (see Figure 7.17, Figure 7.18, Figure 7.20, Figure 7.21, Figure 7.23, and Figure 7.24). The analysis concerning the signal efficiency (η_s), the background efficiency(η_b), and the significance ($S/\sqrt{S+B}$) for each separation is also shown together with the classifier response. These plots are drawn with the "TMVAGui" based on the training and the test data.

The separation of $Iron$ and $proton$ initiated shower events

The η_s versus η_{1-b} curves of the tested classifiers for the $Iron/proton$ separation are shown in Figure 7.16. For the separation tested with raw inputs (see Figure 7.16(a)), η_s values of most classifiers remain above 95%, while the corresponding η_{1-b} values are above 95%. Slight

difference between the performances of linear and non-linear classifiers can be seen in the plot as expected. The η_s vs. η_{1-b} curves yielded by the CutsPCA classifier are irregular due to the difficulty to apply a simple cut to the multidimensional input data. For the separation with tuned parameters shown in Figure 7.16(b), η_s vs. η_{1-b} curves of non-linear classifiers have similar tendencies compared to those with raw inputs. The performances of linear classifiers get improved and approach the non-linear ones. This can be understood as the tuning of the input quantities reduces the complexity of the database, therefore, leading to a better separation with the linear classifiers.

The responses of the MLP and BDT classifiers are shown in 7.17(a) and 7.18(a), respectively. For the $Iron/proton$ separation, MLP and BDT have similar performances and both offer almost perfect separations. The optimal cut value is suggested to be 0.53 for MLP and 0.00 for BDT based on the analysis of the signal significance (see 7.17(b), 7.18(b)). It is 0.53 for MLP and The signal significance highly depends on the relative ratio of the signal ($Iron$) and background ($proton$) event numbers. Here their event numbers are kept as 1000:1000, which is the default ratio set by the TMVA to evaluate the classifier performances.

The separation of $Helium$ and $proton$ initiated shower events

The properties of air showers initiated by $Helium$ and $proton$ have very little differences and are, therefore, difficult to be identified. The η_s vs. η_{1-b} curves of all tested classifiers for the $Helium/proton$ separation approach the limits at $(\eta_s, \eta_{1-b}) \simeq (75\%,75\%)$ with raw inputs (see 7.19(a)) and at $(\eta_s, \eta_{1-b}) = (\sim 68\%,\sim 68\%)$ with tuned parameters (see 7.19(b)).

The $Helium/proton$ separations by both MLP and BDT have large areas of overlap (see 7.23(a) and 7.24(a)). This makes poor $S/\sqrt{S+B}$ values even for the optimal cuts. The performances of the two classifiers are not out of expectation and can be used to estimate the statistical limit of the data from the LHAASO hybrid detectors for the $Helium/proton$ separation.

The separation of $Heavy\,nuclide/p+He$ initiated shower events

Previous tests with $Iron/proton$ and $Helium/proton$ separations can be realized to probe the classifier performances under extreme conditions. In the practical measurements of the cosmic rays at the LHAASO observatory, air showers induced by many mass compositions will arrive arbitrarily at the ground. The classification for heavy and light nuclide with the simulated data of the five compositions is tested in order to foresee the performances of the classifiers in an "open" cosmic-ray observation. The relative ratio of the five compositions are set to

$$N_{proton} : N_{Helium} : N_{CNO} : N_{MgAlSi} : N_{Iron} = 1 : 1 : 1 : 1 : 1.$$

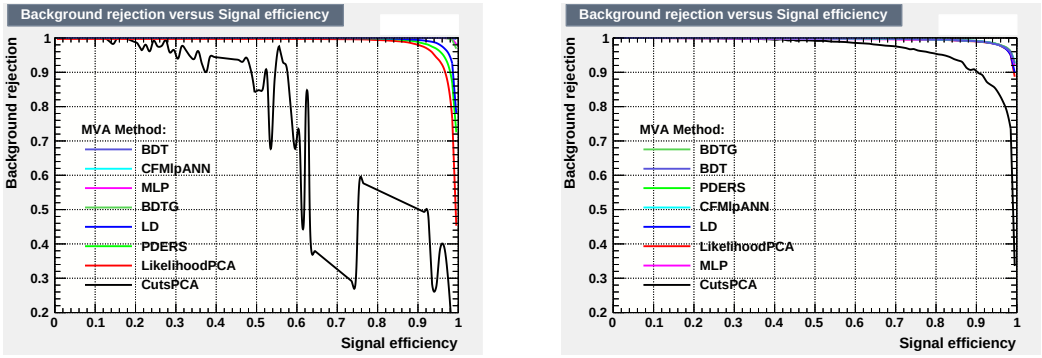

(a) (b)

Figure 7.16 – η_s vs η_{1-b} of the classifiers for the *Iron/proton* separation with raw inputs (7.16(a)) and tuned parameters (7.16(b)), respectively. In 7.16(b), the η_s vs η_{1-b} curves of most classifiers (except CutsPCA) are superposed since they have similar performance.

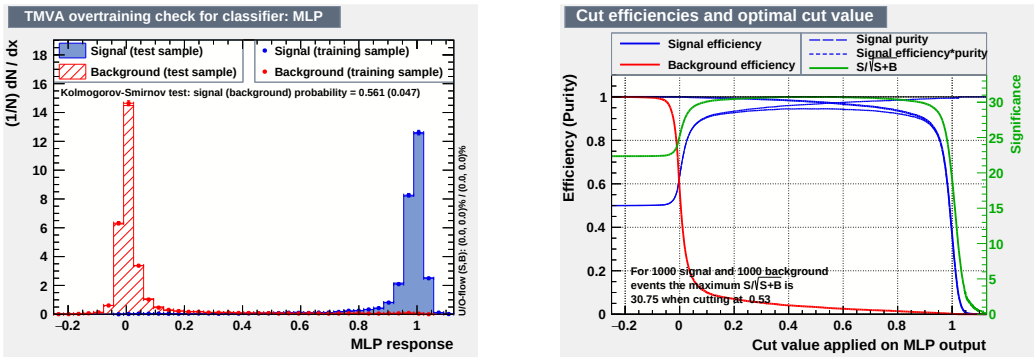

(a) (b)

Figure 7.17 – 7.17(a): Response of the MLP classifier for the *Iron/proton* separation. 7.17(b): η_s (blue), η_b (red) and $S/\sqrt{S+B}$ (green) over the range of classifier response.

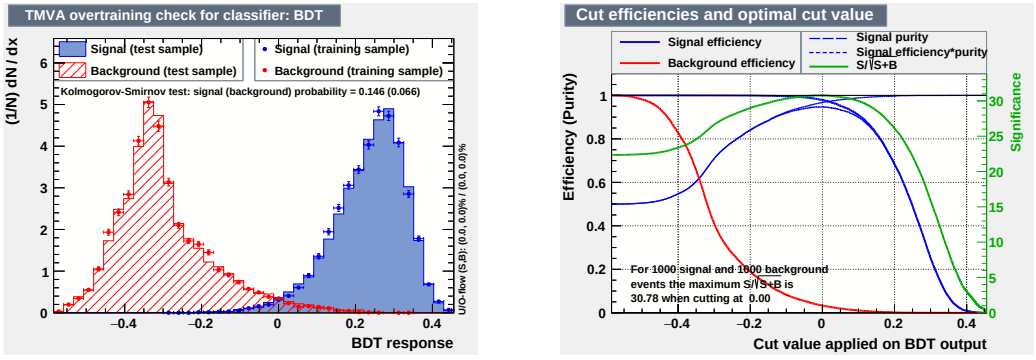

(a) (b)

Figure 7.18 – 7.18(a): Response of the BDT classifier for the *Iron/proton* separation. 7.18(b): η_s (blue), η_b (red) and $S/\sqrt{S+B}$ (green) over the range of classifier response.

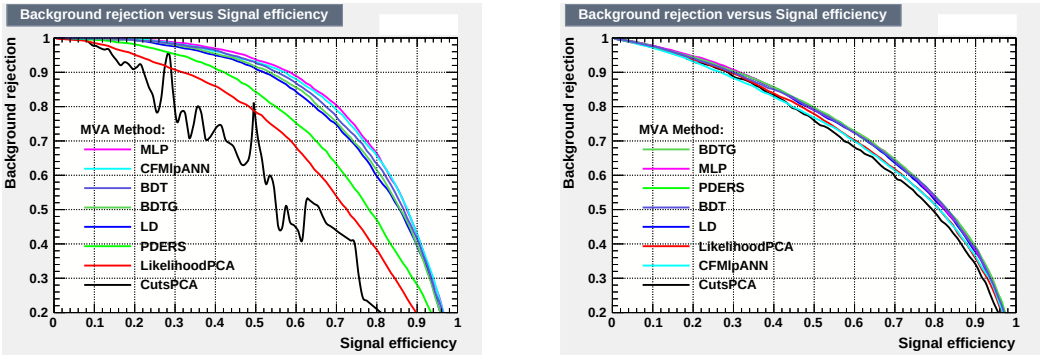

(a) (b)

Figure 7.19 – η_s vs η_{1-b} of the classifiers for the *Helium/proton* separation with raw inputs (7.19(a)) and tuned parameters (7.19(b)), respectively.

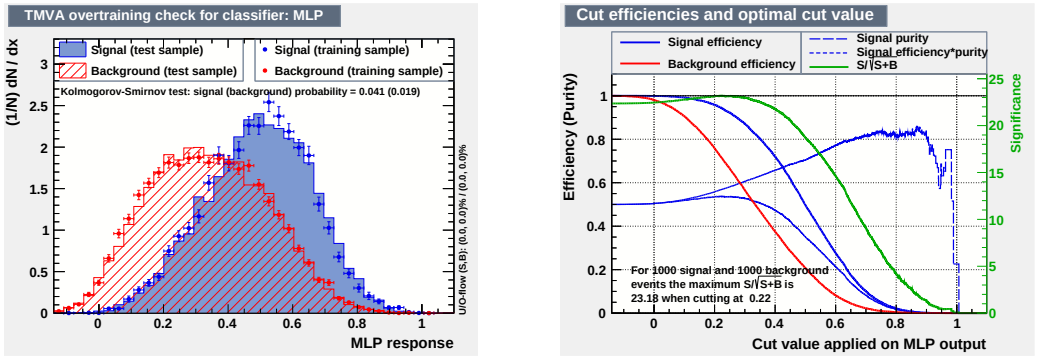

(a) (b)

Figure 7.20 – 7.20(a): Response of the MLP classifer for the *Helium/proton* separation. 7.20(b): η_s (blue), η_b (red) and $S/\sqrt{S+B}$ (green) over the range of classifier response.

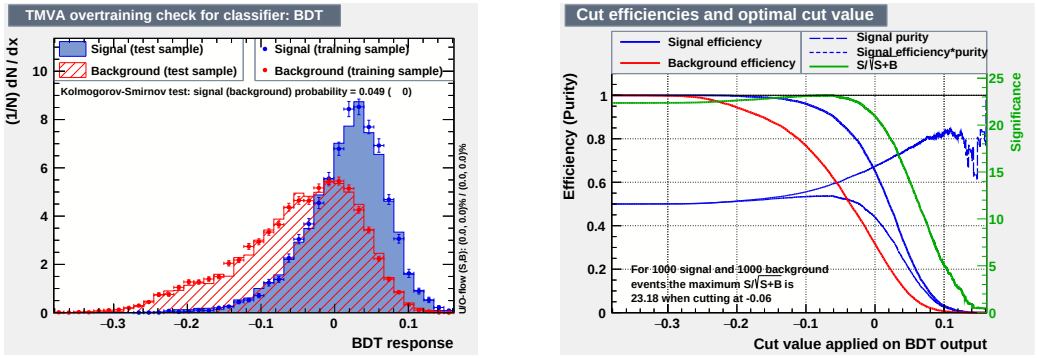

(a) (b)

Figure 7.21 – 7.21(a): Response of the BDT classifier for the *Helium/proton* separation. 7.21(b): η_s (blue), η_b (red) and $S/\sqrt{S+B}$ (green) over the range of classifier response.

The results of η_s vs. η_{1-b} for the $Heavy\,nuclide/p + He$ separation are shown in Figure 7.22. Linear classifiers have good performances of (η_s, η_{1-b}) $\simeq$ (85%,85%) for tests with both raw inputs (see 7.22(a)) and tuned parameters (see 7.22(b)). However, the non-linear classifiers perform differently for the two cases. Their η_s vs. η_{1-b} curves get over the limit of (η_s, η_{1-b}) = (92%,92%) when working with raw inputs, and degrade down to (η_s, η_{1-b}) $\simeq$ (85%,85%), which are comparable to the ones of linear classifiers, when working with tuned parameters.

The MLP and BDT responses for the $Heavy\,nuclide/p + He$ separation with tuned parameters are shown in 7.23(a) and 7.24(a), respectively. The $Signal$ (Heavy nuclide) and $Background$ (p+He) are clearly separated by both classifiers, and the maximum values of signal significance are appreciable for further applications (see 7.23(b) and 7.24(b)).

Discussion of the classifier comparison

The linear classifiers are considered to be simple, robust and easy to train for most target problems. They are also efficient in algorithm training. However, the disadvantages of linear models make them limited when dealing with the data having complex structures. From the results that were presented above, it can be concluded that non-linear classifiers always have better performances in this work, as expected. The results obtained with the tuned parameters are relatively worse than those with raw inputs for the non-linear classifiers. This can be explained since the tuning of parameters dwarfs the characteristics of the input quantities for each composition in the database, at the same time as makes a simpler data structure. The tuned parameters are chosen for further applications in this work to avoid overtraining and to be conservative.

The NNs and the BDT algorithms have both good performances in particle separation. After a comparison in terms of the training time, the performance over the whole energy range, and the adaptability for further improvement, the method of Boost Decision Trees with Gradient boosting (BDTG), which is an extension of the BDT algorithm, is selected to be employed for the particle identification with the LHAASO simulation data.

7.6.4 Training and application of the BDTG classifier

Training of BDTG

Decision trees have a structure of nodes, which determine the response to a given event based on the logic that is built up during the algorithm training. In the classification, a set of parameters for a given event is sent to each node for a binary decision, until the final decision

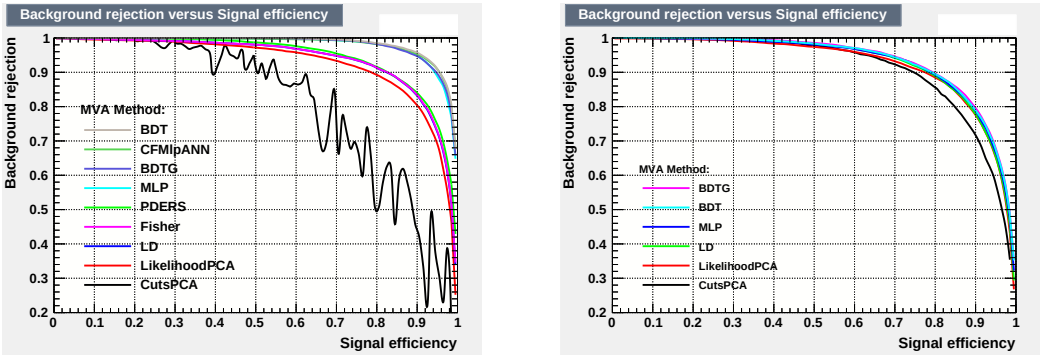

(a) (b)

Figure 7.22 – η_s vs η_{1-b} of the classifiers for the $Heavy\,nuclide/p+He$ separation with raw inputs (7.19(a)) and tuned parameters (7.22(b)), respectively.

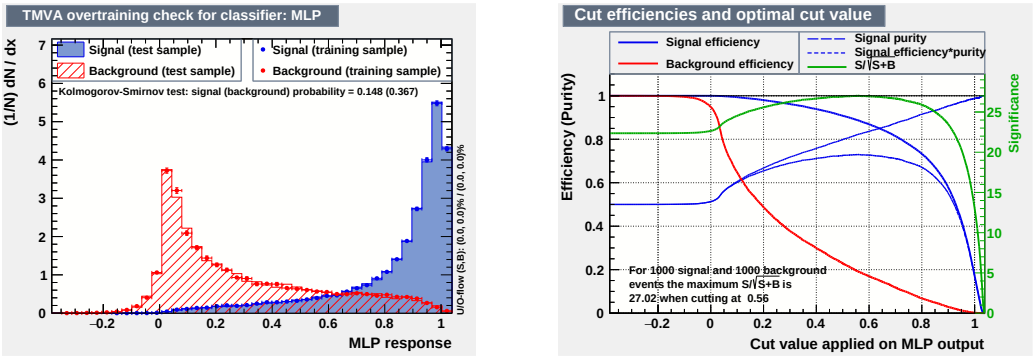

(a) (b)

Figure 7.23 – 7.23(a): Response of the MLP classifer for the $Heavy\,nuclide/p+He$ separation. 7.23(b): η_s (blue), η_b (red) and $S/\sqrt{S+B}$ (green) over the range of classifier response.

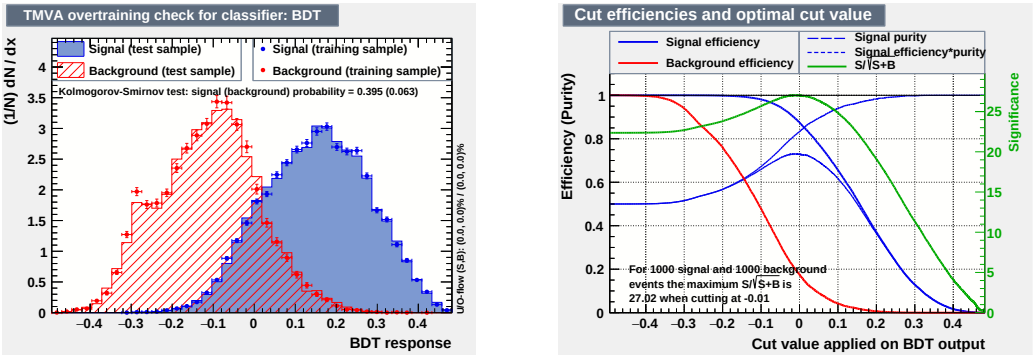

(a) (b)

Figure 7.24 – 7.24(a): Response of the BDT classifer for the $Heavy\,nuclide/p+He$ separation. 7.24(b): η_s (blue), η_b (red) and $S/\sqrt{S+B}$ (green) over the range of classifier response.

of *Signal* or *Background* is made for this event.

In the algorithm training of the BDTG classifier, most training parameters correspond to the default settings, since they have been tested and set to the optimal values by the TMVA team. Some parameters are modified for a balance between the performance of the classifier and the time consumption by the processors or to avoid overtraining.

- The number of decision trees is adjusted to 500 (default value: 1000). The tests with various values from 500 to 1000 show that it does not significantly affect the current result.
- The number of the grid points in variable range used to select the optimal cut value in the binary decision at each node, is changed to 50 (default value: 20) to sufficiently optimize the performance of the classifier.
- The weight of each event in the training samples is defined as $\frac{1}{(dN(E)/N)\cdot N}$, where N is the number of events for each composition and $dN(E)/N$ is the relative flux for a given event with a primary energy of E.

Results and discussion

The BDTG classifiers for the separation of $Iron/proton$ and Heavy nuclide/(p+He) are trained and applied to the simulation data of the LHAASO hybrid detection. The responses of the two separations are shown in Figure 7.25 and Figure 7.26. The cut values for $Iron/proton$ and $Heavy\,nuclide/p+He$ separations are set to 0 and to -0.1, respectively, based on the analysis of *Signal-to-Background* ratio. The cut efficiency and the contamination of each separation are calculated based on the response of each event weighted by its proportion of flux in the cosmic-ray spectrum following the Höerandel model [210] (see in Figure 7.27). For the separation of $Iron/proton$, nearly perfect results approximating the theoretical limit are obtained with the cut efficiency > 95% and the contamination < 5% over the energy range from 100 TeV to 1 PeV. For the separation of Heavy nuclide/(p+He), a clear separation for the different responses is obtained from the BDTG classification. The cut efficiency and the contamination are ~ 85% and ~ 15% over the given energy range, respectively.

The performance of the classifiers highly depends on the separation of different mass compositions with each variable. According to the variable ranking by the TMVA and the classifiers, P_μ is the most important variable for the classification, which is expected based on the physics mechanism of the EAS development. P_{lat} ranks the second as it's sensitive to X_{max} of the shower. P_E and P_{long} are both parameters which are tuned from the Cherenkov image sampled with a single telescope at the observatory level. They are specially used for energy

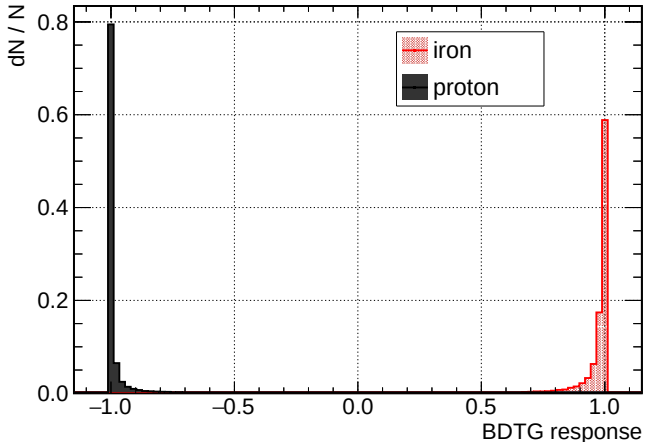

Figure 7.25 – Responses of different compositions in the $Iron/proton$ separation with BDTG classifiers for all the selected events.

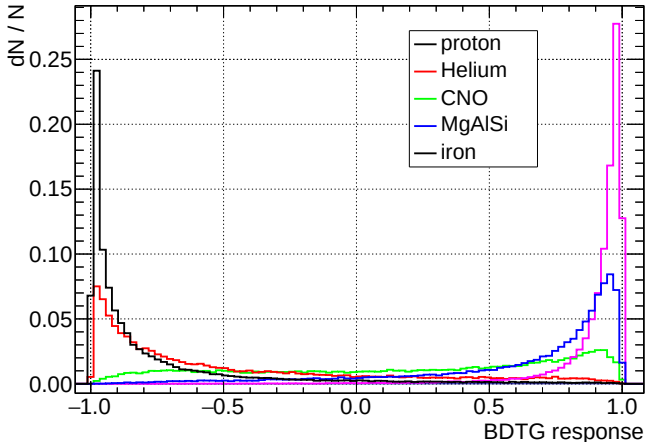

Figure 7.26 – Responses of different compositions in the Heavy nuclide/(p+He) separation with BDTG classifiers for all the selected event.

reconstruction of the showers and much less efficient than P_μ and P_{lat} for the separation with individual variables. However, they are also helpful in a fair proportion of the decision trees, since the shower energy and the primary mass are interrelated in the classification.

7.7 Summary

The WFCTA simulation code,“NewTel”, has been updated. Compared to the previous version, this new program has a better modularization for the structure and an elaborate simulation of each process (optical ray-tracing, camera response, and pattern trigger). According to the simulation results, WFCTA can precisely reconstruct the shower energy with a resolution of ~20% over the energy range of 100 TeV to 10 PeV.

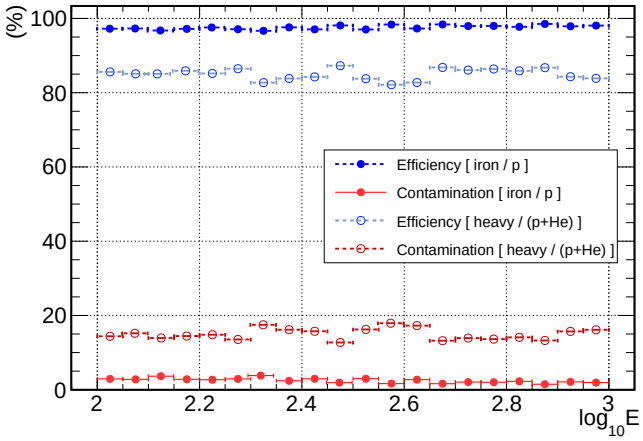

Figure 7.27 – Efficiency and contamination of the Heavy nuclide/(p+He) and $Iron/proton$ separations.

Primary particle identification based on the simulations of the LHAASO hybrid detection of the EAS has been implemented by using the MVA method over the energy range from 100 TeV to 1 PeV. Simulated data for various detector arrays of LHAASO are parameterized and tuned for the training of the MVA classifiers. The first results show almost perfect separations for $Iron/proton$ and good separations for Heavy nuclide/(p+He) with the BDTG classifier. This part of work has been reported as a proceeding for ICRC 2017 (*Primary particle identification with MVA method for the LHAASO project*, PoS (ICRC2017) 547) by the author of this thesis. Further studies will be performed with better statistics for mass composition and for a larger energy range of cosmic rays.

8

Conclusions

The development of instrumentation and analysis methods is crucial for modern cosmic-ray experiments. By using new technologies and experimental methods, accurate measurements of the high-energy cosmic-ray properties are expected to be performed in the near future. Following the physics motivations and the technical specifications of the AugerPrime and LHAASO projects, four research topics are presented in this thesis. The conclusions and related perspectives of each topic are summarized as follows:

The AugerPrime project consists of several implementations with the aim to improve capability in particle identification on an event-by-event basis. The key part of AugerPrime is the scintillator surface detector (SSD). In this thesis, the R&D work for SSD and the data analysis of the engineering array are presented.

The studies reported in this thesis concern the candidate SSD components including scintillators, WLS fibers, and fiber/PMT optical coupling methods. The related results have been discussed in the collaboration meetings during the R&D phase of the SSD. The configuration (FNAL 50×10 mm^2 2-hole scintillator + Kuraray Y11(300)-MSJ ($\oslash$ 1.0 mm) WLS fiber + RTV silicone pad) was chosen based on the consideration of the performance, the reliability, and the total cost. The output signal of this detector configuration is > 30 ph.e. (HV=1100 V), which fulfills the requirement of SSD performance (> 12 ph.e.). One scintillator detector was assembled and equipped with the optical coupling module with the polishing

method developed in this work. Good results for signal amplitudes, peak-to-valley ratio, and signal uniformity are obtained from the test of this detector by using the muon tower of KIT. Currently, this detector is deployed in one of the EA stations, St.25. Further monitoring and studies on its performance are underway.

The data from the AugerPrime engineering array has been continuously taken since its deployment in October 2016. The EA performance has been investigated by monitoring various electronic and detector parameters. The results show good stability and performance for the EA operation. The observed noise levels are higher than the specifications. This has been corrected in the next prototypes currently under fabrication. Shower signals from the EA stations are in good agreement with the LDF fitted by the existing SD array. The global LDF of the S_{WCD} normalized by the shower size agrees well with the ones of the existing stations. The global LDF of S_{SSD} shows the SSD sensitivity to the EM components of the EAS, as expected. The study of WCD signal accuracy yields a preliminary result of ~10% for the EA stations, which is comparable to that of the existing SD array. Further studies on the EA performance with better statistics are currently underway.

The LHAASO observatory composed of 4 detector arrays, WCDA, WFCTA, and KM2A (ED & MD), is currently under construction. One of the scientific goals of LHAASO is to precisely measuring the cosmic-ray spectrum from 30 TeV to 100 PeV. The simulations for LHAASO-WFCTA and the analysis preparation for the LHAASO-hybrid detector consisting of WCDA, WFCTA, and KM2A have been presented in this thesis.

The simulation code of the WFCTA has been updated. The new simulation code has a modularized structure, a precise optical ray-tracing, an enriched camera simulation and an adaptable trigger simulation. The WFCTA is predicted to measure the primary energy of the air showers with an accuracy of ~20% over the energy range of 100 TeV to 10 PeV.

The particle identification with the LHAASO-hybrid simulation data by using the MVA method has been implemented. Good results are shown for the $Iron/proton$ and $Heavy\,nuclide/p + He$ separations. Further studies are expected to be performed with better statistics for mass composition and for a larger energy range of cosmic rays.

A

Fabrication procedures of the polished coupling module

The fabrication procedures of the polished SSD fiber/PMT coupling module are presented below:

1. Assemble the detector and wrap the fiber ends together. The SSD detector is designed to be fixed in an enclosure box. First of all, we assembled the entire detector, including the scintillator bars, the optical fibers, and the fiber routers, in the enclosure frame. The fibers are inserted into the holes along the scintillators and placed in the fiber routers. After the assembling, the fiber ends are gathered together and wrapped with Teflon tape to form a compact bundle in the center zone of the detector. The fiber ends are aligned at the same level, with a tolerance range of up to 5 mm (see Figure A.1, left).

2. Glue the fiber ends with the coupling PMMA cylinder in the Teflon container. The plastic cylinder support of the coupling module is made of PMMA. It has been realized at IPN-Orsay following the dimension of the plastic coupling module used in the melted fiber coupling design [154]. On this PMMA cylinder, one hole with a diameter of 13mm is drilled along the central axis. Four smaller holes are drilled at the edge of the cylinder to allocate the

screws needed to fix the coupling element on the PMT housing module (see Figure A.2). A Teflon container was as well fabricated in order to keep the fibers and the PMMA support in place during the glue curing process. This element matches the dimension of the PMMA support and has a 5 mm-long spare space along the central axis to contain the fiber ends. The central part of the Teflon container is drilled off. An aluminum cylinder with a Teflon layer attached at the top and a screw nut installed at the bottom is used to fill the central hole of the Teflon container (see Figure A.3). This design was realized with the aim to ease the PMMA support removal after the gluing process, by simply pushing up the small Teflon cylinder with a screw. We performed the gluing with Saint-Gobain BC600 optical cement that has been widely used in many long-lasting experiments. As the first step of this operation, we inject a few microliters of BC600 into the hole of the PMMA support, placed in the Teflon container. Then we insert the fiber bundle into the hole controlling that each fiber end is touching the bottom of the Teflon container. Finally, the whole coupling module together with the fiber bundle is kept still for 12 h for a complete cure of the BC600 glue (see Figure A.4). In this procedure, the curing time is shorter than suggested, at room temperature, in the BC600 data sheet, since in our design the glue is not used as the optical element but only to provide more rigidity and stability to the bundle and to fill the empty spaces between the fibers.

3. Push the coupling module out of the Teflon container after gluing. When the glue curing is completed, we push the coupling module out of the Teflon container with a long screw and a screwdriver. The whole coupling module including the PMMA support and the fiber bundle is, in this way, separated from the Teflon container (see Figure A.5).

4. Polish the fiber ends with sandpapers of different roughness. A 5mm-long excess of fibers outside the PMMA support ensures that all the fiber ends can be adequately polished in this step . We first polish this protruding part by hand with 200-grit and 320-grit sandpapers until the excess is removed and the surface is even. Then, 800-grit and 1200-grit sandpapers are used to polish the surface of the PMMA support and the fiber ends to make them smoother (see Figure A.6, left and center).

5. Buff the fiber ends with a loose cotton installed on an electric polisher. We employ an electric polisher with a 1-inch loose cotton wheel installed on it to finish the last buffing procedure. As the loose cotton is quite soft, it will collapse and not damage the surface when touching the material. When doing the buffing, we keep the spindle speed of the polisher below 10000 revolutions per minute as a proper speed for both protecting the surface from splitting off and ensuring it is buffed well. After the buffing with the loose cotton, the surface

of each fiber ends gets clear and the emitted lights of the fibers are uniformly distributed throughout the whole bundle surface (see Figure A.6, right).

6. Fix the coupling module on the PMT tube with a silicone pad as couplant. The whole coupling module is fixed on top of the PMT aluminum housing with four screws. A silicone pad is attached to the fiber bundle as optical couplant between the fiber ends and the PMT entrance window (see Figure A.7 and Figure A.8). The silicone pad is made of Room Temperature Vulcanization (RTV) silicone materials. In our design, the RTV silicone type we used is RHODORSIL RTV 141 A&B. The silicon pad is fabricated by mixing two reagents (A and B) with a ratio of 100:5. Similar RTV silicones are also produced by some other companies like Wacker and GE silicone. The GE6136 RTV silicone has been applied in the Auger Surface Detector as optical couplant for more than 10 years. Thus, the RTV silicone pad is expected to have a good performance against the aging when working in the field for a long time.

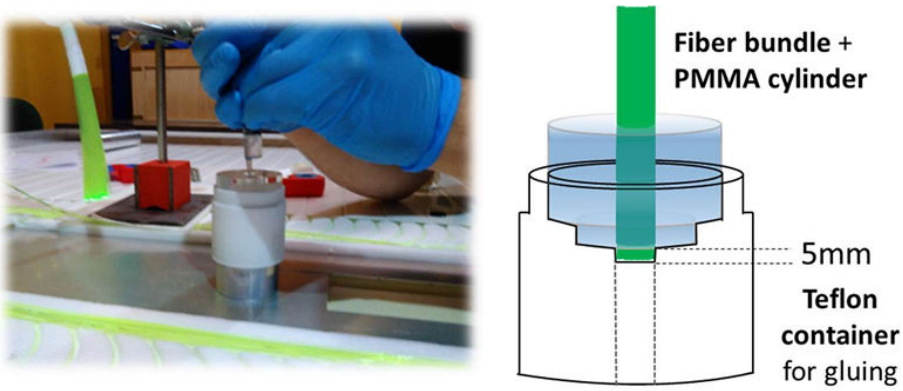

Figure A.1 – Preparation of the gluing. Fiber ends are aligned at the same level, a few microliters of BC600 is injected into the hole in the PMMA cylinder that is placed in the Teflon container (left). In the Teflon container, 5mm-long spare space is reserved for the fiber bundle excess. This design aims to ensure all the fiber ends can be polished after gluing (right).

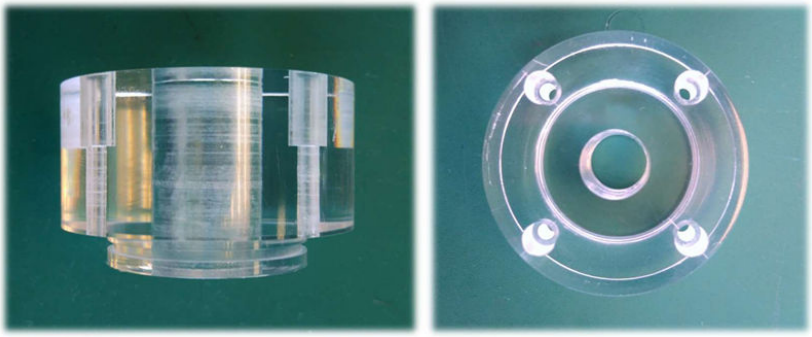

Figure A.2 – The coupling module is made of PMMA, with one hole along the central axis for the fiber bundle placement and four holes on the edge for the screws used to fix it on the PMT aluminum housing.

Figure A.3 – The Teflon container is drilled along the central axis (left). An aluminum cylinder with a Teflon layer at the top and a screw nut at the bottom (center). By pushing the aluminum cylinder with a screw, the PMMA support and the fiber bundle can be easily separated after gluing (right).

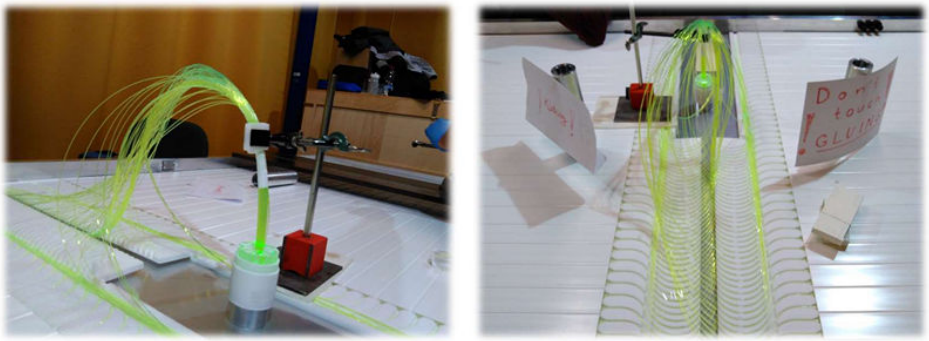

Figure A.4 – The whole coupling module is placed in the Teflon container and kept still for a cure time of 12h.

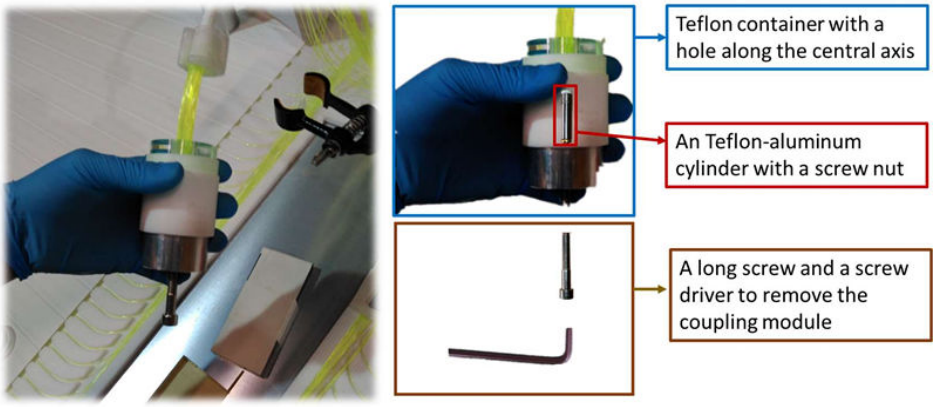

Figure A.5 – After gluing, we remove the coupling module out of the container by pushing it with a screw and a screwdriver.

Figure A.6 – We polish off the protruding 5mm-long fibers with heavy-grade sandpapers (200, 320 grit) (left). Then we polish the fiber ends and PMMA surface with fine-grade sandpaper (800, 1200 grit) (center) and buff the fiber ends with a 1-inch loose cotton wheel on an electric polisher rotating at a spindle speed below 10000 revolutions per minute (right).

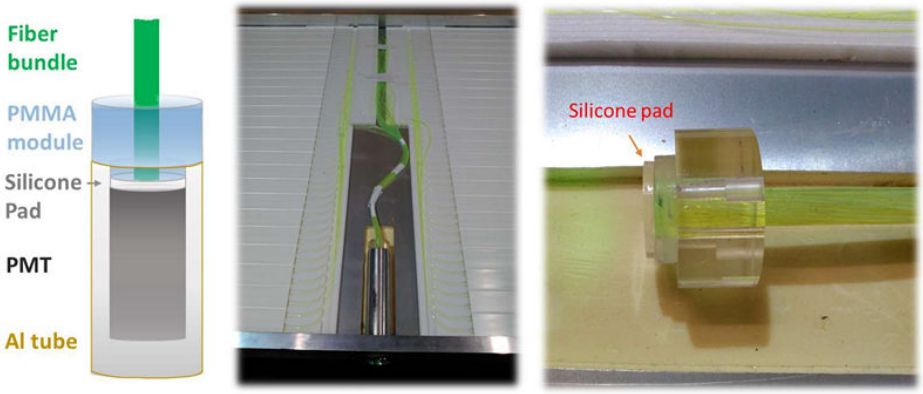

Figure A.7 – The coupling module is installed on top of an aluminum housing and fixed with 4 screws. A silicone pad is attached in front to the fiber bundle as couplant between the PMT entrance window and the fiber ends.

Figure A.8 – The PMT aluminum housing is installed on the frame. This photo is taken before the installation of the PMT, the scintillation lights are emitting out of the coupling part.

Bibliography

[1]C. T. Wilson, "On the leakage of electricity through dust-free air," in Proc. camb. phil. soc, Vol. 11 (1900), p. 32.

[2]E. Rutherford and H. L. Cooke, "A penetrating radiation from the earth's surface," Physical Review **16**, 183 (1903).

[3]T. Wulf, "Uber die in der Atmosphare vorhandene Strahlung von hoher Durchdringungsfahigkeit," Physikalische Zeitschrift **10**, 152–157 (1909).

[4]V. F. Hess, "Uber Beobachtungen der durchdringenden Strahlung bei sieben Freiballonfahrten," Z. Phys. **13**, 1084 (1912).

[5]W. Kolhörster, "Messungen der durchdringenden Strahlung im Freiballon in grosseren Hohen," Physikalische Zeitschrift **14**, 1153–1156 (1913).

[6]W. Kolhörster, "Messungen der durchdringenden Strahlungen bis in Hohen von 9300 m," Verh. Dtsch. Phys. Ges **16**, 719–721 (1914).

[7]R. A. Millikan and G. H. Cameron, "High frequency rays of cosmic origin III. Measurements in snow-fed lakes at high altitudes," Physical Review **28**, 851 (1926).

[8]C. D. Anderson, "The positive electron," Physical Review **43**, 491 (1933).

[9]S. H. Neddermeyer and C. D. Anderson, "Cosmic-ray particles of intermediate mass," Physical Review **54**, 88 (1938).

[10]G. Rochester and C. C. Butler, "Evidence for the existence of new unstable elementary particles," Nature **160**, 855 (1947).

[11]D. Perkins, "Nuclear disintegration by meson capture," Nature **159**, 126–127 (1947).

[12]H. Yukawa, "On the interaction of elementary particles. I," Nippon Sugaku-Buturigakkwai Kizi Dai 3 Ki **17**, 48–57 (1935).

[13]H. YUKAWA and S. SAKATA, "On the Theory of the Beta-Disintegration and the Allied Phenomenon," Proceedings of the Physico-Mathematical Society of Japan. 3rd Series **17**, 467–479 (1935).

[14]H. YUKAWA and S. SAKATA, "On the theory of internal pair production," Nippon Sugaku-Buturigakkwai Kizi Dai 3 Ki **17**, 397–407 (1935).

[15]R. Armenteros, K. Barker, C. Butler, and A. Cachon, "CXIII. The properties of neutral V-particles," The London, Edinburgh, and Dublin Philosophical Magazine and Journal of Science **42**, 1113–1135 (1951).

[16]R. Armenteros, K. Barker, C. Butler, A. Cachon, and A. Chapman, "Decay of V-particles.," Nature **167**, 501–503 (1951).

[17]H. Geiger and W. Müller, "Elektronenzahlrohr zur messung schwachster aktivitaten," Naturwissenschaften **16**, 617–618 (1928).

[18]W. Bothe and W. Kolhörster, "Das wesen der höhenstrahlung," Zeitschrift für Physik A Hadrons and Nuclei **56**, 751–777 (1929).

[19]P. Auger, P. Ehrenfest, R. Maze, J. Daudin, and R. A. Fréon, "Extensive cosmic-ray showers," Reviews of Modern Physics **11**, 288 (1939).

[20]J. Linsley, "Evidence for a primary cosmic-ray particle with energy 10^{20} eV," Physical Review Letters **10**, 146 (1963).

[21]P. Roll and D. T. Wilkinson, "Cosmic background radiation at 3.2 cm-support for cosmic black-body radiation," Physical Review Letters **16**, 405 (1966).

[22]K. Greisen, "End to the cosmic-ray spectrum?" Physical Review Letters **16**, 748 (1966).

[23]G. T. Zatsepin and V. A. Kuzmin, "Upper limit of the spectrum of cosmic rays," JETP lett. **4**, 114–116 (1966).

[24]D. Bird, S. Corbato, H. Dai, B. Dawson, J. Elbert, T. Gaisser, K. Green, M. Huang, D. B. Kieda, S. Ko, et al., "Evidence for correlated changes in the spectrum and composition of cosmic rays at extremely high energies," Physical Review Letters **71**, 3401 (1993).

[25]N. Hayashida, K. Honda, M. Honda, S. Imaizumi, N. Inoue, K. Kadota, F. Kakimoto, K. Kamata, S. Kawaguchi, N. Kawasumi, et al., "Observation of a very energetic cosmic ray well beyond the predicted 2.7 k cutoff in the primary energy spectrum," Physical Review Letters **73**, 3491 (1994).

[26]S. Yoshida, N. Hayashida, K. Honda, M. Honda, S. Imaizumi, N. Inoue, K. Kadota, F. Kakimoto, K. Kamata, S. Kawaguchi, et al., "The cosmic ray energy spectrum above 3×10^{18} eV measured by the Akeno Giant Air Shower Array," Astroparticle Physics **3**, 105–123 (1995).

[27]H. R. F. E. Collaboration, R. Abbasi, T. Abu-Zayyad, M. Allen, J. Amman, G. Archbold, K. Belov, J. Belz, S. B. Zvi, D. Bergman, et al., "First observation of the Greisen-Zatsepin-Kuzmin suppression," Physical Review Letters **100**, 101101 (2008).

[28]A. Collaboration et al., "The Pierre Auger observatory project: an overview," in International cosmic ray conference, Vol. 5 (1997), p. 205.

[29]A. Collaboration et al., *The Pierre Auger Observatory design report*, 1997.

[30]The Pierre Auger Collaboration, "Observation of the suppression of the flux of cosmic rays above $4{\times}10^{19}$ eV," Physical Review Letters **101**, 061101 (2008).

[31]A. A. Pacini, "Cosmic rays: bringing messages from the sky to the Earth's surface," Revista Brasileira de Ensino de Fisica **39** (2017).

[32]M. Unger, for the Pierre Auger Collaboration, "Highlights from the Pierre Auger Observatory," in International cosmic ray conference, Vol. 3 (2017).

[33]P. K. Grieder, *Cosmic rays at Earth* (Gulf Professional Publishing, 2001).

[34]K. Greisen, "Cosmic ray showers," Annual Review of Nuclear Science **10**, 63–108 (1960).

[35]W. Heitler, *The quantum theory of radiation* (Courier Corporation, 1954).

[36]J. Matthews, "A heitler model of extensive air showers," Astroparticle Physics **22**, 387–397 (2005).

[37]K. Kamata and J. Nishimura, "The lateral and the angular structure functions of electron showers," Progress of Theoretical Physics Supplement **6**, 93–155 (1958).

[38]K. Greisen, "The extensive air showers," Progress in Cosmic Ray Physics **3** (1956).

[39]G. Moliere, "Theorie der streuung schneller geladener teilchen ii mehrfach-und vielfachstreuung," Zeitschrift für Naturforschung A **3**, 78–97 (1948).

[40]G. Moliere, "Theory of scattering of fast charged particles. 3: multiple scattering of tracks and the influence of statistical coupling(multiple scattering of tracks and statistical coupling influence, using chords and angle between neighboring tangents)," Z. Naturforsch.,(Tubingen) **10**, 177–211 (1955).

[41]A. Hillas, "The sensitivity of cerenkov radiation pulses to the longitudinal development of cosmic-ray showers," Journal of Physics G: Nuclear Physics **8**, 1475 (1982).

[42]J. Patterson and A. Hillas, "The relation of the lateral distribution of cerenkov light from cosmic-ray showers to the distance of maximum development," Journal of Physics G: Nuclear Physics **9**, 1433 (1983).

[43]T. K. Gaisser and A. M. Hillas, "Reliability of the method of constant intensity cuts for reconstructing the average development of vertical showers," in International cosmic ray conference, Vol. 8 (1977), pp. 353–357.

[44]J. Linsley, "Structure of large air showers at depth 834 g/sq cm. iii-applications," in International cosmic ray conference, Vol. 12 (1977), pp. 89–96.

[45]J. Linsley and A. Watson, "Validity of scaling to 10 20 ev and high-energy cosmic-ray composition," Physical Review Letters **46**, 459 (1981).

[46]T. Gaisser, P. Freier, and C. Waddington, "Correlation between meson production and nuclear fragmentation in collisions between nuclei," in International cosmic ray conference, Vol. 6 (1979), p. 251.

[47]J. V. Jelley, "Cerenkov radiation and its applications," British Journal of Applied Physics **6**, 227 (1955).

[48]Y. Chen, "Simulations and electronics development for the LHAASO experiment," PhD thesis (Paris 11, 2015).

[49]G. Inman, "Characteristics of fluorescent lamps," Red **3**, 3 (1939).

[50]P. Sokolsky, "Introduction to ultrahigh energy cosmic ray physics.," Frontiers in Physics, Vol. 76, **76** (1989).

[51]B. Keilhauer, M. Bohacova, M. Fraga, J. Matthews, N. Sakaki, Y. Tameda, Y. Tsunesada, and A. Ulrich, "Nitrogen fluorescence in air for observing extensive air showers," in Epj web of conferences, Vol. 53 (EDP Sciences, 2013), p. 01010.

[52]F. G. Schröder, "Radio detection of cosmic-ray air showers and high-energy neutrinos," Progress in Particle and Nuclear Physics **93**, 1–68 (2017).

[53]F. Kahn and I. Lerche, "Radiation from cosmic ray air showers," in Proceedings of the royal society of london a: mathematical, physical and engineering sciences, Vol. 289, 1417 (The Royal Society, 1966), pp. 206–213.

[54]F. Schröder, D. Besson, N. Budnev, O. Gress, A. Haungs, R. Hiller, Y. Kazarina, M. Kleifges, A. Konstantinov, E. Korosteleva, et al., "Tunka-Rex: A radio antenna array for the Tunka experiment," in Aip conference proceedings, Vol. 1535, 1 (AIP, 2013), pp. 111–115.

[55]A. A. Abdo, M. Ackermann, M. Ajello, W. Atwood, M. Axelsson, L. Baldini, J. Ballet, G. Barbiellini, D. Bastieri, M. Battelino, et al., "Measurement of the cosmic ray $e^+ + e^-$ spectrum from 20 GeV to 1 TeV with the Fermi Large Area Telescope," Physical Review Letters **102**, 181101 (2009).

[56]O. Adriani, G. Barbarino, G. Bazilevskaya, R. Bellotti, M. Boezio, E. Bogomolov, L. Bonechi, M. Bongi, V. Bonvicini, S. Borisov, et al., "PAMELA measurements of cosmic-ray proton and helium spectra," arXiv preprint arXiv:1103.4055 (2011).

[57]R. Battiston, "The antimatter spectrometer (AMS-02): A particle physics detector in space," Nuclear Instruments and Methods in Physics Research Section A: Accelerators, Spectrometers, Detectors and Associated Equipment **588**, 227–234 (2008).

[58]E. Atkin, V. Bulatov, V. Dorokhov, S. Filippov, N. Gorbunov, V. Grebenyuk, D. Karmanov, I. Kovalev, I. Kudryashov, A. Kurganov, et al., "The NUCLEON experiment. Results of the first year of data acquisition," Astroparticle Physics **90**, 69–74 (2017).

[59]S. Torii et al., "The CALorimetric Electron Telescope (CALET): High-Energy Astroparticle Physics Observatory on the International Space Station," in 34th international cosmic ray conference (2015).

[60]C. Jin, "Dark matter particle explorer: the first chinese cosmic ray and hard γ-ray detector in space," Chinese Journal of Space Science **34**, 550–557 (2014).

[61]S. Ostapchenko, "Monte Carlo treatment of hadronic interactions in enhanced Pomeron scheme: QGSJET-II model," Physical Review D **83**, 014018 (2011).

[62]E.-J. Ahn, R. Engel, T. K. Gaisser, P. Lipari, and T. Stanev, "Cosmic ray interaction event generator SIBYLL 2.1," Physical Review D **80**, 094003 (2009).

[63]K. Werner, F.-M. Liu, and T. Pierog, "Parton ladder splitting and the rapidity dependence of transverse momentum spectra in deuteron-gold collisions at the BNL Relativistic Heavy Ion Collider," Physical Review C **74**, 044902 (2006).

[64]K. A. Olive, P. D. Group, et al., "Review of particle physics," Chinese physics C **38**, 090001 (2014).

[65]Measuring cosmic-ray and gamma-ray air showers, https://www.mpi-hd.mpg.de/hfm/CosmicRay/ShowerDetection.html.

[66]M. Aglietta, B. Alessandro, P. Antonioli, F. Arneodo, L. Bergamasco, M. Bertaina, C. Castagnoli, A. Castellina, A. Chiavassa, G. C. Castagnoli, et al., "The cosmic ray primary composition in the "knee" region through the EAS electromagnetic and muon measurements at EAS-TOP," Astroparticle physics **21**, 583–596 (2004).

[67]T. Antoni, W. Apel, F. Badea, K. Bekk, A. Bercuci, H. Blümer, H. Bozdog, I. Brancus, C. Büttner, A. Chilingarian, et al., "The cosmic-ray experiment KASCADE," Nuclear Instruments and Methods in Physics Research Section A: accelerators, spectrometers, detectors and associated equipment **513**, 490–510 (2003).

[68]e. W. Apel, J. Arteaga, A. Badea, K. Bekk, M. Bertaina, J. Blümer, H. Bozdog, I. Brancus, P. Buchholz, E. Cantoni, et al., "The kascade-grande experiment," Nuclear Instruments and Methods in Physics Research Section A: accelerators, spectrometers, detectors and associated equipment **620**, 202–216 (2010).

[69]Pierre Auger Collaboration, "The Pierre Auger Cosmic Ray Observatory," Nuclear Instruments and Methods in Physics Research Section A: Accelerators, Spectrometers, Detectors and Associated Equipment **798**, 172–213 (2015).

[70]R. Baltrusaitis, R. Cady, G. Cassiday, R. Cooperv, J. Elbert, P. Gerhardy, S. Ko, E. Loh, M. Salamon, D. Steck, et al., "The Utah Fly's eye detector," Nuclear Instruments and Methods in Physics Research Section A: Accelerators, Spectrometers, Detectors and Associated Equipment **240**, 410–428 (1985).

[71]J. Abraham, P. Abreu, M. Aglietta, C. Aguirre, E. Ahn, D. Allard, I. Allekotte, J. Allen, P. Allison, J. Alvarez-Muniz, et al., "The fluorescence detector of the Pierre Auger Observatory," Nuclear Instruments and Methods in Physics Research Section A: Accelerators, Spectrometers, Detectors and Associated Equipment **620**, 227–251 (2010).

[72]H. Tokuno, Y. Tameda, M. Takeda, K. Kadota, D. Ikeda, M. Chikawa, T. Fujii, M. Fukushima, K. Honda, N. Inoue, et al., "New air fluorescence detectors employed in the Telescope Array experiment," Nuclear Instruments and Methods in Physics Research Section A: Accelerators, Spectrometers, Detectors and Associated Equipment **676**, 54–65 (2012).

[73]V. Prosin, S. Berezhnev, N. Budnev, A. Chiavassa, O. Chvalaev, O. Gress, A. Dyachok, S. Epimakhov, N. Karpov, N. Kalmykov, et al., "Tunka-133: results of 3 year operation," Nuclear Instruments and Methods in Physics Research Section A: Accelerators, Spectrometers, Detectors and Associated Equipment **756**, 94–101 (2014).

[74]M. Cassidy, L. Fortson, J. Fowler, R. Ong, C. Jui, D. Kieda, E. Loh, and P. Sommers, "Casa-blanca: a large non-imaging cherenkov detector at casa-mia," arXiv preprint astro-ph/9707038 (1997).

[75]Pierre Auger Collaboration, "The Pierre Auger project design report," Nov. 1996, Revised Mar. 1997) p **21** (1997).

[76]Pierre Auger Collaboration, "Measurement of the depth of maximum of extensive air showers above 10^{18} eV," Physical Review Letters **104**, 091101 (2010).

[77]Pierre Auger Collaboration, "Interpretation of the depths of maximum of extensive air showers measured by the Pierre Auger Observatory," arXiv preprint arXiv:1301.6637 (2013).

[78]Pierre Auger Collaboration, "Muons in air showers at the Pierre Auger Observatory: Measurement of atmospheric production depth," Physical Review D **90**, 012012 (2014).

[79]A. Aab, P. Abreu, M. Aglietta, I. Al Samarai, I. Albuquerque, I. Allekotte, A. Almela, J. A. Castillo, J. Alvarez-Muñiz, G. Anastasi, et al., "Combined fit of spectrum and composition data as measured by the Pierre Auger Observatory," Journal of Cosmology and Astroparticle Physics **2017**, 038 (2017).

[80]Pierre Auger collaboration, "Evidence for a mixed mass composition at the 'ankle' in the cosmic-ray spectrum," Physics Letters B **762**, 288–295 (2016).

[81]Pierre Auger Collaboration, "Measurement of the cosmic ray spectrum above 4×10^{18} eV using inclined events detected with the Pierre Auger Observatory," arXiv preprint arXiv:1503.07786 (2015).

[82]C. Bonifazi and Pierre Auger Collaboration, "The angular resolution of the Pierre Auger Observatory," Nuclear Physics B-Proceedings Supplements **190**, 20–25 (2009).

[83]Pierre Auger Collaboration, "Correlation of the highest-energy cosmic rays with nearby extragalactic objects," Science **318**, 938–943 (2007).

[84]J. Abraham, P. Abreu, M. Aglietta, C. Aguirre, D. Allard, I. Allekotte, J. Allen, P. Allison, J. Alvarez-Muñiz, M. Ambrosio, et al., "Correlation of the highest-energy cosmic rays with the positions of nearby active galactic nuclei," Astroparticle Physics **29**, 188–204 (2008).

[85]A. Aab, P. Abreu, M. Aglietta, I. A. Samarai, I. Albuquerque, I. Allekotte, A. Almela, J. A. Castillo, J. Alvarez-Muñiz, G. Anastasi, et al., "Multi-resolution anisotropy studies of ultrahigh-energy cosmic rays detected at the Pierre Auger Observatory," arXiv preprint arXiv:1611.06812 (2016).

[86]A. Aab, P. Abreu, M. Aglietta, M. Ahlers, E. Ahn, I. Al Samarai, I. Albuquerque, I. Allekotte, J. Allen, P. Allison, et al., "A search for point sources of EeV photons," The Astrophysical Journal **789**, 160 (2014).

[87]M. Settimo, "Search for ultra-High Energy Photons with the Pierre Auger Observatory," Proc. Science Photon **62** (2013).

[88]Pierre Auger Collaboration, "A targeted search for point sources of EeV photons with the Pierre Auger Observatory," The Astrophysical Journal Letters **837**, L25 (2017).

[89]Pierre Auger Collaboration, "A search for point sources of EeV photons," Astrophysical Journal, 2014, vol. 789, num. 2, p. 160-1-160-12 (2014).

[90]P. Abreu, M. Aglietta, M. Ahlers, E. Ahn, I. F. d. M. Albuquerque, D. Allard, I. Allekotte, J. Allen, P. Allison, A. Almela, et al., "Search for point-like sources of ultra-high energy neutrinos at the Pierre Auger Observatory and improved limit on the diffuse flux of tau neutrinos," The Astrophysical Journal Letters **755**, L4 (2012).

[91]P. Abreu, M. Aglietta, M. Ahlers, E. Ahn, I. Albuquerque, D. Allard, I. Allekotte, J. Allen, P. Allison, A. Almela, et al., "Ultrahigh energy neutrinos at the Pierre Auger Observatory," Advances in High Energy Physics **2013** (2013).

[92]Pierre Auger Collaboration, "Ultrahigh-energy neutrino follow-up of gravitational wave events GW150914 and GW151226 with the Pierre Auger Observatory," Physical Review D **94**, 122007 (2016).

[93]The Pierre Auger Collaboration, "A search for point sources of EeV neutrons," The Astrophysical Journal **760**, 148 (2012).

[94]The Pierre Auger Collaboration, "A targeted search for point sources of EeV neutrons," The Astrophysical Journal Letters **789**, L34 (2014).

[95]The Pierre Auger Collaboration, "Measurement of the proton-air cross section at $\sqrt{s}$= 57 TeV with the Pierre Auger Observatory," Physical review letters **109**, 062002 (2012).

[96]T. Csörgő, G. Antchev, P. Aspell, I. Atanassov, V. Avati, J. Baechler, V. Berardi, M. Berretti, E. Bossini, M. Bozzo, et al., "Elastic Scattering and Total Cross-Section in p+ p reactions as Measured by the LHC Experiment TOTEM at $\sqrt{s}$ = 7 TeV," Progress of Theoretical Physics Supplement **193**, 180–183 (2012).

[97]T. Gaisser, "Viewpoint: Cosmic-Ray Showers Reveal Muon Mystery," Physics **9**, 125 (2016).

[98]P. Facal San Luis, "Measurement of the UHECR spectrum above 10^{19} eV at the Pierre Auger Observatory using showers with zenith angles greater than 60°," in International cosmic ray conference, Vol. 4 (2008), pp. 339–342.

[99]E.I. du Pont de Nemours and Co., Wilmington, Delaware, U.S.A., http://www.dupont.com.

[100]I. Allekotte, A. Barbosa, P. Bauleo, C. Bonifazi, B. Civit, C. Escobar, B. García, G. Guedes, M. G. Berisso, J. Harton, et al., "The surface detector system of the Pierre Auger Observatory," Nuclear Instruments and Methods in Physics Research Section A: Accelerators, Spectrometers, Detectors and Associated Equipment **586**, 409–420 (2008).

[101] J. Abraham, P. Abreu, M. Aglietta, E. Ahn, D. Allard, I. Allekotte, J. Allen, J. Alvarez-Muñiz, M. Ambrosio, L. Anchordoqui, et al., "Trigger and aperture of the surface detector array of the Pierre Auger Observatory," Nuclear Instruments and Methods in Physics Research Section A: Accelerators, Spectrometers, Detectors and Associated Equipment **613**, 29–39 (2010).

[102] C. Meurer, N. Scharf, et al., "HEAT-a low energy enhancement of the Pierre Auger Observatory," arXiv preprint arXiv:1106.1329 (2011).

[103] Photonis, *Photomultiplier tube*, https://www.photonis.com/.

[104] M. J. Tueros, "Estimate of the non-calorimetric energy of showers observed with the fluorescence and surface detectors of the Pierre Auger Observatory," in Proceedings of the 33rd int. cosmic ray conf., rio de janeiro, brazil (2013).

[105] D. Newton, J. Knapp, and A. Watson, "The optimum distance at which to determine the size of a giant air shower," Astroparticle Physics **26**, 414–419 (2007).

[106] J. Hersil, I. Escobar, D. Scott, G. Clark, and S. Olbert, "Observations of extensive air showers near the maximum of their longitudinal development," Physical Review Letters **6**, 22 (1961).

[107] A. Schulz et al., "The measurement of the energy spectrum of cosmic rays above 3×10^{17} eV with the Pierre Auger Observatory," Proceedings of the 33rd ICRC, Rio de Janeiro, Brasil (2013).

[108] V. Verzi, "The energy scale of the Pierre Auger Observatory," Proceedings of the 33rd ICRC, Rio de Janeiro, Brasil (2013).

[109] R. Pesce, "Energy calibration of data recorded with the surface detectors of the Pierre Auger Observatory: an update," Proc. 32nd ICRC, Beijing, China (2011).

[110] V. Berezinsky, A. Gazizov, and S. Grigorieva, "On astrophysical solution to ultrahigh energy cosmic rays," Physical Review D **74**, 043005 (2006).

[111] V. S. Berezinsky, S. Grigorieva, and B. Hnatyk, "Extragalactic UHE proton spectrum and prediction for iron-nuclei flux at 10^8–10^9 GeV," Astroparticle Physics **21**, 617–625 (2004).

[112] T. Wibig and A. W. Wolfendale, "At what particle energy do extragalactic cosmic rays start to predominate?" Journal of Physics G: Nuclear and Particle Physics **31**, 255 (2005).

[113] A. Hillas, "Can diffusive shock acceleration in supernova remnants account for high-energy galactic cosmic rays?" Journal of Physics G: Nuclear and Particle Physics **31**, R95 (2005).

[114]D. Allard, E. Parizot, A. Olinto, E. Khan, and S. Goriely, "UHE nuclei propagation and the interpretation of the ankle in the cosmic-ray spectrum," Astronomy & Astrophysics **443**, L29–L32 (2005).

[115]D. Allard, "Extragalactic propagation of ultrahigh energy cosmic-rays," Astroparticle Physics **39**, 33–43 (2012).

[116]T. K. Gaisser, T. Stanev, and S. Tilav, "Cosmic ray energy spectrum from measurements of air showers," Frontiers of Physics **8**, 748–758 (2013).

[117]K. Fang, K. Kotera, and A. V. Olinto, "Ultrahigh energy cosmic ray nuclei from extragalactic pulsars and the effect of their Galactic counterparts," Journal of Cosmology and Astroparticle Physics **2013**, 010 (2013).

[118]V. Aranda et al., "Depth of maximum of air-shower profiles at the Pierre Auger Observatory. II. Composition implications," Physical Review D **90**, 122006–1 (2014).

[119]The Pierre Auger Collaboration, "The Pierre Auger Observatory Upgrade - Preliminary Design Report," 201 (2016).

[120]P. Lipari, "Concepts of "age" and "universality" in cosmic ray showers," Physical Review D **79**, 063001 (2009).

[121]S. Lafebre, R. Engel, H. Falcke, J. Hörandel, T. Huege, J. Kuijpers, and R. Ulrich, "Universality of electron–positron distributions in extensive air showers," Astroparticle Physics **31**, 243–254 (2009).

[122]A. Hillas, "Angular and energy distributions of charged particles in electron-photon cascades in air," Journal of Physics G: Nuclear Physics **8**, 1461 (1982).

[123]M. Giller, A. Kacperczyk, J. Malinowski, W. Tkaczyk, and G. Wieczorek, "Similarity of extensive air showers with respect to the shower age," Journal of Physics G: Nuclear and Particle Physics **31**, 947 (2005).

[124]F. Nerling, J. Blümer, R. Engel, and M. Risse, "Universality of electron distributions in high-energy air showers—Description of Cherenkov light production," Astroparticle Physics **24**, 421–437 (2006).

[125]F. Schmidt, M. Ave, L. Cazon, and A. Chou, "A model-independent method of determining energy scale and muon number in cosmic ray surface detectors," Astroparticle Physics **29**, 355–365 (2008).

[126]D. Maurel, M. Roth, and J. Gonzalez, "Universality of the time structure of ground particle distributions and its application to the reconstruction of extensive air showers," in International cosmic ray conference (Citeseer, 2013), pp. 1–4.

[127]R. Engel, D. Heck, and T. Pierog, "Extensive air showers and hadronic interactions at high energy," Annual review of nuclear and particle science **61**, 467–489 (2011).

[128]R. Smida, for the Pierre Auger Collaboration, "Scintillator detectors of AugerPrime," in International cosmic ray conference, Vol. 3 (2017).

[129]Tiina Suomijärvi for the Pierre Auger collaboration, "New electronics for the surface detectors of the Pierre Auger Observatory," **3** (2017).

[130]A. Etchegoyen, P. A. Collaboration, et al., "Amiga, auger muons and infill for the ground array," arXiv preprint arXiv:0710.1646 (2007).

[131]B. Daniel, P. A. Collaboration, et al., "The AMIGA enhancement of the Pierre Auger Observatory," in Journal of physics: conference series, Vol. 632, 1 (IOP Publishing, 2015), p. 012088.

[132]M. Platino, M. Hampel, A. Almela, A. Krieger, D. Gorbena, A. Ferrero, G. De La Vega, A. Lucero, F. Suarez, M. Videla, et al., "AMIGA at the Auger Observatory: the scintillator module testing system," Journal of Instrumentation **6**, P06006 (2011).

[133]A. Aab, P. Abreu, M. Aglietta, E. Ahn, I. Al Samarai, I. Albuquerque, I. Allekotte, P. Allison, A. Almela, J. A. Castillo, et al., "Muon counting using silicon photomultipliers in the AMIGA detector of the Pierre Auger observatory," Journal of Instrumentation **12**, P03002 (2017).

[134]O. Wainberg, A. Almela, M. Platino, F. Sanchez, F. Suarez, A. Lucero, M. Videla, B. Wundheiler, D. Melo, M. Hampel, et al., "Digital electronics for the Pierre Auger Observatory AMIGA muon counters," Journal of Instrumentation **9**, T04003 (2014).

[135]A. Pla-Dalmau, A. D. Bross, V. V. Rykalin, and B. M. Wood, "Extruded plastic scintillator for MINERvA," IEEE Nucl. Sci. Symp. Conf. Rec. **3**, 1298–1300 (2005).

[136]Kuraray, *Wavelength Shifting Fibers*, http://kuraraypsf.jp/psf/ws.html.

[137]Hamamatsu, "Photomultiplier tube,"

[138]Costruzioni Apparecchiature Elettroniche Nucleari S.P.A (CAEN), *High/Low Voltage Power Supply systems and Front-End/Data Acquisition modules*, http://www.caen.it/.

[139]ISEG HIGH VOLTAGE. EXACTLY., *INTEGRATED HV SUPPLIES FOR PHOTOMULIPLIER TUBES (PMT)*, http://iseg-hv.com/en/products/detail/PHQ.

[140]i-Lotus GPS, http://www.ilotus.com.sg/m12m_timing_oncore/.

[141]A. Quaranta, S. Carturan, T. Marchi, M. Buffa, M. Degerlier, M. Cinausero, G. Guastalla, F. Gramegna, G. Valotto, G. Maggioni, et al., "Doped polysiloxane scintillators for thermal neutrons detection," Journal of Non-Crystalline Solids **357**, 1921–1925 (2011).

[142]V. Senchyshyn, B. Grynyov, S. Melnychuk, V. Lagutin, M. Dracos, A. Olchevski, Y. Gornushkin, A. Nozdrin, and A. Sadovski, "Influence of polystyrene scintillator strip methods of production on their main characteristics," Radiation Measurements **42**, 911–914 (2007).

[143]M. Bowen, S. Majewski, D. Pettey, J. Walker, R. Wojcik, and C. Zorn, "A new radiation-hard plastic scintillator," Nuclear Instruments and Methods in Physics Research Section A: Accelerators, Spectrometers, Detectors and Associated Equipment **276**, 391–393 (1989).

[144]Saint-Gobain Crystals, *Wavelength Shifting Fibers*, http://www.crystals.saint-gobain.com/Scintillating_Fiber.aspx.

[145]A. Pla-Dalmau, A. D. Bross, and V. V. Rykalin, "Extruding plastic scintillator at Fermilab," in Nuclear science symposium conference record, 2003 ieee, Vol. 1 (IEEE, 2003), pp. 102–104.

[146]A. Pla-Dalmau, A. D. Bross, and K. L. Mellott, "Low-cost extruded plastic scintillator," Nucl. Instruments Methods Phys. Res. Sect. A Accel. Spectrometers, Detect. Assoc. Equip. **466**, 482–491 (2001).

[147]GNKD, *Plastic scintillator*, http://www.gaonengkedi.com/.

[148]J. Zhao, J. Liu, X.-D. Sheng, H.-H. He, Y.-Q. Guo, C. Hou, and H.-K. Lü, "Design and performances of electromagnetic particle detector for LHAASO-KM2A," Chinese Phys. C **38**, 036002 (2014).

[149]Dow Corning, *Optical Couplant*, http://www.dowcorning.com/.

[150]Bluesil, Rhodorsil, *RTV Silicone*, https://www.bluestarsilicones.com/.

[151]M. Janecek, "Reflectivity spectra for commonly used reflectors," IEEE Transactions on Nuclear Science **59**, 490–497 (2012).

[152]M. Crow, J. Hodges, and R. Cooper, "Shifting scintillator prototype large pixel wavelength-shifting fiber detector for the POWGEN3 powder diffractometer," Nuclear Instruments and Methods in Physics Research Section A: Accelerators, Spectrometers, Detectors and Associated Equipment **529**, 287–292 (2004).

[153]B. Loehr, S. Weissenrieder, F. Barreiro, and E. Ros, "An electromagnetic calorimeter with wavelength shifting fiber readout," Nuclear Instruments and Methods in Physics Research Section A: Accelerators, Spectrometers, Detectors and Associated Equipment **254**, 26–34 (1987).

[154]K. Daumiller, R. Engel, H. Kern, et al., *Scintillator Surface Detectors of the Engineering Array:Production and Validation*, GAP-2016-040 (Karlsruhe Institute of Technology, 2016).

[155]X. Bertou, P. Allison, C. Bonifazi, P. Bauleo, C. Grunfeld, M. Aglietta, F. Arneodo, D. Barnhill, J. Beatty, N. Busca, et al., "Calibration of the surface array of the Pierre Auger Observatory," Nuclear Instruments and Methods in Physics Research Section A: Accelerators, Spectrometers, Detectors and Associated Equipment **568**, 839–846 (2006).

[156]D. Schmidt, for the Pierre Auger Collaboration, "AugerPrime implementation in the Offline simulation and reconstruction framework," in International cosmic ray conference, Vol. 3 (2017).

[157]A. Castellina, for the Pierre Auger Collaboration, "The dynamic range of the AugerPrime Surface Detector: technical solution and physics reach," in International cosmic ray conference, Vol. 3 (2017).

[158]G. Cataldi and M.R. Coluccia1, D. Martello1, and R. Smida, *SSD Engineering Array performance*, GAP-2017-032 (2017).

[159]R. SATO, "Long Term Performance of the Surface Detectors of the Pierre Auger Observatory," in 32th international cosmic ray conference beijing, Vol. 3 (2011), p. 204.

[160]I. Antcheva, M. Ballintijn, B. Bellenot, M. Biskup, R. Brun, N. Buncic, P. Canal, D. Casadei, O. Couet, V. Fine, et al., "ROOT—A C++ framework for petabyte data storage, statistical analysis and visualization," Computer Physics Communications **182**, 1384–1385 (2011).

[161]M. Morháč, J. Kliman, V. Matoušek, et al., "Background elimination methods for multidimensional coincidence γ-ray spectra," Nuclear Instruments and Methods in Physics Research Section A: Accelerators, Spectrometers, Detectors and Associated Equipment **401**, 113–132 (1997).

[162]C. Ryan, E. Clayton, W. Griffin, S. Sie, and D. Cousens, "SNIP, a statistics-sensitive background treatment for the quantitative analysis of PIXE spectra in geoscience applications," Nuclear Instruments and Methods in Physics Research Section B: Beam Interactions with Materials and Atoms **34**, 396–402 (1988).

[163]P. Bauleo, A. Castellina, A. Chou, J. Harton, R. Knapik, G. Navarra, P. A. Collaboration, et al., "The accuracy of signal measurement with the water Cherenkov detectors of the Pierre Auger Observatory," Nuclear Instruments and Methods in Physics Research A **578**, 180–184 (2007).

[164]KASCADE collaboration, "The cosmic-ray experiment KASCADE," Nucl. Instruments Methods Phys. Res. Sect. A Accel. Spectrometers, Detect. Assoc. Equip. **513**, 490–510 (2003).

[165]J. Hinton and W. Hofmann, "Teraelectronvolt astronomy," Annual Review of Astronomy and Astrophysics **47**, 523–565 (2009).

[166]J. Holder, "TeV gamma-ray astronomy: A summary," Astroparticle Physics **39**, 61–75 (2012).

[167]S. Wakely and D. Horan, "Online catalog for TeV astronomy," (2014).

[168]Z. Cao et al., "Status of LHAASO updates from ARGO-YBJ," Nuclear Instruments and Methods in Physics Research Section A: Accelerators, Spectrometers, Detectors and Associated Equipment **742**, 95–98 (2014).

[169]M. Zha et al., "Status of the large high altitude air shower observatory project," Nuclear Instruments and Methods in Physics Research Section A: Accelerators, Spectrometers, Detectors and Associated Equipment **692**, 77–82 (2012).

[170]M. Actis, G. Agnetta, F. Aharonian, A. Akhperjanian, J. Aleksić, E. Aliu, D. Allan, I. Allekotte, F. Antico, L. Antonelli, et al., "Design concepts for the Cherenkov Telescope Array CTA: an advanced facility for ground-based high-energy gamma-ray astronomy," Experimental Astronomy **32**, 193–316 (2011).

[171]G. Di Sciascio, L. Collaboration, et al., "The LHAASO experiment: from Gamma-Ray Astronomy to Cosmic Rays," Nuclear and Particle Physics Proceedings **279**, 166–173 (2016).

[172]L. Q. Yin, et al., "Accurate Measurement of the Cosmic Ray Proton Spectrum from 100TeV to 10PeV with LHAASO," in International cosmic ray conference, Vol. 3 (2017).

[173]Y. Liu, Z. Cao, S. Chen, Y. Chen, S. Cui, H. He, X. Huang, X. Ma, Q. Yuan, X. Zhang, et al., "Expectation on Observation of Supernova Remnants with the LHAASO Project," The Astrophysical Journal **826**, 63 (2016).

[174]X. Li, C. Liu, X. Ding, W. Du, H. Wu, and H. Li, "Simulation of the dynamic range extension system for the LHAASO-WCDA experiment," **3** (2017).

[175]H. Lv, H. He, X. Sheng, and J. Liu, "Timing calibration of the lhaaso-km2a electromagnetic particle detectors," **3** (2017).

[176]J. Liu, X. SHENG, and H. HE, "Performances of the LHAASO-KM2A engineering array," in Proceedings of the 32nd internationl cosmic ray conference (2011).

[177]L. Jia, S. Xiang-Dong, H. Hui-Hai, et al., "Performances and long-term stability of the LHAASO-KM2A prototype array," Chinese physics C **38**, 026001 (2014).

[178]G. Xiao, X. ZUO, X. LI, and S. FENG, "Design and performance of prototype muon detector of LHAASO-KM2A," in Proceedings of the 33rd international cosmic ray conference (Citeseer, 2013).

[179]Mingjun Chen on behalf of LHAASO colloboration, "Status of water cherenkov detector array of lhaaso project," **3** (2017).

[180]H.-C. Li, Z.-G. Yao, C.-X. Yu, M.-J. Chen, H.-R. Wu, M. Zha, B. Gao, X.-J. Wang, J.-Y. Liu, W.-Y. Liao, et al., "A method to monitor and measure the water transparency in LHAASO-WCDA using cosmic muon signals," Chinese physics C **41**, 026002 (2017).

[181]Z. Yao, M. Zha, Z. Cao, H. He, et al., "LHAASO Simulation: Performance of the Water Cherenkov Detector Array,"

[182]M. Chen, Z. Yao, B. Gao, B. Zhou, H. Wu, and H. LI, "R&D of LHAASO-WCDA," Proc. of the 32nd ICRC (2011).

[183]Q. An, Y. Bai, X. Bi, Z. Cao, Z. Cao, J. Chang, G. Chen, L. Chen, M. Chen, T. Chen, et al., "Performance of a prototype water Cherenkov detector for LHAASO project," Nuclear Instruments and Methods in Physics Research Section A: Accelerators, Spectrometers, Detectors and Associated Equipment **644**, 11–17 (2011).

[184]Q. An, Y. Bai, X. Bi, Z. Cao, J. Chang, G. Chen, M. Chen, S. Chen, S. Chen, T. Chen, et al., "The performance of a prototype array of water Cherenkov detectors for the LHAASO project," Nuclear Instruments and Methods in Physics Research Section A: Accelerators, Spectrometers, Detectors and Associated Equipment **724**, 12–19 (2013).

[185]H. Li, Z. Yao, M. Chen, C. Yu, M. Zha, H. Wu, B. Gao, X. Wang, J. Liu, W. Liao, et al., "Study on single-channel signals of water Cherenkov detector array for the LHAASO project," Nuclear Instruments and Methods in Physics Research Section A: Accelerators, Spectrometers, Detectors and Associated Equipment **854**, 107–112 (2017).

[186]S. Zhang, "Studying Cosmic Ray Energy Spectrum above 10TeV using WFCA Prototype," PhD thesis (Ph. D. Thesis, IHEP, 2010).

[187]B. Bartoli, P. Bernardini, X. Bi, Z. Cao, S. Catalanotti, S. Chen, T. Chen, S. Cui, B. Dai, A. D'Amone, et al., "Knee of the cosmic hydrogen and helium spectrum below 1 PeV measured by ARGO-YBJ and a Cherenkov telescope of LHAASO," Physical Review D **92**, 092005 (2015).

[188]M. Giller, G. Wieczorek, A. Kacperczyk, H. Stojek, and W. Tkaczyk, "Energy spectra of electrons in the extensive air showers of ultra-high energy," Journal of Physics G: Nuclear and Particle Physics **30**, 97 (2004).

[189]T. Weekes, "Book Review: Very high energy gamma-ray astronomy/Institute of Physics, 2003," The Observatory **123**, 382 (2003).

[190]H. Cabot, C. Meynadier, D. Sobczyńska, B. Szabelska, J. Szabelski, and T. Wibig, "Measurable difference in Cherenkov light between gamma and hadron induced EAS," Astroparticle Physics **9**, 269–276 (1998).

[191]T. Ergin, "The energy spectrum of very high energy gamma rays from the Crab Nebula as measured by the HESS array," PhD thesis (Humboldt-Universität zu Berlin, Mathematisch-Naturwissenschaftliche Fakultät I, 2006).

[192]F. Arqueros and T. H. Collaboration, "Energy spectrum and chemical composition of cosmic rays between 0.3 and 10 PeV determined from the Cherenkov-light and charged-particle distributions in air showers," arXiv preprint astro-ph/9908202 (1999).

[193]J. Fowler, L. Fortson, C. Jui, D. Kieda, R. Ong, C. Pryke, and P. Sommers, "A measurement of the cosmic ray spectrum and composition at the knee," Astroparticle Physics **15**, 49–64 (2001).

[194]O. Gress, T. Gress, E. Korosteleva, L. Kuzmichev, B. Lubsandorzhiev, L. Pan'kov, Y. V. Parfenov, P. Pohil, V. Prosin, and Y. A. Semeney, "The study of primary cosmic rays energy spectrum and mass composition in the energy range 0.5–50 PeV with TUNKA EAS Cherenkov array," Nuclear Physics B-Proceedings Supplements **75**, 299–301 (1999).

[195]D. Chernov, E. Korosteleva, L. Kuzmichev, V. Prosin, I. Yashin, N. Budnev, O. Gress, T. Gress, L. Pankov, Y. V. Parfenov, et al., "Primary energy spectrum and mass composition determined with the Tunka EAS Cherenkov array," International Journal of Modern Physics A **20**, 6799–6801 (2005).

[196]C. W. Akerlof, M. Cawley, D. Fegan, A. Hillas, R. Lamb, D. Lewis, D. Meyer, and T. Weekes, "Granite, a new very high energy gamma-ray telescope," Nuclear Physics B-Proceedings Supplements **14**, 237–243 (1990).

[197]F. Aharonian, G. Heinzelmann, H. collaboration, et al., "The HEGRA experiment status and recent results," Nuclear Physics B-Proceedings Supplements **60**, 193–198 (1998).

[198]F. Aharonian, A. Akhperjanian, A. Bazer-Bachi, M. Beilicke, W. Benbow, D. Berge, K. Bernlöhr, C. Boisson, O. Bolz, V. Borrel, et al., "The HESS survey of the inner galaxy in very high energy gamma rays," The Astrophysical Journal **636**, 777 (2006).

[199]R. Enomoto, S. Hara, A. Asahara, G. Bicknell, P. G. Edwards, S. Gunji, T. Hara, J. Jimbo, F. Kajino, H. Katagiri, et al., "Design study of CANGAROO-III, stereoscopic imaging atmospheric Cherenkov telescopes for sub-TeV γ-ray detection," Astroparticle Physics **16**, 235–244 (2002).

[200]N. Park et al., "Performance of the VERITAS experiment," arXiv preprint arXiv:1508.07070 (2015).

[201]J. Albert, E. Aliu, H. Anderhub, P. Antoranz, A. Armada, M. Asensio, C. Baixeras, J. Barrio, M. Bartelt, H. Bartko, et al., "Observation of gamma rays from the galactic center with the MAGIC telescope," The Astrophysical Journal Letters **638**, L101 (2006).

[202]M. Doro, C. Consortium, et al., "CTA—a project for a new generation of Cherenkov telescopes," Nuclear Instruments and Methods in Physics Research Section A: Accelerators, Spectrometers, Detectors and Associated Equipment **630**, 285–290 (2011).

[203]The CTA collaboration, https://www.cta-observatory.org/project/technology/.

[204]A. M. Hillas, "Cerenkov light images of EAS produced by primary gamma," in International cosmic ray conference, Vol. 3 (1985).

[205]D. Heck, G. Schatz, J. Knapp, T. Thouw, and J. Capdevielle, *CORSIKA: A Monte Carlo code to simulate extensive air showers*, tech. rep. (1998).

[206]S. W. Cui, et al., "Simulation on gamma-ray astronomy research with LHAASO-KM2A," Astropart. Phys. **54**, 86–92 (2014).

[207]S. S. Zhang, et al., "Properties and performance of two wide field of view Cherenkov/fluorescence telescope array prototypes," Nucl. Instrum. Meth. A **629**, 57–65 (2011).

[208]J. G. Gonzalez, "Measuring the muon content of air showers with IceTop," in Epj web of conferences, Vol. 99 (EDP Sciences, 2015), p. 06002.

[209]A. Hoecker, P. Speckmayer, J. Stelzer, J. Therhaag, E. von Toerne, H. Voss, M. Backes, T. Carli, O. Cohen, A. Christov, et al., "TMVA-Toolkit for multivariate data analysis," arXiv preprint physics/0703039 (2007).

[210]J. R. Hoerandel, "On the knee in the energy spectrum of cosmic rays," Astroparticle Physics **19**, 193–220 (2003).

List of Tables

List of Figures

Résumé de thèse :
« Étude des rayons cosmiques par Auger et LHAASO : R&D et analyse de données d'AugerPrime et simulations pour LHAASO »

Doctorant : Zizhao Zong

Directrice de thèse : Prof. Tiina Suomijärvi

Affiliation: Institut de Physique Nucléaire d'Orsay (IPN) – CNRS-IN2P3

Université Paris-Sud / Université Paris-Saclay

Après la découverte des rayons cosmiques en 1912, un grand nombre d'études ont été réalisées pour comprendre leur nature et leur origine. Pour les études expérimentales, des ballons, des satellites et des détecteurs au sol ont été utilisés. Le spectre des rayons cosmiques observé s'étend de quelques GeV jusqu'à $\sim 10^{20}$eV. En mesurant avec précision la composition de masse, le spectre d'énergie et la direction d'arrivée des rayons cosmiques de haute énergie, y compris les particules chargées, les rayons gamma et les neutrinos, nous nous attendons à mieux comprendre leur origine.

L'observatoire Pierre Auger (Malargüe, Argentine), visant à sonder l'origine des rayons cosmiques avec les énergies extrêmes ($>10^{18}$eV), a pris régulièrement des données depuis 2004 et a obtenu de résultats importants. En particulier, une suppression de flux est clairement observée à $E> 4 \times 10^{19}$ eV, et la composition des rayons cosmiques a tendance à alourdir aux énergies élevées, au delà de quelques 10^{18}eV. La collaboration Auger a proposé un projet d'amélioration de l'Observatoire, baptisé «AugerPrime», afin de déterminer avec précision la composition en masse des rayons cosmiques à

ultra-haute énergie (UHECR). Pour cela, un détecteur scintillateur sera installé sur les déteteur Cherenkov à eau du réseau de surface. Le réseau d'ingénierie (EA) de 12 stations de détecteur d'AugerPrime a été déployé en octobre 2016 et, depuis lors, prend continuellement des données.

Le grand observatoire de rayons gammas et rayons cosmiques à haute altitude (LHAASO), actuellement en construction à 4400 a.s.l. à Daocheng, en Chine, est une expérience d'astro-particules à usages multiples. L'un des objectifs scientifiques de LHAASO est de mesurer le spectre des rayons cosmiques autour de la région «genou» de 30 TeV à 100 PeV. LHAASO propose de détecter les gerbes atmosphériques induites par différentes particules primaires avec une technique hybride en combinant trois réseaux de détecteurs, un réseau de télescopes Cherenkov (WFCTA), un réseau de détecteurs Cherenkov à eau (WCDA) et un réseau de 1 km^2 (KM2A). Cette observation hybride devrait avoir de bonnes performances pour mésurer l'énergie, la direction d'arrivée, et la masse des particules primaires.

Ce travail de thèse a été mené dans le cadre de ces deux expériences et porte principalement sur les travaux de R&D des détecteurs scintillateurs d'AugerPrime, sur l'analyse des premières données d'AugerPrime EA, sur la simulation de WFCTA, et sur l'analyse des données de simulation hybride de LHAASO en utilisant la méthode d'analyse multivariée (MVA).

Le manuscrit de cette thèse est organisé comme suit:

Le chapitre 1 donne une brève introduction à l'ensemble du travail de thèse.

Dans le chapitre 2, les études sur les rayons cosmiques sont brièvement introduites, y compris les principes de physique des rayons cosmiques, les

gerbes atmosphériques (extensive air shower, EAS) et les expériences au sol sur les rayons cosmiques.

Au chapitre 3, l'observatoire Pierre Auger et les principaux résultats sont présentés. La motivation physique et les implémentations techniques du projet d'amélioration AugerPrime sont également présentées.

Au chapitre 4, les travaux de R&D des détecteurs de scintillateurs (SSD) d'AugerPrime sont présentés. Ces traveaux portent sur les tests des configurations SSD et la fabrication du module de couplage optique fibre / PMT.

Les résultats liés au test des composants SSD (scintillateur, fibre optique et couplage optique) et l'estimation de l'efficacité de collecte de lumière (LCE) pour différentes configurations scintillateur / fibre sont rapportés. Tous ces résultats ont été discutés lors des réunions de collaboration pendant la phase R&D du SSD. La configuration (scintillateur à 2 trous de 50 × 10 mm^2 du FNAL + Kuraray Y11 (300) -MSJ (diamètre 1,0 mm) fibre WLS + «cookies » de RTV silicone) a été choisie pour AugerPrime en fonction de la performance, de la fiabilité et du coût total. Le signal de sortie de cette configuration de détecteur est > 30 ph.e. (HV = 1100V), qui satisfait aux exigences de performances du détecteur SSD (> 12 ph.e.).

Un détecteur scintillateur a été assemblé et équipé du module de couplage optique avec la méthode de polissage développée dans ce travail. De bons résultats pour les amplitudes de signal, le rapport pic-sur-vallée et d'uniformité du détecteur sont obtenus à partir du test de ce détecteur en utilisant la tour à muons de KIT (Karlsruher Institut für Technologie, Allemagne). Actuellement, ce détecteur est déployé dans l'une des stations d'EA (i.d. 25).

Au chapitre 5, l'analyse des premières données du réseau d'ingénierie AugerPrime constitué de 12 stations de détecteur améliorées est presentée. En

particulier, l'étalonnage du détecteur et la performance des stations d'EA sont présentés. En outre, les signaux de gerbe mesurés à la fois par les détecteurs Cherenkov à eau (WCD) et les détecteurs de scintillateur anisi que les résultats préliminaires sur la précision du signal sont discutés. Ce travail a été réalisé en collaboration avec l'équipe AugerPrime. L'auteur a développé la routine pour lire les premières données du réseau d'ingénierie d'AugerPrime.

Les résultats de l'analyse des données d'EA montrent une bonne stabilité et une bonne performance pour l'opération EA. Les niveaux de bruit observés sont légèrement supérieurs aux spécifications. Cela a été corrigé dans les prochains prototypes actuellement en cours de fabrication. Les signaux de gerbes mésurées par des stations d'EA sont en bon accord avec la fonction de distribution latérale (LDF) définie par le réseau de détecteurs de surface (SD) existant. La LDF globale du S_{WCD} normalisée par la taille de la gerbe concorde bien avec celle des stations existantes. La LDF globale de S_{SSD} indique la sensibilité du SSD au composante électromagnétique (EM) de l'EAS, comme prévu. L'étude de la précision du signal WCD donne un résultat préliminaire d'environ 10% pour les stations d'EA, ce qui est comparable à celui du réseau SD existante. D'autres études sur la performance avec de meilleures statistiques sont actuellement en cours.

Au chapitre 6, les objectifs scientifiques de LHAASO et la conception des réseaux de détecteurs WCDA, KM2A et WFCTA sont introduits.

Au chapitre 7, la simulation de LHAASO-WFCTA est d'abord présentée. La reconstruction de l'énergie primaire de l'EAS basée sur la simulation WFCTA est ensuite introduite. Dans les dernières sections de ce chapitre, les résultats obtenus sur l'identification des particules primaires avec le détecteur hybride LHAASO, qui consiste en WCDA, KM2A et WFCTA en utilisant la méthode multivariée, sont présentés.

Dans ce travail, le code de simulation WFCTA a été développé par l'équipe LHAASO-WFCTA. En tant que membre de cette équipe, l'auteur a optimisé

le module d'I/O et la structure du code, développé le module de simulation de caméra et participé à l'optimisation du code. Sur la base des données de simulation, il est prévu que WFCTA mesurera l'énergie primaire des gerbes atmosphériques avec une précision de ~ 20% sur la gamme d'énergie de 100 TeV à 10 PeV.

Concernant l'identification des particules avec les méthodes MVA, la simulation des gerbes atmosphériques et des détecteurs LHAASO a été mise en œuvre par les collaborateurs de l'IHEP (Institute of High Energy Physics, China). Les caractéristiques des différents algorithmes MVA et la comparaison de leurs performances lorsqu'elles sont utilisées pour l'identification de masse primaire sont discutées. L'auteur a fait la préparation (ajustement et réglage) des données de simulation, développé les scripts MVA pour la classification de masse primaire et analysé les résultats des classificateurs MVA. De très bons résultats sont obtenus pour les séparations Iron / proton et nucléide lourd / p + He. D'autres études devraient être effectuées avec de meilleures statistiques pour la composition de masse et pour une plus grande gamme d'énergie des rayons cosmiques.

Au chapitre 8, tous les résultats de cette thèse sont résumés et les perspectives de travaux futurs sont discutées.

Actuellement, les projets AugerPrime et LHAASO sont en cours de construction. Les études présentées dans cette thèse ont été présentées et discutées lors des réunions de collaboration et des conférences et ont contribué de façon significative aux deux projets.

université PARIS-SACLAY | ÉCOLE DOCTORALE PHENIICS

Titre : Étude des rayons cosmiques par Auger et LHAASO : R&D et analyse de données d'AugerPrime et simulations pour LHAASO

Mots clés : Rayons cosmiques, Gerbes atmosphéric (EAS), EAS instrumentation

Résumé : Les rayons cosmiques sont des particules chargées, ainsi que des coproduits comme les photons et les neutrinos, issus de sources de rayons cosmiques galactiques ou extragalactiques. Ils arrivent au sommet de l'atmosphère terrestre avec des énergies primaires allant jusqu'à quelques 10 EeV. Lorsque les rayons cosmiques entrent dans l'atmosphère, ils interagissent avec les molécules de l'air et produisent un grand nombre de particules secondaires, créant une gerbe atmosphérique (extensive air shower, EAS). Accompagné des particules secondaires, une émission de la lumière Cherenkov et de la lumière fluorescence est induite par le passage des particules dans l'atmosphère. L'Observatoire Pierre Auger et Large High Altitude Air Shower Observatory (LHAASO) sont des observatoires dédiés à la détection des gerbes atmosphériques dans le but de répondre aux questions ouvertes concernant les rayons cosmiques, mais se concentrant sur différentes gammes d'énergie, les plus hautes énergies et les énergies autour de quelques PeV. Après plus de 10 ans d'exploitation de l'Observatoire Pierre Auger, la collaboration Auger a proposé une amélioration des détecteurs de son réseau de surface, appelée «AugerPrime». Le but est d'augmenter la sensibilité à la masse des particules primaires en ajoutant un détecteur scintillateur sur le détecteur Cherenkov à eau. Les deux observatoires sont dits «hybrides» car composés de télescopes optiques observant le développement longitudinal des gerbes et des réseaux de détecteurs de surface échantillonnant leurs profils latéreaux. Dans cette thèse, une série d'études contribuant aux projets AugerPrime et LHAASO sont présentées. En ce qui concerne le projet AugerPrime, la présente étude comprend le travail de recherche & dévelopment des scintillateurs et l'analyse de données du réseau de tester. Pour le projet LHAASO, des simulations de télescopes Cherenkov et une analyse multivariée des observations hybrides pour l'identification des masses primaires sont présentées.

Title: Study of cosmic rays by Auger and LHAASO: R&D and Data Analysis of AugerPrime and simulations for LHAASO

Keywords: Cosmic rays, Extensive Air Shower (EAS), EAS instrumentation

Abstract: Cosmic rays are charged particles, as well as coproducts like photons and neutrinos, originated in cosmic-ray sources inside or outside the Galaxy. They arrive at the top of the Earth's atmosphere with primary energies of up to a few 10 EeV. When the cosmic rays enter the atmosphere, they interact with the molecules in the air and produce a large number of secondary particles, creating an extensive air shower (EAS). The ground-based observation of the EAS can be used to deduce the energy, the arrival direction, and the mass composition of cosmic rays. The Pierre Auger Observatory and the Large High Altitude Air Shower Observatory (LHAASO) are both EAS observatories aiming at solving open questions of cosmic-ray studies but focusing on different energy ranges, the highest-energy and the so-called knee (around few PeV) regions. Based on the experience gained during the operation of the Pierre Auger Observatory for more than 10 years, the Auger collaboration has proposed an upgrade project, called "AugerPrime", with the aim of increasing the sensitivity of the surface detector array to the primary mass of cosmic rays. Both observatories employ the so-called "hybrid detector arrays" composed of optical telescopes overlooking the longitudinal development and ground detector arrays sampling the signal densities in the lateral direction of the EAS. The ground detector arrays of both observatories are being constructed or upgraded to have various types of particle detectors (scintillator and water-Cherenkov detectors), which allow us to decompose the electromagnetic and muonic components of the EAS. In this thesis, a series of studies contributing to the AugerPrime and LHAASO projects are presented. Concerning the AugerPrime project, the present study includes R&D work of the scintillator detector and data analysis of the engineering array. For the LHAASO project, simulations of the wide field of view Cherenkov telescope array and a multivariate analysis of LHAASO-hybrid observations for the primary mass identification are presented.

Université Paris-Saclay
Espace Technologique / Immeuble Discovery
Route de l'Orme aux Merisiers RD 128 / 91190 Saint-Aubin, France